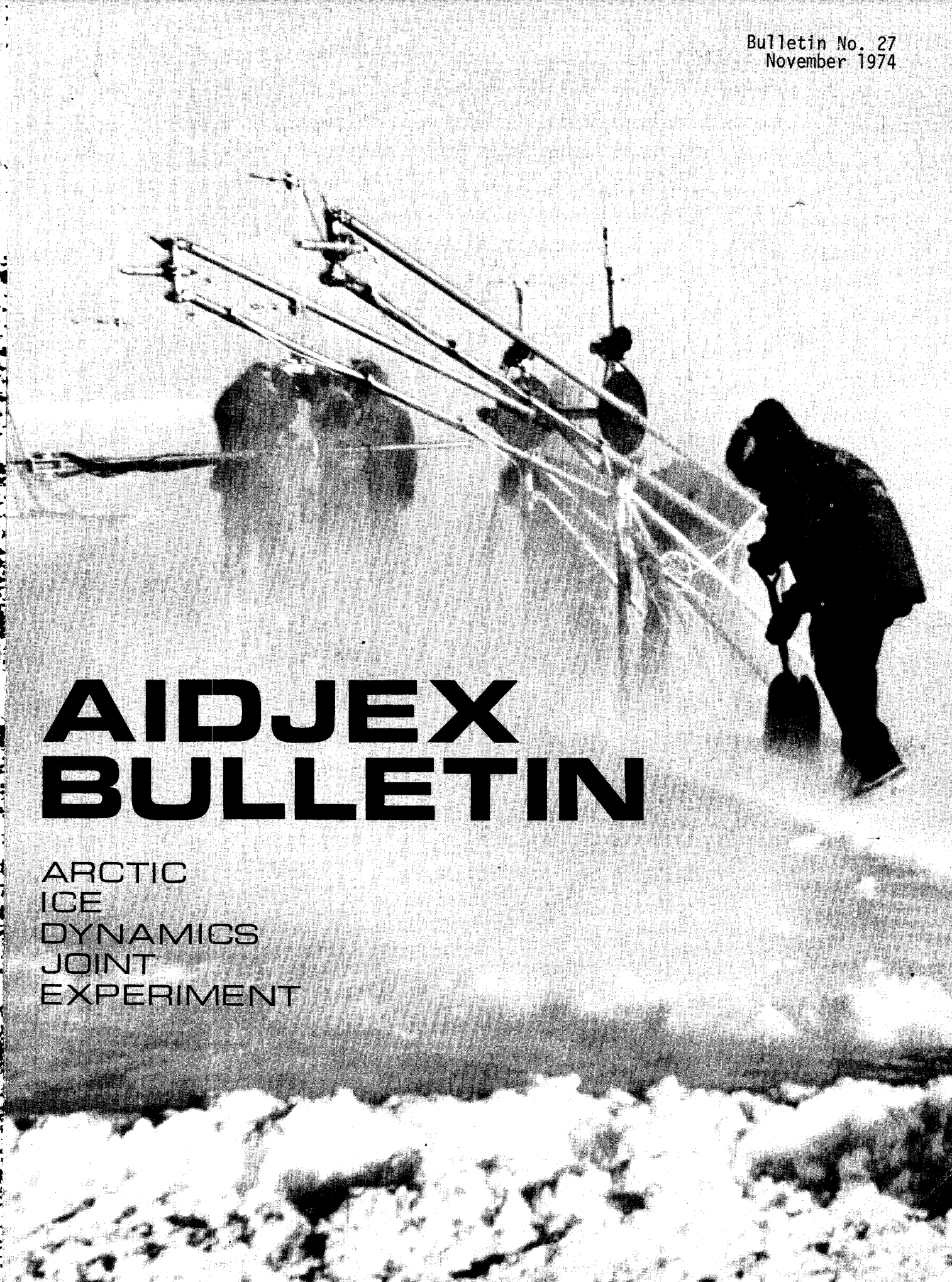


Bulletin No. 27
November 1974



AIDJEX BULLETIN

ARCTIC
ICE
DYNAMICS
JOINT
EXPERIMENT

AIDJEX BULLETIN No. 27

November 1974

Contents

THE USE OF SATELLITE PHOTOGRAPHS TO GIVE THE MOVEMENT AND DEFORMATION OF SEA ICE --J.F. Nye and D.R. Thomas	1
THE REMOTE SENSING PROGRAM REQUIRED FOR THE AIDJEX MODEL --W.F. Weeks, Max D. Coon, and W.J. Campbell	22
ELASTIC STRAIN IN THE AIDJEX SEA ICE MODEL --R.S. Pritchard	45
THE ENERGETICS OF PLASTIC DEFORMATION IN PACK ICE --D.A. Rothrock	63
COMPARISON OF SHEAR STRESS CALCULATIONS BETWEEN TWO PROFILE METHODS USING SOME DRAG-PLATE MEASUREMENTS --Chi-Hai Ling	84
HYDROSTATIC LEVELING ON FLOATING ICE --J.R. Weber	91
ICE ISLAND REPORT --P. Martin and A. Thorndike	108
REPORTS FROM THE PRINCIPAL INVESTIGATORS, AIDJEX LEAD EXPERIMENT	117
EFFECT OF OPEN LEADS ON THE EXCHANGE OF CO ₂ BETWEEN THE ATMOSPHERE AND SURFACE SEA WATER --J.J. Kelley	121
OCEANOGRAPHIC INVESTIGATIONS DURING THE AIDJEX LEAD EXPERIMENT --J. Dungan Smith	125
TURBIDITY IN THE ARCTIC ATMOSPHERE --B. Holmgren, G. Shaw, and G. Weller	135
LOCAL RADIATION FLUXES OVER OPEN AND FREEZING LEADS IN THE POLAR PACK ICE --B. Holmgren and G. Weller	149
SODAR INVESTIGATIONS OF THE EFFECT OF OPEN LEADS ON THE BOUNDARY LAYER STRUCTURE OVER THE ARCTIC BASIN --B. Holmgren and L. Spears	167

*Front cover: Atmospheric instrumentation at the artificial lead
experiment on Elson Lagoon in March 1974.*

*Back cover: Sir Thorndike Peabody, noted arctic yachtsman, maintaining
a grip on his sloop "Snowflake," which was taking some water.*

AIDJEX BULLETIN No. 27

November 1974

* * * * *

*Financial support for AIDJEX is provided by
the National Science Foundation,
the Office of Naval Research,
and other U.S. and Canadian agencies.*

* * * * *

Arctic Ice Dynamics Joint Experiment
Division of Marine Resources
University of Washington
Seattle, Washington 98105

Division of Marine Resources
UNIVERSITY OF WASHINGTON

The AIDJEX Bulletin aims to provide both a forum for discussing AIDJEX problems and a source of information pertinent to all AIDJEX participants. Issues--numbered, dated, and sometimes subtitled--contain technical material closely related to AIDJEX, informal reports on theoretical and field work, translations of relevant scientific reports, and discussions of interim AIDJEX results.

The first part of Bulletin No. 27 covers several subjects, among them the AIDJEX model and the goals for remote sensing during the main experiment. The second half of the Bulletin (starting on page 117) is devoted to the AIDJEX lead experiment of last spring.

We are indebted to The Australian Student, vol. 9(3), April 1973, for the following succinct description of AIDJEX, passed on to us this summer by Gunter Weller:

American scientists are descending into a hole cut in an ice floe about 270 miles north-west of Cape Barrow, at the northern tip of Alaska. The ice floe, three-quarters of a mile long, half a mile wide and nine feet deep, is being studied as part of an intensive research into Arctic Ocean icebergs and their effect on world climatic conditions. The project, called the Arctic Ice Dynamics Joint Experiment (AIDJEX), will be conducted in stages until 1976.

We share Dr. Weller's apprehension, expressed in an attached note: "Just hope that not all of the American scientists are descending into that dreadful hole."

Any correspondence concerning the Bulletin should be addressed to

*Alma Johnson, Editor
AIDJEX Bulletin
4059 Roosevelt Way N.E.
Seattle, Washington 98105*

THE USE OF SATELLITE PHOTOGRAPHS TO GIVE THE MOVEMENT AND DEFORMATION OF SEA ICE

by

J. F. Nye
Physics Department
University of Bristol, England

and

D. R. Thomas
AIDJEX

ABSTRACT

A preliminary study of ERTS-A 1973 photography of the AIDJEX area has been made to test the hypothesis that the pack ice can be modeled as a continuum and to examine the spatial scales involved. In all three cases examined there was a spatial variation of ice velocity on a scale of some 500 km, with smaller-scale variations of smaller amplitude superimposed. The large-scale velocity varied from about 8 km day^{-1} to zero, while the small-scale variations were about 0.3 km day^{-1} . The strain rate calculated from the large-scale velocity varied from $2.5\% \text{ day}^{-1}$ to zero. From the photographs one can assess what effect the gauge length has on measured strain rates. Our preliminary results suggest that a gauge length of 50 km may give a strain rate differing from the regional average by about $1\% \text{ day}^{-1}$; for a gauge length of 100 km the corresponding figure was $0.4\% \text{ day}^{-1}$ for all three cases examined.

Our measurements support the adoption of a continuum model for the pack ice and suggest that measurements adequate for the purposes of the AIDJEX model will be readily obtainable during spring 1975 from ERTS-B pictures, provided of course that the satellite is operating. Comparison with the model during the Main Experiment may be done with strain rate and with velocity. The strain rate may be obtained by superimposing successive ERTS pictures of the same ice features. The displacement of ice features over an interval of a few days may also be measured satisfactorily, particularly when the information from ERTS is combined with that from the manned camps and the data buoys. This can be done without these stations being visible on the photographs.

If ERTS-B is not operating it is suggested that information on displacement to check the model could be obtained from aircraft

photographs, using the navigation system of the aircraft to determine the geographical position of the ice features. Alternatively, a new method of stereophotogrammetry without use of ground control is suggested.

1. INTRODUCTION

Movement and deformation studies of sea ice using the photographs taken by the first Earth Resources Technology Satellite (ERTS-A) have already been made by Crowder et al. [1974], Hibler et al. [in press], Shapiro and Burns [in press], and Barnes and Bowley [1974]. This report describes some exploratory work on a set of 1973 ERTS photographs directed specifically to the needs of the AIDJEX modeling group. We wanted to find out how much information about ice movement and deformation useful to the modeling group this set of photographs contains, and to find the best way of extracting it. If the second satellite, ERTS-B, were to be launched before the Main Experiment in 1975, or if ERTS-A were still operating, we should then know in advance how useful it was likely to be in checking the predictions of the AIDJEX model about the movement and deformation of the sea ice. But, whether or not ERTS-B is launched in time, we wanted to use the ERTS-A photographs to test the working hypothesis of the AIDJEX modeling group that on some scale or scales the ice could be modeled as a continuum (see Rothrock [in press] and Nye [1974] for statements of this hypothesis).

The general conclusion from our limited study is that the continuum hypothesis is a sound one. The next question is one of scale. The strain rate deduced from the changing distance between two points fixed in the ice will depend on the exact location of the points and on their distance apart [Nye, 1973]. If the gauge length is small, the result will depend strongly on its exact position; we must choose the gauge length long enough to reduce this source of scatter, but at the same time not make it so long that we average out significant detail in the spatial variation of the strain. Hibler et al. [1973] have concluded from point-to-point distance measurements, made with a laser-beam instrument, that the scatter due to inhomogeneities in the ice will decrease as $l^{-1/2}$, where l is the gauge length. In section 4 we present some preliminary results from the ERTS pictures on this matter of

selecting the best gauge length; the ERTS pictures are ideally suited to studying the question, for they contain all the spatial detail that is needed.

2. THE PHOTOGRAPHS AND THEIR ACCURACY

About 750 ERTS-A pictures had been obtained by the AIDJEX Data Bank from the EROS Data Center covering the period from 6 March to 28 September 1973 and the area between latitude 69°N and 81°N and between longitude 125°W and 176°W (which includes the region of the Main Experiment). The order specified that the pictures should contain no more than 30% cloud cover. The ERTS Data User's Handbook [1972] describes the ERTS system and what it produces; a useful short summary is given by Swithinbank [1973]. The pictures we used were "bulk imagery, MSS Band 5." The image is obtained by a scanning device that uses an oscillating mirror and is thus essentially a single continuous strip. This is later cut into frames. Before photographic printing the data are corrected to remove many sources of distortion, such as the tilt of the satellite and the movement of the scanning platform. As a result, each photograph is a map on a scale of 1:1,000,000 with very little distortion.

The accuracy of this map can be specified in various ways. By superimposing an ERTS positive transparency upon a 1:1,000,000 map of the Puget Sound area (northwest U.S.A.) in the position of best fit, John Sherman (personal communication) finds an error in position of only 70 m (0.07 mm on the photograph), which is about the resolving power of the system. Table F.1-6 of the ERTS Data User's Handbook estimates a "registration accuracy," which is not quite the same thing, of 159 m. However, both are quite different from the positional mapping accuracy, which is a measure of the accuracy of the latitude and longitude of a point. The latitude and longitude of the format center are printed at the edge of the photograph. The Handbook (Table F.1-6) estimates positional mapping accuracy as 757 m for paper prints; an inaccuracy of 1 km is often found in practice (Nugent, personal communication), and in one case an error of 8 km was found. We find that, if we register two successive frames by the detail they have in common

(the operation of the scanner means that this is actually the same data, but presumably corrected slightly differently for each frame), the latitude and longitude ticks on the edges of the two photographs disagree typically by 2 km. (The exact interpretation of the latitude and longitude ticks, whether to use the inner or the outer end, is in doubt. There is also doubt as to how to draw the latitude lines, which are noticeably curved in these high latitudes.) Cartographers overcome these difficulties by using ground control. We cannot do this, unless by chance a strip of usable photographs crosses a coastline. Even then there would be a cumulative error corresponding to a rotation of the whole strip about the intersection of the strip with the coastline.

The implication of all this for our problem is that we can expect to be able to measure the displacement of ice features to within about 1 or 2 km. On the other hand, we could expect to measure a *relative* displacement between two ice features on the same photograph of 100 to 200 m. Then a strain of 1% would be just detectable with a gauge length of 10 km. With a gauge length of 100 km we could expect to measure strain with an error of 0.1% strain.

These accuracies depend upon being able to identify the same clear-cut feature at different times. This is possible in practice over a period of a few days. Over a longer period, say, 18 days, a feature may remain identifiable but may change in detail. Thus, if one sets out to measure strain rate, the effect of lengthening the period of observation is that at first one gains in precision, because the strain to be measured increases, but later one may lose precision because the features become less distinct.

3. MEASUREMENTS OF DISPLACEMENT AND STRAIN

The AIDJEX Data Bank has listed its holdings of ERTS photographs, identifying each picture by latitude and longitude of the format center and by time [Stateman, 1974]. A casual search with the help of this listing yielded two pictures, dated 7 May and 24 May 1973, which are reproduced here as Figures 1a and 1b. The same ice features, such as the floe marked P, can be seen in both. The correspondence is much more readily seen when two

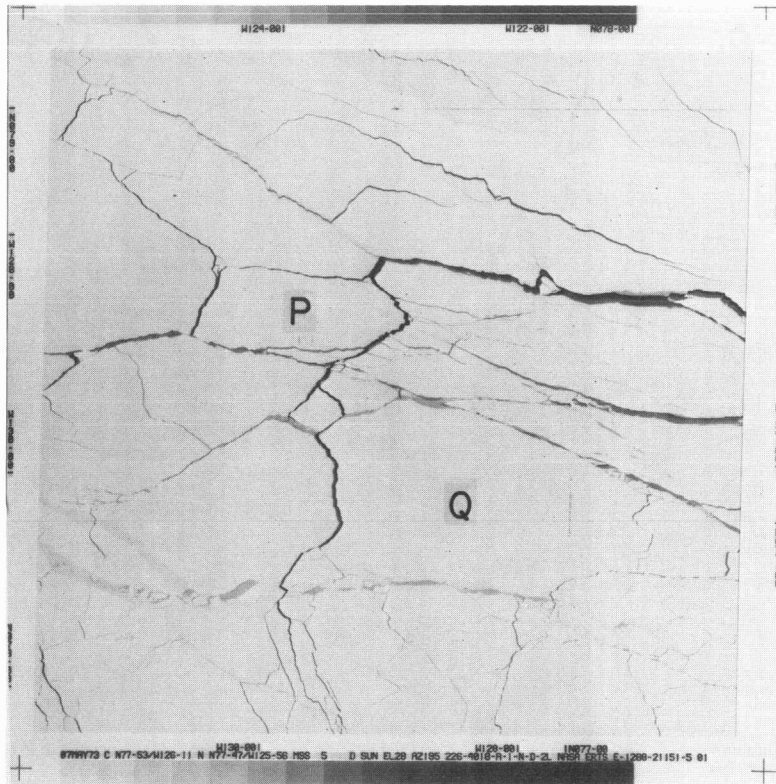


Fig. 1a. Arctic sea ice (78°N , 126°W) on 7 May 1973. ERTS photo no. E-1288-21151-5.

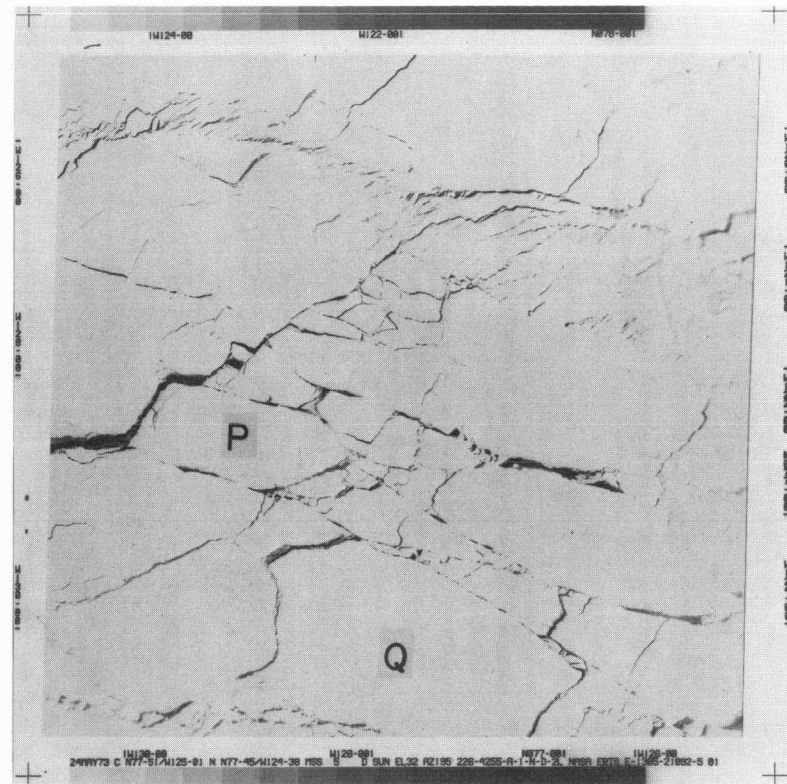


Fig. 1b. Approximately the same area as Fig. 1a, on 24 May 1973. ERTS photo no. E-1305-21092-5.

positive transparencies are superimposed. Transparencies were therefore made from the paper originals using the AIDJEX office photocopier. Although this machine is not designed to reproduce halftones well and the process gives a size change of some 0.7%, it enabled us to have usable transparencies at once. It would, of course, have been better to work on proper halftone transparencies had they been available. All the work reported here was done with transparencies produced from the office photocopier.

By drawing latitude and longitude lines on each picture and superimposing them, displacements could be readily measured. They are typically about 20 mm on the pictures, which corresponds to 20 km, in a southwesterly direction. The corresponding mean velocity is 1 km day^{-1} . The floe *P* has rotated clockwise through 4° ($0.2^\circ \text{ day}^{-1}$), its long axis has extended by 4% ($0.2\% \text{ day}^{-1}$), and its short axis has remained about the same length ($\pm 2\%$, or $\pm 0.1\% \text{ day}^{-1}$). The large floe *Q*, which is 80 km long, has rotated clockwise through the same angle and there are visible changes at its edges, but it shows no measurable overall distortion ($\pm 2\%$, or $\pm 0.1\% \text{ day}^{-1}$).

Figure 2 shows the relative motion of eight points in the ice that are visible in the two pictures. They are joined (in arbitrary pairs) by straight lines. The eight points for 7 May (joined by solid lines) are superimposed on the corresponding eight points for 24 May (joined by broken lines) by making points *O* on floes *P* coincide (this requires a displacement of 15 km) and then rotating the points for 24 May rigidly about *O* by 2.5° counterclockwise. The lack of register that remains, as seen in Figure 2, is a measure of the strain. One can see that there has been an extension north-south of some 6% in 17 days ($0.4\% \text{ day}^{-1}$). East-west there has been a compression ranging from 8% ($0.5\% \text{ day}^{-1}$) at the south end of the figure to zero at the north end.

The fact that a floe as large as *Q* was behaving rigidly, within our limits of accuracy, suggested that we should study the variation of displacements over larger distances than 100 km. For this purpose five successive ERTS frames for 21 March 1973 were joined together so that the overlapping ice detail was in register. The strip so formed was superimposed on a corresponding strip for 23 March 1973. We tried to make the latitude and longitude lines coincide for both strips; it was possible to do this to within about 2 km along the whole length. An *x* axis, 500 km long, was

drawn down the center of the overlap region and the displacements over two days of ice points originally on the x axis could then be measured.

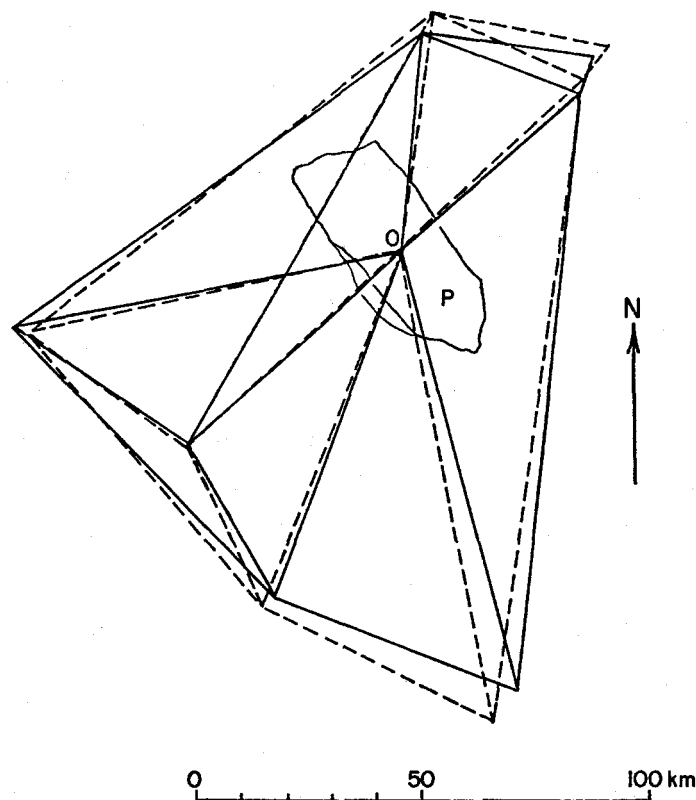


Fig. 2. Drawn from Figures 1a and 1b to show the distortion of the ice over a 17-day period.

In Figure 3a the x -component of displacement, u , is plotted against x . The most noticeable feature of these two strips was a series of zigzagging leads, each a few kilometers wide, spaced at distances of from 10 to 60 km; the edges of these leads provided nearly all the measurement points. In some cases measurable movement, widening (W) or narrowing (N), took place on them; the $u:x$ graph is nearly vertical at these places. On other segments of the measurement line strain occurred without any active leads or ridges being visible. Figure 3a shows a general trend (broken line) of u increasing with x , that is, stretching; u changes from -9.6 km (-4.8 km day $^{-1}$) to zero over a distance of 500 km, while the stretching rate increases from 0.0% day $^{-1}$ at the left (SW) to 1.9% day $^{-1}$ at the right (NE). Superimposed on this

general trend there are spatial fluctuations of u which give rise to a mean absolute deviation from the broken line of 0.43 km (0.22 km day⁻¹). This is a measure of the difference between the actual displacement (or velocity) of a point and the smoothed displacement (or velocity) curve represented by the broken line. Thus, on the left, the small-scale variations in velocity are 4.5% of the total velocity.

We then moved the x axis parallel to itself by 45 km to the southeast and, as expected, we found a second $u:x$ graph (Fig. 3b) which was similar in general features to the first one. The displacements in Figure 3b are consistently larger than in Figure 3a, and the smoothed strain rate at the right-hand end is 2.7% day⁻¹. The mean absolute deviation in Figure 3b of the observed displacements from the smoothed curve is 0.84 km (0.42 km day⁻¹). Thus, at the left-hand end of the curve the small-scale variations in velocity are 6.8% of the total velocity.

The apparent size of the floes is considerably larger from March to May than in July and August. Because a smaller floe size would presumably be more favorable to a continuum model, we tried to find usable pairs of photographs taken in the summer. None was found for August or July, because of clouds. June gave two corresponding strips (14 and 16 June 1973), and the resulting displacement measurements are shown in Figure 3c. The general trend is here adequately represented by a straight line (the broken line). As a measure of the spatial scale of this general trend we note that if the trend continued the displacement would fall to zero after 900 km. The mean absolute deviation of the measured points from this line is 0.57 km (0.29 km day⁻¹). Thus the small-scale variations in velocity are about 4% of the total.

The discussion in section 2 suggests that the *relative* displacements between neighboring points in Figures 3a, 3b, and 3c could be made accurate to within about 0.1 or 0.2 km. The present measurements are not quite as good as this, but we are sure that the deviations of our measured points from smooth curves reflect real inhomogeneities in the strain of the ice:

they are not simply errors of measurement. However, the uncertainties in latitude and longitude introduce a *systematic* error of some 2 km in the displacements.

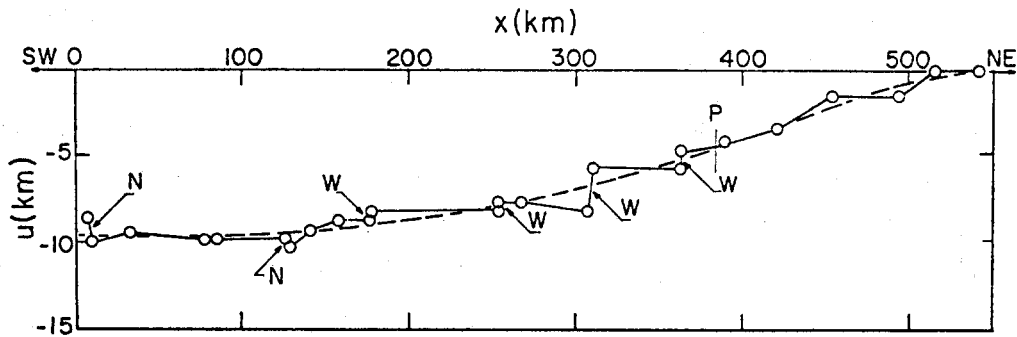


Fig. 3a. The variation of u , the x -component of displacement, with distance x along a line. Period 21-23 March 1973. From ERTS photos no. E-1241-21571-5

64-5
62-5
55-5
53-5
E-1243-22084-5
81-5
75-5
72-5
70-5

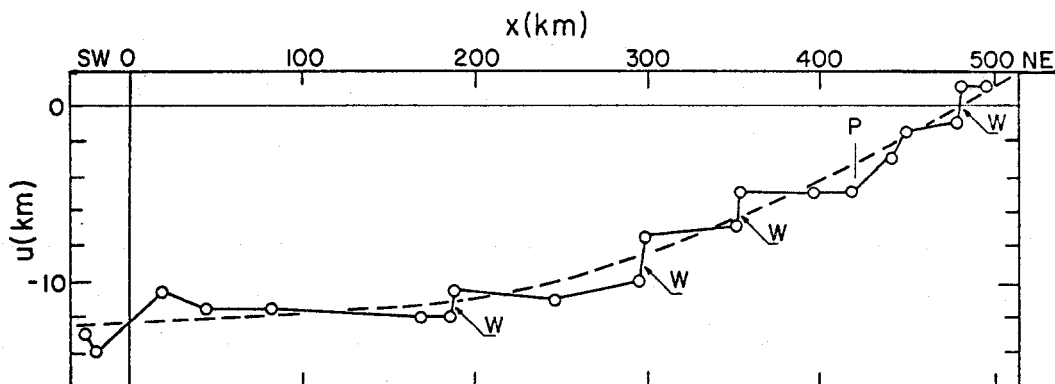


Fig. 3b. The same as Fig. 3a, but the x -axis has been moved 45 km to the southeast.

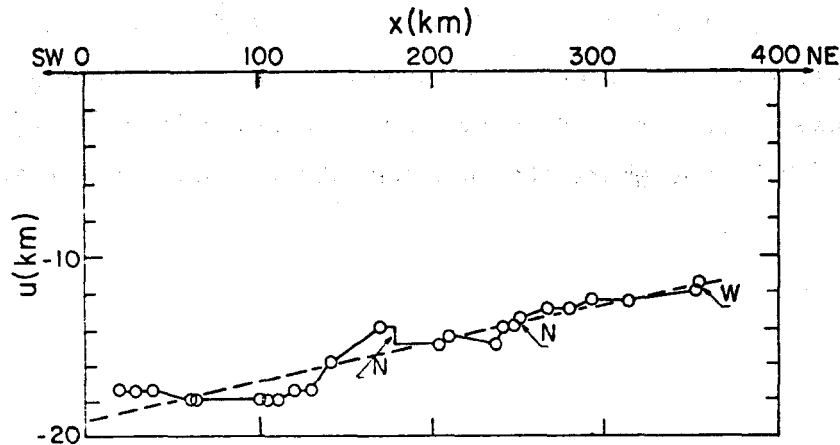


Fig. 3c. As for Fig. 3a, but for a different area later in the year (14-16 June 1973). From ERTS photos no. E-1326-21273-5

70-5

64-5

E-1328-21383-5

81-5

74-5

4. THE EFFECT OF GAUGE LENGTH

We used Figures 3a, 3b, and 3c to answer the question: if strain rate averaged over two days were measured between two specific points separated by a distance l , how close would the result be to the smoothed strain rate represented by the broken curve? This is related to the interpretation of point-to-point strain measurements on the ice surface such as those of Hibler et al. [1973] and to the questions about the definition of strain rate raised by Nye [1973].

We chose the point P in Figure 3a, where the smoothed strain rate is $1.7\% \text{ day}^{-1}$, and we selected a certain value of l ; then, by laying down the gauge length in n different positions in the neighborhood of P we made n different measurements of the strain rate $\dot{\epsilon}$ (n was about 10). The individual measurements naturally are scattered around a value close to the smoothed value; they are all plotted in Figure 4a at the selected value of l . Then l was changed and the procedure was repeated. Figure 4a shows that the scatter of the individual measurements decreases as l increases, as expected; thus a gauge length of 10 km gives a strain rate of $1.6 \pm 1.2\% \text{ day}^{-1}$, while

a gauge length of 50 km gives $1.6 \pm 0.4\% \text{ day}^{-1}$. Further increase of the gauge length does not in this case reduce the scatter appreciably. In general, it would be expected to do so until the gauge lengths began to sample parts of the curve where the smoothed strain rate was appreciably different.

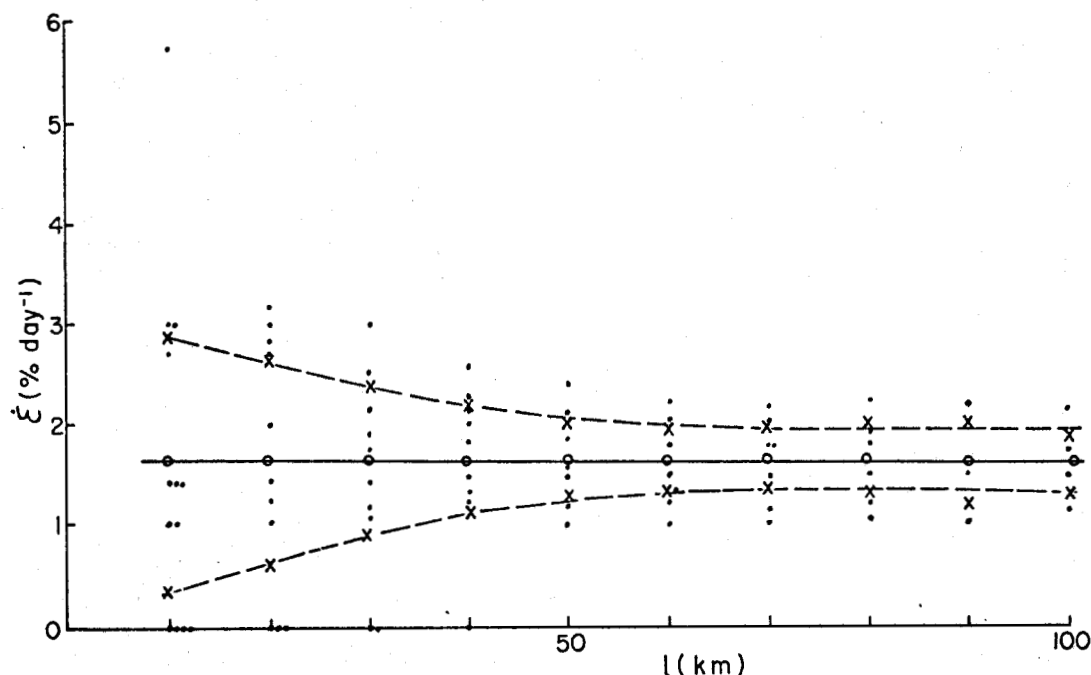


Fig. 4a. From Fig. 3a, showing the result of measuring strain rate $\dot{\epsilon}$ with increasing gauge length l . The dots show the individual measurements; the open circles show the mean values; the crosses show the spread defined by the mean absolute deviation.

Figure 4b corresponds to Figure 3b. At the selected point P the strain rate measured from the smoothed curve is $2.5\% \text{ day}^{-1}$. For $l = 10 \text{ km}$ one finds $\dot{\epsilon} = 2.7 \pm 2.8\% \text{ day}^{-1}$; for $l = 50 \text{ km}$, $\dot{\epsilon} = 2.4 \pm 1.4\% \text{ day}^{-1}$; and for $l = 100 \text{ km}$, $\dot{\epsilon} = 2.4 \pm 0.4\% \text{ day}^{-1}$. Thus, in this case, a gauge length of 100 km is needed if the large-scale strain rate is to be measured with an accuracy of $0.4\% \text{ day}^{-1}$.

Figure 4c corresponds to Figure 3c. Since the smoothed curve in Figure 3c is a straight line there is no selected point P ; all points have the same smoothed strain rate, which is $1.07\% \text{ day}^{-1}$. For $l = 10 \text{ km}$ one finds

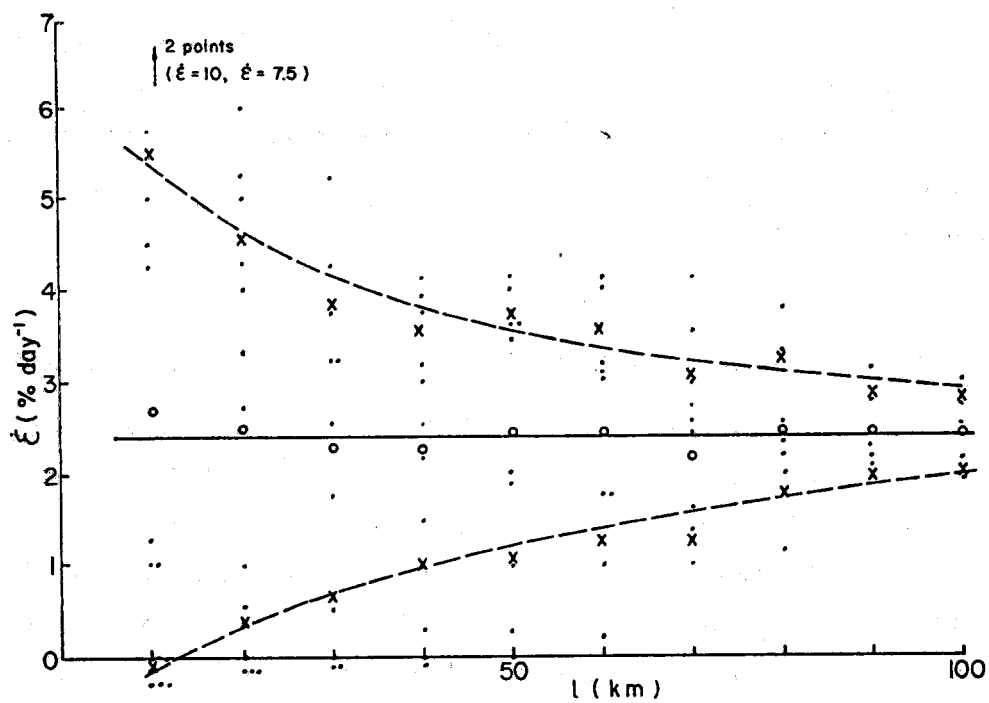


Fig. 4b. The same, from Fig. 3b.

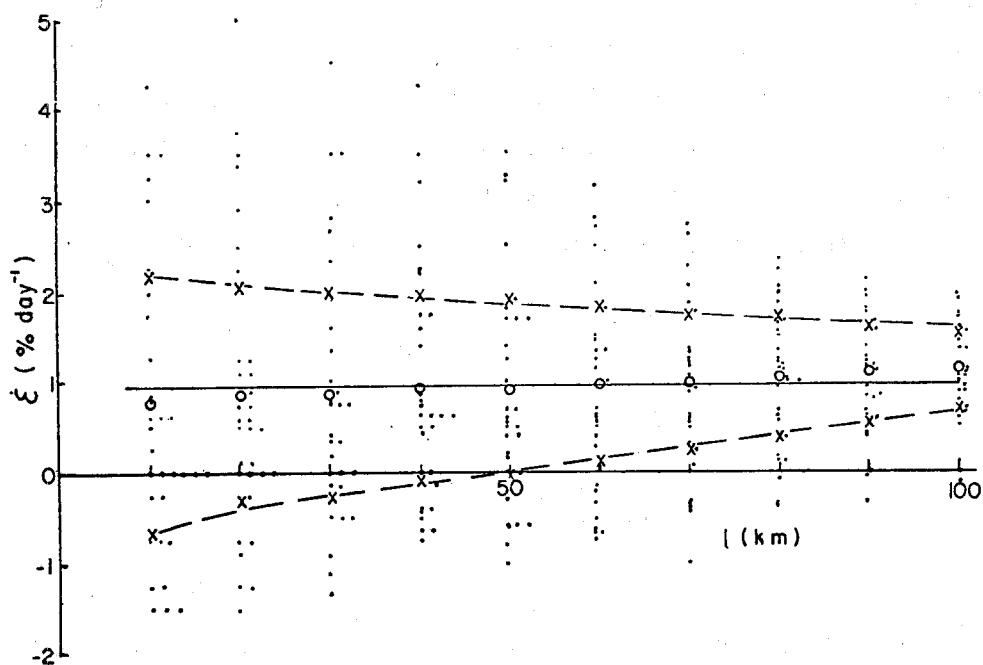


Fig. 4c. The same, from Fig. 3c.

$\dot{\epsilon} = 0.7 \pm 1.4\% \text{ day}^{-1}$; for $l = 50 \text{ km}$, $\dot{\epsilon} = 0.9 \pm 1.0\% \text{ day}^{-1}$; and for $l = 100 \text{ km}$, $\dot{\epsilon} = 1.1 \pm 0.4\% \text{ day}^{-1}$. It is interesting that, in spite of the apparent smaller size of the floes in this case, the scatter of the strain-rate measurements is much the same as before. The dependence of scatter on l shown in Figures 4a, 4b, and 4c may be compared with the $l^{-1/2}$ dependence suggested by Hibler et al. [1973].

5. HOW MUCH MOVEMENT INFORMATION DO THE ERTS PICTURES CONTAIN?

Let us suppose that ERTS-B is launched in time, and let us suppose that it produces the same number of usable pictures for 1975 that ERTS-A produced for 1973. How much useful information on displacement, velocity, and deformation would then be available to test the AIDJEX model during the Main Experiment? To answer this question we have examined the coverage given by the 1973 pictures in the Data Bank (which were already selected to have nominally 30% or less of cloud cover). We considered only a region approximately equivalent to the one within the projected outer ring of data buoys.

There are 199 pairs of pictures which show acceptable overlap (this is defined so that the center of one picture is within 100 km of the center of the other--the pictures are $180 \text{ km} \times 180 \text{ km}$) and which are separated by one to five days. We chose a maximum of five days so that the average velocity deduced for the interval may not be too far from the actual velocities during the interval. The distribution of the pairs by month is as follows:

March	76
April	62
May	42
June	15
July	4
August	0
September	<u>0</u>
Total	199

Thus, assuming some corresponding features can be identified--which is a reasonable assumption--displacement, and hence velocity, could be measured on each of these 199 pairs.

It might be an advantage to have the velocity measurements of a number of points all at the same time. There are 22 pairs of pictures which show acceptable overlap, are separated by one to five days, and whose interval includes the day 21 April 1973. The same conditions are satisfied by 21 pairs for 21 March 1973, 12 pairs for 25 May 1973, 11 pairs for 5 May 1973, and 10 pairs for 6 April 1973.

One might try to follow the same point on the ice for a long time. Let us suppose that a feature will always be recognizable after an interval of 18 days. Starting with a certain latitude and longitude, we ask whether there is a series of pictures, each with this geographical point not more than 100 km from its center, at intervals of never more than 18 days. For 25 different starting points the lengths, in days, of the longest sequences of this sort were as follows:

		LONGITUDE (degrees west)				
		156.0	148.5	141.0	133.5	126.0
LATITUDE (degrees north)	79	37 days	2	36	4	1
	77	1	36	19	94	54
	75	1	22	95	73	37
	73	20	38	38	72	19
	71	0	0	0	0	0

The number 25 was chosen because roughly 25 ERTS pictures would be needed to cover the AIDJEX area. A given latitude and longitude is not the same as a given ice feature—but the lengths of the sequences should be much the same for the two cases.

These numbers give some idea of the coverage that might be expected between March and August 1975 if ERTS-B is launched in time.

6. ICE DEFORMATION FROM ERTS PICTURES DURING THE MAIN EXPERIMENT

The work described was a preliminary study. The measurements should be repeated more carefully, using proper positive transparencies instead of makeshift transparencies from the office photocopier, to see whether the pictures selected for measurement were properly representative; but probably the result will have the same general character. In the three examples studied there is a large-scale spatial variation of ice velocity on a scale of many hundreds of kilometers; smaller-scale variations of velocity are superimposed on this, but their amplitude is not enough to obscure the large-scale trend. We conclude from this that the adoption of a continuum model is justified.

Let us assume now that this result, obtained from the three examples studied from 1973, is indeed general and let us see what the implications may be for the use of ERTS photographs to give deformation during the Main Experiment in 1975. If the weather in 1975 follows the same pattern as in 1973, the amount of cloud-free coverage will be good for March, April, and May: February may also come into this category, but we have not seen pictures for February. June will be possible (see, for example, Fig. 3c), but July, August, and September will be very unfavorable.

During the period of good coverage one could try to measure the strain over intervals of from one to five days by simply superimposing pictures and measuring strain on gauge lengths of 50 to 100 km. It is important to notice that this will give a two-dimensional averaging of the strain; it would be like averaging not only over the one-dimensional distribution in Figure 3a, but over many similar distributions such as Figures 3a and 3b. In other words, the two-dimensional averaging will help to minimize the discontinuities arising from wide leads.

In addition to observing strain in this way and comparing with the predictions of the AIDJEX model, one might try to observe displacement. The difficulty here is the 1-2 km uncertainty in how to superimpose the pictures, which arises from the uncertainty of latitude and longitude. The error in joining pictures together on the same strip is relatively small, and therefore this displacement error is systematic over the whole strip,

in the sense that the displacement components u and v have an error that varies linearly over the field.

There are two ways in which this error may be wholly or partly removed. The first is the obvious one, that if the strip contains visible land features these can be used to correct the apparent displacements; but unfortunately land will only rarely be seen on the usable strips. The second way makes use of the AIDJEX manned camps and the data buoys, which we shall call prime points; strips will not infrequently include one or more of these. The positions of prime points will be known by independent means probably to better than 0.1 km. However, to make use of the information for our purpose it is *not* necessary to identify the exact position of a prime point on the ERTS photograph; no ground marking of the prime points is needed in this application. The changing position data from a prime point tell us its displacement, and so we know that *some* point on the ERTS image within a 2 km square has that displacement. We can now assume that the nearest identifiable ice feature (say, within a few kilometers) has that same displacement. This tells us how we must superimpose the two successive ERTS images at that point, and so removes the systematic error in displacement at that point. The method works because, although 2 km is an uncomfortably large error in displacement $u(x,y)$ or $v(x,y)$, it is of little importance as an error in the position (x,y) where the displacement is measured.

In a strip like that of Figure 3a there will be a systematic error in displacement of some 2 km, which for u is uniform along x and for v is linear in x . If the strip contained a prime point, the systematic error in u would become effectively zero (that is, about the same as the 0.1 km random error), but there would still remain a systematic error in v which increases linearly with x as one leaves the prime point. If the strip contains two prime points (perhaps a manned camp and a data buoy), the displacement would be tied down at two points and the systematic errors in both u and v would become effectively zero.

For accurate values of the derivative $\partial u/\partial x$ no prime points are needed, but to obtain $\partial v/\partial x$ free from systematic error two prime points are required.

If it proves possible to obtain strain by two-dimensional averaging over pairs of single photographs, this will be a great advantage, because pairs of strips of usable photographs, showing the necessary overlap and separated by the requisite time interval, will be rarer. However, it is possible that at certain times the required averaging distance will be so large that strips must be used. In this case a possible method would be simply to measure the ice velocity at a few points in each $100 \text{ km} \times 100 \text{ km}$ square, taking the view that the details of the velocity variations within a square are not really relevant to the AIDJEX model, and that the amplitude of the small-scale velocity variations is small enough for a measurement at a single point to be reasonably representative. For example, the broken curve in Figure 3a could be reasonably well determined by measuring five points spaced at 100 km intervals. (Alternatively, the average displacement over a 100 km square could be obtained directly by making a best fit visually over the area.) This method would enable one to find the large-scale $\partial u / \partial x$ without significant systematic error. However, if the displacement component v at one end of a 500 km line is systematically wrong by 2 km, relative to the displacement at the other end, the error in $\partial v / \partial x$ is 0.4%. Thus, without prime points, a large-scale value of $\partial v / \partial x$ of $2\% \text{ day}^{-1}$ could be measured to 10% accuracy over a two-day interval, to 5% accuracy over a four-day interval, and so on. The use of two prime points would remove these systematic errors in $\partial v / \partial x$.

The other disadvantage of using strips, besides their relative rarity, is that they do not give any improvement on information about y derivatives. This restriction arises because the ERTS orbit which gives the strips of photography always runs from NE to SW. There is, however, another part of the orbit which runs from SE to NW, which is not normally used for gathering pictures because it occupies the dark face of the Earth. However, in summer in the Arctic this part of the orbit is in daylight and could, in theory, give very useful additional coverage for the AIDJEX Main Experiment. If pictures could be transmitted from it they would double the coverage, and, in particular, they would provide strips parallel to Oy which would enable the derivatives $\partial u / \partial y$ and $\partial v / \partial y$ to be obtained just as well as $\partial u / \partial x$ and $\partial v / \partial x$.

7. AIRCRAFT PHOTOGRAPHS AS AN ALTERNATIVE TO ERTS

Should ERTS-B not be available during the Main Experiment, it is worth considering whether photographs from a high-flying aircraft, positioned by inertial navigation, might be used to provide essentially similar information. If the flights were arranged so that they always passed over a manned station or data buoy whose position is known, the error in position on the rest of a straight flight path could probably be reduced to much less than 2 km. Thus, a photograph from an altitude of 20 km, with the aircraft held reasonably horizontal, could be used to fix the position of an ice feature to the necessary accuracy. When the flight was repeated a few days later, over the same station or buoy, overlap between the successive strips of pictures would be assured.

A more elaborate method that would give greater accuracy in strain measurements would be to use aerial photogrammetry. The method we propose here differs from the conventional one in the important respect that it measures strain without making any use of ground control. It goes as follows. The aircraft takes one picture from point P and another a little later from point P' , with sufficient overlap between the pictures that they may be used as a stereo pair. Although the exact attitude of the camera (pitch, roll, and yaw angle) at P and at P' is unknown, and although the altitude may be different at P and P' , when the resulting pictures are placed in a standard stereo-plotting machine and rotated relative to one another there is only one relative orientation of the two pictures that will give stereo reconstruction of the scene, namely, the relative orientation they had when they were taken; at any other relative orientation the two views will not fuse. (It is interesting to note that this theorem is true in three dimensions, but not in two.) At this stage we see in the stereo-plotter a tilted view of the ice pack. It will be essentially a plane, because that is the nature of the scene, but a tilted plane. Since we know that the plane is in fact horizontal, we now rotate the two photographs together until the reconstructed scene is horizontal.

A map can now be made of the ice detail, but it will have no North pointer and no scale. The North pointer is not essential for our purpose. On the other hand, we must know the scale, and this is the crucial point.

Since there will normally be no ground control (which is the usual way of obtaining the scale) we must measure some length. This could be the altitude of the aircraft at P or P' , or it could be the length PP' . In either case if we wish the scale of the map to be accurate to 0.1% we must measure whatever length is chosen to this same accuracy. Aircraft altimeters are not usually designed to be accurate to 0.1% at heights of 10 or 20 km. The length PP' could be derived from the true ground speed of the aircraft together with the time interval between the pictures, but it might be more accurate to obtain it from the inertial navigation system of the aircraft. The length PP' , together with the calibration constant of the stereoplotter, fixes the scale of the map.

A few days later a similar flight line is flown to pass over the same ice features. A second stereo-pair is taken in the same way and a map is produced on the same scale as before. The strain of the ice in the time interval between the two flights is then deduced, to an accuracy of about 0.1% strain, by superimposing the two maps.

The rotation will not be known unless both maps carry North pointers. The azimuth of PP' on the two occasions could probably be obtained to the necessary accuracy of 0.001 radian by again making use of the inertial navigation system of the aircraft.

8. CONCLUSION

Thus, in summary, our measurements on the ERTS 1973 photographs support the adoption of a continuum model for the pack ice, and they suggest that velocity or strain-rate measurements adequate for the purposes of the AIDJEX model will be readily obtainable during spring 1975 from ERTS-B pictures, provided of course that the satellite is operating. If it is not, it may be possible to obtain ice velocity and strain rate from aircraft photographs, either by locating geographically the same ice feature at intervals of a few days, or by using our suggested stereophotogrammetric scheme without ground control.

We should like to thank M. Kettleson and S. Rolfe for giving us valuable help in making some of the measurements described in this report.

REFERENCES

- Barnes, J. C., and C. J. Bowley. 1974. The application of ERTS imagery to monitoring arctic sea ice. ERT Document 0408-F, February 1974. Type III report, June 1972-December 1973, prepared for NASA by Environmental Research and Technology, Lexington, Mass. 02173.
- Crowder, W. K., H. L. McKim, S. F. Ackley, W. D. Hibler, and D. M. Anderson. 1974. Mesoscale deformation of sea ice from satellite imagery. *Advanced Concepts and Techniques in the Study of Snow and Ice Resources*, pp. 563-573, US-IHD, National Academy of Sciences, Washington, D.C.
- ERTS Data User's Handbook. 1972. Document No. 71SD4249, NASA-Goddard Space Flight Center, Greenbelt, Maryland 20771.
- Hibler, W. D. III, S. F. Ackley, W. K. Crowder, H. L. McKim, and D. M. Anderson. Analysis of shear zone ice deformation in the Beaufort Sea using satellite imagery. *Symposium on Beaufort Sea Coastal and Shelf Research, San Francisco, California, January 1974*. Arctic Institute of North America, Washington, D.C. (in press).
- Hibler, W. D. III, W. F. Weeks, A. Kovacs, and S. F. Ackley. 1973. Differential sea ice drift I: Spatial and temporal variations in sea ice deformation. *AIDJEX Bulletin No. 21* (July 1973), 79-113. (In press, *Journal of Glaciology*.)
- Nye, J. F. 1973. The meaning of two-dimensional strain-rate in a floating ice cover. *AIDJEX Bulletin No. 21* (July 1973), 9-17.
- Nye, J. F. 1974. Three notes on the theory of sea-ice movement. *AIDJEX Bulletin No. 23* (January 1974), 37 (first note).
- Rothrock, D. A. The mechanical behavior of pack ice. *Annual Review of Earth and Planetary Sciences*, vol. 3, section on Kinematics (in press).
- Shapiro, L. H., and J. J. Burns. Satellite observations of sea ice movement in the Bering Strait region. *Symposium on Beaufort Sea Coastal and Shelf Research, San Francisco, California, January 1974*. Arctic Institute of North America (in press).
- Stateman, M. 1974. ERTS-1 imagery acquired by the AIDJEX Data Bank. *AIDJEX Bulletin No. 25* (July 1974), 29-48.
- Swithinbank, C. 1973. Satellite view of McMurdo Sound, Antarctica. *Polar Record*, 16(105), 851-872.

THE REMOTE SENSING PROGRAM REQUIRED FOR THE AIDJEX MODEL

by

W. F. Weeks

*U.S. Army Cold Regions Research and Engineering Laboratory
Hanover, NH 03755*

Max D. Coon

*AIDJEX, University of Washington
Seattle, WA 98105*

and

W. J. Campbell

*Ice Dynamics Project, USGS
Tacoma, WA 98416*

INTRODUCTION

The remote sensing program associated with the main AIDJEX experiment has three purposes:

1. Collection of the data that are required for the operation of the AIDJEX ice dynamics model.
2. Collection of basic remote sensing documentation of the AIDJEX study area. (Although this information is not required for the AIDJEX model as now envisioned, it would serve as the basis for an expanded analysis incorporating factors that are neglected at present; at the very least, it would serve as valuable documentation of the ice under study.)
3. Operation of remote sensing experiments that, although not immediately related to AIDJEX, use AIDJEX as a vehicle to expand our general knowledge of remote sensing techniques as applied to the study of sea ice.

The difficulties in formulating an optimum AIDJEX remote sensing program lie in obtaining all the requisite data for purpose 1 while at the same time obtaining the best compromise program relating to purposes 2 and 3. Purpose 3 is particularly important in that organizations such as NASA and

the Canadian Centre for Remote Sensing must justify their participation in the proposed field experiment primarily on the strength of their internal instrument development programs rather than their direct contributions to the purposes of AIDJEX.

In this document we discuss only the first purpose: that of obtaining the remote sensing data *requisite* to the operation of the AIDJEX model. Within this limit, we examine the kinds of data needed, the question of the best sensors for particular requirements, ground truth, the frequency and types of missions, and data analysis. This report will serve as the first step in the formulation of an overall AIDJEX remote sensing plan.

REQUIREMENTS FOR THE MODEL

The independent determination of the ice thickness distribution by using remote sensing techniques is of paramount importance to the successful operation of the AIDJEX model and is the foremost problem that must be faced in developing an AIDJEX remote sensing program.

The present AIDJEX ice dynamics model has been well described [Coon et al., 1974]. It models pack ice by an elastic-plastic constitutive law which utilizes an ice thickness distribution as a state parameter. In this sense the ice thickness distribution, G , refers to the fractional area of ice thinner than a given thickness. As such, G serves as a parameter from which both the elastic behavior (elastic moduli) and the plastic behavior (size and shape of the yield surface) can be determined. The ice thickness distribution also controls the thermal coupling between the ocean and the atmosphere, and a knowledge of its value permits a determination of the mass balance. However, in this report we will concentrate primarily on the relationship of G to the mechanical response of pack ice.

The ice thickness distribution is controlled by two processes: the thermal growth and ablation of ice of all thicknesses (growth rates are much higher for thinner ice); and the mechanical redistribution of ice by the opening of leads (creation of open water) and the formation of ridges. The ridges are composed of the thinner ice that forms in frozen leads. Thin ice is the ice most changed

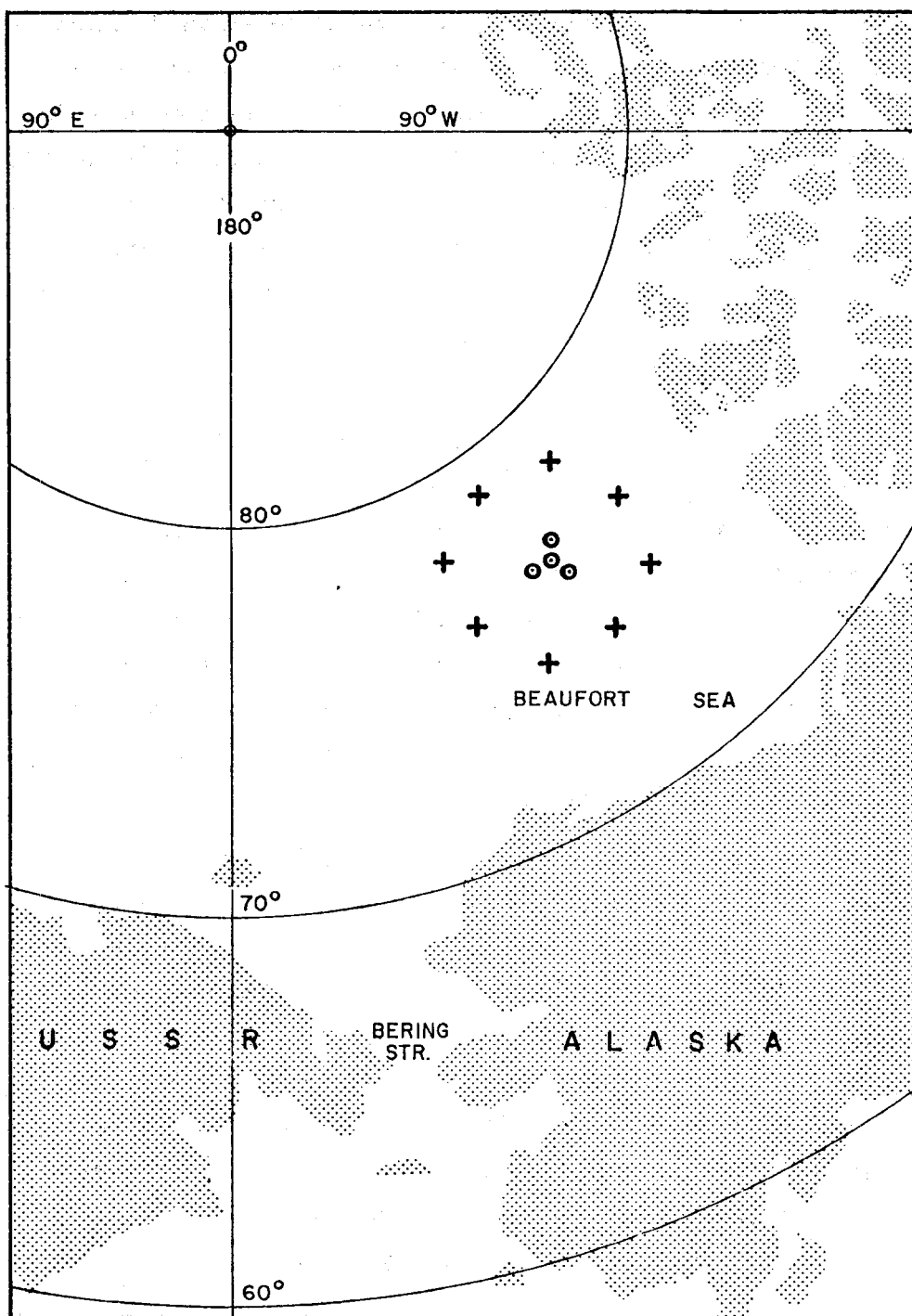
by thermal and mechanical effects, and it is also the part of the ice thickness distribution that is most closely related to the plastic response (yield stress for the ice).

The differential equation for G can be driven by the mechanical strain rates for the area being considered and by the thermal conditions (temperature field) and energy fluxes that control ice growth and ablation. Therefore, this equation serves as a submodel in the AIDJEX plan and can be tested separately if the deformations of an area can be measured at the same time that the ice thickness distribution is being measured. Below we suggest that within the triangular array of manned camps of the AIDJEX main experiment such experiments should be run to test the ice thickness distribution equation separately from the other components of the general AIDJEX model.

Another view of the ice thickness distribution equation is as one member of the general equations; here the ice thickness distribution is required as an initial condition for all elements of the AIDJEX ocean (the area inside the ring of buoys) to provide solutions to the various differential equations. Also, if the G component of the general equations is to be checked in general, then other readings (at other times) of the ice thickness distribution must be noted throughout the AIDJEX ocean. This is the other portion of the ice thickness distribution experiment that will be considered below.

The second requirement for remote sensing data arises from the need for expanded strain information throughout the AIDJEX ocean.

The collection of strain information is one of the main purposes of AIDJEX. These data will come primarily from determining the relative motions of the four manned stations and data buoys. However, it is highly desirable to be able to expand this strain network during two or three representative periods by determining the motion of a large number of identifiable points both within the 100 km manned triangle and throughout the AIDJEX ocean. Because of the large size of the area of interest and the prohibitive cost of obtaining this information from additional data buoys, this is an ideal area to utilize remote sensing techniques, including satellite- and aircraft-borne photography.



Configuration of the AIDJEX main experiment. Data buoys are represented by crosses, manned stations by circled dots. The AIDJEX ocean is the area within the ring of buoys.

The analysis of this photogrammetrically determined strain information will permit AIDJEX to resolve conclusively the scale, if any, upon which arctic pack ice can be modeled as a continuum. It is quite possible that this scale changes with weather conditions and the time of year. Because this experiment requires the sensing of strains on many scales, photogrammetric data are ideal, since such data permit one to measure strain on many scales. The fluctuations in the velocity field due to both the discrete nature of pack ice and the presumed random nature of small-scale interfloe movements will also be both observable and of interest.

In addition, the detailed strain information will allow studies to be made of the response of the pack as a function of ice morphology. It is to be expected that the ice thickness distribution will show significant variations across the AIDJEX ocean and perhaps even within the 100 km manned triangle. These variations in G should lead to different responses in the ice motion. Using the controlled sequential imagery that will be obtained for the strain study, the deformation rates in regions of differing G can actually be measured and compared with the response predicted by the AIDJEX model. This will provide valuable insight into the sensitivity of the model.

Finally, the photographic coverage resulting from the expanded strain study will make a major contribution to the second purpose of the AIDJEX remote sensing program mentioned in the introduction: it will carefully document the nature of the ice under study. In recent experiments, especially in the Arctic, it has been found that often the lack of complete and carefully controlled photographic coverage of the area under study severely limits the utility of the acquired experimental data. This is particularly true in investigations that extend beyond the scope of the originally envisioned uses of the data. Considering the complexities of the problem that AIDJEX proposes to resolve, one can be certain that such extensions will occur.

The last remote sensing requirement is the attainment of a quantitative description of the roughness of both top and bottom surfaces of sea ice during several different times of the year.

Again because of the large areas of ice involved, information on surface roughness can be obtained only by remote sensing. The reason for wanting such

data is simple. The wind stress is the main force driving the drift of the ice, and the water stress acts as a drag. To be able to estimate either of these quantities with confidence, one must be able to determine the average drag coefficients of both upper and lower surfaces of the ice. Present research indicates that this can be done given adequate profile data. The stresses calculated in this manner can then be compared with stresses calculated by bulk boundary layer methods. For instance, if variable deformation is observed within the AIDJEX array, it could be produced by variations in the wind velocity field, variations in G (primarily caused by changes in the thin portions of the ice cover), or variations in the surface roughness (primarily caused by changes in the thick part of the cover). To be able to separate these effects is highly desirable.

The best method for obtaining the roughness of the upper surface utilizes an airborne laser. The lower surface, on the other hand, could best be studied with an upward-looking sonar system based on a nuclear submarine. Because the chances of obtaining submarine observations appear to be small, bottom roughness will probably have to be estimated from the laser profile of the upper surface. These roughness measurements are not only important in their own right, but they also provide valuable information on the nature of the ice thickness distribution.

In summary, we believe that the remote sensing programs that are absolutely required for the proper operation of the AIDJEX model are those that relate to (1) specifying the ice thickness distribution, (2) establishing detailed strain arrays within the AIDJEX ocean for representative periods of time, and (3) determining the top and bottom roughness of the ice pack.

Checking the Model

It should be noted that the verification of the AIDJEX model will be accomplished by model calculations involving the ice enclosed by the ring of unmanned data buoys in the main AIDJEX experiment. The observed drift of the manned stations can serve as a check on the motion and strain of one element of this calculation.

A similar calculation can be accomplished by using the outer portion of the buoy ring and the Alaskan and Canadian coasts as defining an area of interest. In this case, several of the buoys in the buoy ring will be internal to the area of interest. But what is more important is that this kind of calculation will involve a portion of the shear zone. Therefore, it will allow the model to be checked against various boundary conditions as they appear during the year; for example, specified displacement conditions in the winter when the ice extends all the way to shore and stress-free conditions in the summer when the ice pack has receded from the shore. Since no deformation data will be taken directly in the shear zone as part of AIDJEX, any remote-sensed data that can be taken to help define the deformation in this region will be a great help to the modelers. Also, tracking the ice edge during the summer months can be useful in the model in two ways: (1) the location of the boundary can then be specified as a function of time and serve as input to the model; and (2) a more sophisticated check on the model can be attempted by using the model to predict the location of the ice edge. To accomplish the above will fortunately not require new remote sensing techniques. It will, however, require some thought as to the optimum scheduling of sensors and the designation of flight paths.

ICE THICKNESS DISTRIBUTION

For ice thickness distribution measurements we must be able to measure--from either line track or strip imagery--the percentage of the line or area that is covered by a given thickness of ice. At the least the imagery should resolve ice thickness in the ranges of open water (or "no ice"), 0-20 cm, 20-100 cm, and above 100 cm (with the last category also showing the amount of heavily ridged ice). Higher thickness resolution is, of course, highly desirable. The size resolution should be 10 m; that is, all elements greater than 10 m in width must be distinguished. The relative importance of the thickness classes mentioned above varies with the season. In the late fall, winter, and early spring, the thin ice and open water categories are most important because of their pronounced effect on the plastic behavior

of the ice. In the late spring, summer, and early fall, the most important category to be distinguished is simply open water. As will be seen below, these differences in the relative importance have a major influence on the choice of the optimum sensor or sensors for a given time of year.

The choice of a sensor is also related to cloud and light conditions throughout the year. The lack of light in late fall, winter, and early spring, when thin ice and open water must be sensed, dictates the choice of a sensor that can identify thin ice and open water without visual light, e.g., an IR sensor. However, in the late spring, summer, and early fall, the cloud cover in the Arctic is heavy, and a sensor should be able to penetrate the clouds. Here, the best sensors may be microwave and radar, and it is extremely important that they sense open water, if not ice categories.

A. Sensor Package

It should be realized that there is at present no operational remote sensing system that is capable of directly obtaining the thickness of sea ice from an aircraft. Therefore, although considerable progress had been made recently on this problem [Adey et al., 1972; Adey and Reed, 1973; Campbell and Orange, 1974], it is necessary for planning purposes to assume that ice thickness estimates during AIDJEX will have to be made by indirect methods. In view of this, the sensors of potential interest are visual light photography, IR imagery, microwave radiometry, SLAR, and sonar and laser profiles.

1. Spring-summer-early fall

As we mentioned, during spring, summer, and early fall it is necessary to have a sensor that operates through the clouds and provides good areal estimates of the relative amounts of ice and open water. It would, of course, be desirable to be able to differentiate several classes of ice thickness. The reason this is not mandatory is that the vast majority of thinner ice will have melted completely in the early summer leaving only multiyear ice

and open water. Microwave radiometry, SLAR, and radar scatterometry have the capability of fulfilling these requirements.

Ice and water are easily differentiated in microwave imagery such as that obtained by NASA during the spring 1972 AIDJEX program. It is also possible to differentiate first-year from multiyear ice. Whether this distinction can be made during the summer melt period as well is not yet known; if it can, it will be a useful bonus. Microwave systems now in use also have the advantage of imaging a wide expanse of sea ice on a given pass. The groups with a suitable microwave system and aircraft capability are NASA and the U. S. Coast Guard.

SLAR systems such as the APS-94 X-band system also give good estimates of the amount of open water. SLAR distinguishes water from ice by the smoothness of a water surface as opposed to the roughness of an ice surface. Again it should be possible to obtain some information on the amount of newly formed ice in frozen leads, because new ice can usually be distinguished from open water. SLAR has the advantage of imaging a wide swath of sea ice (50 km) on each pass. It would be desirable to have some limited photographic imagery that can be correlated with the SLAR imagery so that any questions in the interpretation of the SLAR can be resolved (at present most SLAR flights have been made under fall or winter conditions). Organizations possessing suitable SLAR systems are the U. S. Geological Survey and the Canadian Armed Forces.

Another useful sensor for summer conditions is the radar scatterometer. Recent field tests [Texas A & M, 1973] indicate that all-weather scatterometry systems are capable of differentiating between open water, first-year ice, and multiyear ice. The principal drawback to the system now being used is that it samples only a narrow strip (3° beam width). Again, some aerial photography would be almost mandatory as an interpretative aid. In fact, standard photography should be obtained whenever possible as an interpretative aid to analyzing almost all other imagery. The scatterometer system of interest is operated by the Remote Sensing Center of Texas A and M University.

In summary, for the late spring-summer-early fall time period microwave imagery would appear to be the preferable system, although SLAR also seems

quite attractive. Radar scatterometry is of less interest because of the narrowness of its area samples, but it would nevertheless be a useful addition.

2. Late fall-winter-early spring

Late fall-winter-early spring is the time period for which the determination of the ice thickness distribution G is essential. The difficulties are caused by the fact that open water as well as at least three ranges of ice thickness must be differentiated (0-20 cm, 20-100 cm, > 100 cm) and that it is dark much of the time. In general, however, the weather can be expected to be clear.

Several systems should be helpful in determining G . The most important of these seems to be a thermal IR that has a fixed dynamic calibration. Inasmuch as such IR systems give a direct determination of the temperature of the upper ice or snow surface, it is possible, in principle, to directly calculate the ice thickness distribution from the imagery. In practice, however, this is not possible because of varying amounts of snow on the surface of the sea ice. Therefore, the gray scale on the IR image only corresponds to a relative thickness scale. With a simple "ground truth" program that measures ice thickness in a number of identifiable locations, it should be possible to calibrate the gray scale so that it becomes a thickness scale, because although snow cover is not a unique function of ice thickness, equivalent ice thicknesses will have equivalent snow covers in a given area of the Arctic Ocean. Once the thickness of a uniform area of sea ice is identified, it should be easy to calculate the ice thicknesses at later times from simple empirical equations and near-surface meteorological information.

Organizations having suitable IR equipment are NASA and the U. S. Geological Survey. The NASA equipment is mounted in a Convair 990 that is capable of long-range high-altitude flights over the whole AIDJEX ocean. The USGS equipment, on the other hand, is mounted in a Beaver that can fly low-level detailed surveys within the manned triangle of stations. Presumably the Beaver could be based at the main manned station for short periods of time.

The Beaver as presently configured does not have photographic capability. This is unfortunate because standard aerial photography is the next most useful method of estimating ice thickness (light permitting). For thin sea ice the gray scale on the photograph can be used to estimate ice thickness. This is particularly true if areas of known thickness are present in the photograph. For thicker ice (> 40 cm), the snow drift patterns can be used to identify ice of similar thickness, while multiyear ice (> 2 m) is usually indicated by its characteristic rolling surface topography. Another advantage of photography is that, with the exception of the Beaver, all the remote sensing aircraft involved in AIDJEX are capable of obtaining it.

A third useful input to estimating G can be provided by laser profilometry. A laser ranger when flown in a low-flying aircraft (< 1000 m) can obtain highly detailed profiles of the upper surface of the ice (or snow). The measurement error even in rough profiles is believed to be less than 10 cm. By suitable filtering procedures [Hibler, 1972] the aircraft motion can be removed from the profile, leaving an accurate representation of the surface topography of the ice. By using open water areas as frequent reference levels (open water can be identified unambiguously by measuring the strength of the laser return), accurate running estimates can be made of the freeboard of the ice. In undeformed ice the freeboard plus the density provide the ice thickness. In multiyear ice areas, predictive methods using a variable ice density specified by the freeboard combined with a 10 m "wide" linear filter are effective. Recent studies [Ackley et al., 1974] indicate that the error in predicted ice thicknesses obtained by using the latter method is only 10% greater than the error obtained by direct surface measurements. The problem with laser profilometry is that only a profile is sampled. Nevertheless the thickness estimates on undeformed ice areas are capable of being extended laterally by correlations using either thermal IR or standard photography. Airborne laser capability is now available in the NAVOCEANO, NASA, and Canadian Ice Reconnaissance aircraft.

It would be desirable to be able to directly determine the bottom profile of the ice. This can be done by using an upward-looking sonar system based on a nuclear submarine [Lyon, 1963; Swithinbank, 1972]. Such a submarine would have essentially unlimited range, would be capable of

operations during any time of year, and could move with ease over any prescribed track north of the edge of the continental shelf. Unfortunately, if past experience is any guide, the chance of obtaining a nuclear submarine to take the required sonar data, even during one time of the year--much less three or four times--is small, so that at present we must assume that sonar data will not be available.

It is also desirable to have microwave and SLAR data from flights made during the late fall, winter, and early spring: microwave images would provide valuable large-scale information on the distribution of open water, first-year and multiyear ice [Campbell et al., 1973] while the SLAR results would allow studies of the ridging patterns. However, neither of these two sensors can be considered of principal importance in the determination of G during this period.

In summary, the IR flights are clearly the most important for determining G during the late fall-winter-early spring period, and it is highly desirable that the IR information be supplemented by laser profiles and, when light permits, by aerial photography.

B. Ground Truth

The ground truth measurements needed for the ice thickness distribution studies are quite simple. The thickness of a number of ice categories, ranging from open water to ice of roughly 1 m thickness, must be measured, presumably by drilling, at several locations that can be identified easily in the imagery. The remote sensing flights would then be sure to cover each of the calibrated areas, and the calibration associated with the areas near the manned camps (i.e., various gray levels on photography or on IR) would be extrapolated to the rest of the AIDJEX ocean. The ground truth could be conducted using AIDJEX aircraft and on-site personnel. Laser profiles can also be used as checks on these correlations at sites distant from ground control.

C. Remote Sensing Missions Related to the Ice Thickness Distribution

It would be desirable to have continuous monitoring of G throughout the entire AIDJEX ocean. Since such data acquisition and reduction is clearly impossible, remote sensing flights are suggested that cover ice conditions during late fall (freeze-up), winter (maximum rate of ice growth), early spring (maximum ice thickness), late spring (thaw), and summer (melt).

Within each set of flights two types of missions should be carried out. In one, the area within the manned array is sampled to check the submodel of the ice thickness distribution. The differential equations associated with these calculations are time dependent; therefore, if the model is to be both initiated and tested, an initial condition and at least one subsequent time check on the ice thickness distribution are required. Thus, a minimum data set should include two different determinations (in time) of the ice thickness distribution within the manned area. To be realistic, however, a minimum of three determinations, separated from each other by a few days, are desirable. Coverage of the manned array should be as complete as possible.

The other type of mission involves more broad-scale sampling across the AIDJEX ocean to provide data for the general model. It is important to get several data sets--three or four--for each season in order to initiate and check the calculations of the time-dependent differential equations. Because we cannot possibly get complete coverage of the AIDJEX ocean in these experiments, specific sampling plans will have to be developed that obtain maximum utilization of both the platform and the sensor.

Table 1 presents a "schedule" of aircraft for the AIDJEX remote sensing missions. The only purpose of this table is to illustrate the problems that must be worked out to develop an adequate schedule. In the sensor listings the first sensor for a given aircraft is the most important. There is no significance to the listing sequence of aircraft. Under "Study Area," *outer* refers to flights across the entire area encompassed by the outer ring of data buoys (the AIDJEX ocean), while *inner* refers only to the area circumscribed by the manned stations. In developing a final plan, considerable thought will have to be given to juggling availability of aircraft against the time a specific sensor is needed.

TABLE I: "SCHEDULE" OF AIDJEX REMOTE SENSING FLIGHTS RELATING
TO THE ICE THICKNESS DISTRIBUTION AND SURFACE ROUGHNESS DETERMINATIONS

Time of operation	Operating agency	Aircraft	Main sensors	Study area	Base of operations	Number of flights
early spring	NASA	990	IR, photo, laser microwave	outer and inner	FAI	5
	USGS	Beaver	IR	inner	Ice camp	5
	NAVOCEANO	P-3	Laser, photo	outer	BRW	2
	CCRS	C-47	Scatterometer, photo microwave, IR	inner	YEV*	3
	DND	Argus	SLAR, IR	outer and inner	YEV	2
	NCAR	Electra	Meteorological sensors	outer and inner	FAI	5
	NASA	U-2	Photo	inner	FAI	5
	AIDJEX	Helicopter	Microwave, radiometer radar	inner	Ice camp	10+
late spring	DOE	Electra	Laser, photo	inner	YEV	2
	USGS	Mohawk	SLAR, photo	inner	BRW	2
	AIDJEX	Helicopter	Microwave, radiometer radar	inner	Ice camp	10+
summer	NASA	990	Microwave, photo	outer	FAI	5
	USGS	Mohawk	SLAR, photo	outer	BRW	4
	DND	Argus	SLAR, photo	outer	YEV	2
	AIDJEX	Helicopter	Microwave, radiometer radar	inner	Ice camp	6
fall	NASA	990	IR, photo, laser microwave	outer and inner	FAI	5
	CCRS	C-47	Scatterometer, photo microwave	outer and inner	YEV	3
	NCAR	Electra	Meteorological sensors	outer and inner	FAI	5
	NAVOCEANO	P-3	Laser, photo	outer	FAI	2
	NASA	U-2	Photo	inner	FAI	5
	USGS	Beaver	IR	inner	Ice camp	5
	AIDJEX	Helicopter	Microwave, radiometer radar	inner	Ice camp	10+
winter	NASA	990	IR, laser, microwave	outer and inner	FAI	5
	USGS	Beaver	IR	inner	Ice camp	5
	USGS	Mohawk	SLAR	inner	BRW	5
	DND	Argus	SLAR, IR	outer and inner	YEV	2
	AIDJEX	Helicopter	Microwave, radiometer radar	inner	Ice camp	10+

*Inuvik

D. Data Reduction

The AIDJEX modeling group has considered the general problem of measuring the ice thickness distribution from several types of two-dimensional imagery (primarily NASA aerial photography), in specific, the use of line data or strip data in evaluating the ice thickness distribution. Although the discussion of data reduction in this section centers around the use of visual light photography, it is clear that the discussion could apply equally well to any sensor. The idea is to sense the amount of area covered by a given shade of gray and relate that shade of gray to a given ice thickness.

Such problems have been attacked previously in several ways. It is possible to digitize each two-dimensional image and do computer analysis of the digitized image, but this method is too costly for a production operation in AIDJEX. Other techniques involve human interpretation in some form. The most direct form is that of actually tracing around a given area of gray level to determine its area. This might be done with a simple hand planimeter or with a pencil-following digitizer in conjunction with a minicomputer. The second of these alternatives is very desirable, in that a hard copy of the area traced can be obtained. The errors associated with this data reduction have two sources: the ability (or inability) of a person to trace a given area, and the problem of interpreting gray levels. A considerable amount of the 1972 NASA data has been processed in this manner, but it is a slow, costly process that is hardly ideal for processing the extensive data from the main experiment.

Other automated methods involving human interpretation have been examined by Heiberg and Bell (personal communication). These methods use equipment on which the contrast (either gray level or false color) in an image can be adjusted so that desirable features are of a given gray level or color. Then the amount of that area is automatically calculated. Such a method does have the advantage of human intervention; that is, one can make adjustments for such things as cloud cover by adjusting the color or gray level on each frame. However, there are real disadvantages (with, for example, the 1972 NASA photography) because of the halo effect, i.e., the changing value of gray with distance from the center of the photograph. Similar problems

are encountered in SLAR imagery. It is important that these varying gray levels be taken care of by proper lenses and processing.

In the 1975-76 experiment, as much information must be collected as possible in a way that facilitates automatic processing. Considerable additional thought should be given to this problem. It is, however, our impression that completely automatic processing methods will not be adequate for our data analysis purposes.

When we refer in this paper to the ice thickness distribution at various elements in the AIDJEX ocean, we are assuming that we can sample part of, say, a 100 km² element and adequately estimate the ice thickness distribution without actually measuring all the ice of a given thickness in the entire element. Nor do we want to have to measure the ice thickness distribution in every 100 km element; we want to measure it in a few and extrapolate between elements. Work is now underway to evaluate different sampling procedures and extrapolation techniques. For example, we are studying data obtained from a small number of strips in a 100 km element (covering only a fraction of the actual area) and trying to relate these values to those for the entire 100 km element. Also, work is being done in investigating the sampling errors involved in utilizing line data to calculate the ice thickness distribution in a 100 km element.

In connection with these sampling problems, there is a critical question of how accurately we must know the ice thickness distribution in the first place. To this end, parameter studies are underway on the AIDJEX model that involve varying the ice thickness distribution and seeing how it affects the actual deformation and subsequent ice thickness values that are given by the model. One problem with the ice thickness measurement is that there are three kinds of errors: (1) the error in the actual measurement of the amount of area associated with a given ice thickness (gray scale on the image); (2) the error associated with judging how thick the ice corresponding to that gray scale actually is; and (3) the error caused by the limited resolution of the sensor.

Once the data reduction problems have been solved and parameter studies completed, tentative flight programs for the remote sensing flights can be

worked out. This should be completed by August 1974 so that there is adequate time for discussion with the remote sensing groups that will be involved.

STRAIN

There are two types of strain studies that should be carried out to supplement the strain measurements that will be obtained from the data buoys and the manned array. The purposes of both studies are similar. They differ primarily in the scales and the resolution of the imagery, and in the control that the experimenter has over the time that the data is obtained.

A. Studies by Satellite Imagery

The most important satellite in this regard is ERTS. It images an 160 x 160 km area on a given photograph (actually the imagery is obtained as a continuous strip) with very little distortion. High contrast linear features having widths of roughly 30 m are clearly visible in the imagery. Uncertainties in the satellite orbit will cause errors of about 2 km in the measurement of the displacement of observable ice features. On the other hand, relative displacements of between 100 and 200 m should be observable. Therefore, a 1% strain can be detected with a gauge length of 10 km while a gauge length of 100 km is required for strain of 0.1%. These accuracies depend upon being able to identify the same feature at different times. Nye and Thomas [1974]] have found that by lengthening the period of observation one at first gains in precision as the strain increases, but then one loses precision as the identifying features become less distinct.

Several highly useful strain studies that apply indirectly to AIDJEX have already been made using ERTS imagery (Crowder et al., 1973; Hibler et al., in press; Shapiro and Burns, in press; Nye and Thomas, 1974]. A complete set of deformation parameters can be calculated from observations of the relative ice motions. In addition, information can be obtained on the homogeneity of the deformation, on the angularity and size distribution of interacting floes,

and on the orientation, spacing, density, width distribution, and branching angles of observable leads and polynyas.

There are problems with the ERTS system: imagery is not obtained during cloudy or dark periods; many small leads cannot be seen on the photos; and, at the latitudes where AIDJEX will operate, imagery is presently available only for a 4-day period (one image per day) followed by a 14-day data gap before the satellite returns. This last problem may have a solution. During an arctic summer of continuous daylight, the satellite can obtain two images per day instead of one. Moreover, the light conditions required for "turning on" the satellite are those necessary for photography over a land surface; since sea ice provides a highly reflective surface separated by dark areas (leads) of high contrast, adequate photography is possible with very low light levels.

Requests should be made to NASA so that the above facts are used in implementing an expanded ERTS data collection activity in the Arctic while the AIDJEX project is in the field. A systematic effort should be made to obtain and to analyze all ERTS imagery that is available from the area where AIDJEX will operate. Arrangements should also be made to obtain "near real time" ERTS imagery during the period that the field experiment is active. The analysis of these data will provide a valuable background against which to study the detailed motions of the AIDJEX array.

The above studies should also utilize imagery from NOAA 2 and NOAA 3 and the Defense Meteorological Satellite Program (DMSP). These satellites add broad-scale information on the movement of the pack throughout most of the Arctic Basin [Ackley and Hibler, in press; Streten, 1974], and they image the Arctic on a much more frequent and regular basis than does the ERTS satellite. The main features that can readily be observed via the NOAA and DMSP imagery are the lead patterns. Therefore, the images can serve as useful checks of the predictions of the AIDJEX model about the direction of leads.

By combining the results of the NOAA 2 and NOAA 3, DMSP, and ERTS systems with the results of the manned strain array, AIDJEX has the capability of looking at sea ice on a variety of scales. The analysis should prove

valuable in checking the predictions of the AIDJEX model. The data are available at little cost. The only problem is arranging support for the analysis of the imagery, which is time-consuming and requires manpower.

B. Studies Using High-Elevation Aircraft

To supplement the satellite program, it is desirable to perform an additional photogrammetric experiment over the area of the AIDJEX array. The experiment would utilize either U-2 or RB-57 aircraft, which fly at 60,000-70,000 feet. Flights would be made in 1975 during two separate two- or three-week periods. The first would be in late February or early March when the ice has reached its maximum extent, and the second would take place in late May or early June when the pack starts to loosen up. Approximately five flights would be made in each period, with the exact timing of the flights depending on the weather and the observed ice deformation. Each mission would consist of three straight-line passes over the AIDJEX manned array with each pass containing the main camp and one of the smaller stations. Since the ground width of the photo-track is roughly 30 km, these three flight lines image essentially the complete 100 km triangle. Assuming 60% overlap, it will take from eight to ten photographs to cover each flight line.

To control the photographs made in such flights, large identifiable targets will be placed on the ice at some distance (15-20 km) from the main camp and the distances between the camp and the targets measured by a laser ranger during the overflights. It is also possible that a shorter identifiable distance can be measured in the vicinity of the satellite camps. Leveling control on the photographs will be obtained by using sea level (in leads) as a reference level. Then, starting with the calibration distances in the photograph containing the main camp, phototriangulation procedures will be used to prepare an accurate (0.1%) strip photomap. Selected clearly identifiable ice features (such as lead edges and bends in pressure ridges) will be used as bridging points. When the lines between the same stations are flown again, the changes in length between points identifiable on both strip maps can then be used to study the nature of the pack ice velocity field.

The prime purpose of this experiment is to provide information on the detailed behavior of the pack as a function of ice morphology. The variations in the ice thickness distribution G over the 100 km triangle should lead to different responses in the ice motion. Also, it is within the 100 km triangle that the variations in G should be best specified. Using the controlled mosaics, the deformation rates in regions of different G can be measured. These actual rates are then compared with the responses predicted by various deformation models in order to compare the sensitivity of the models with the actual local ice response. The experiment will also permit the examination of spatial scaling effects down to quite small scales and will permit a much more detailed examination of the distribution of leads and floes than is possible with satellite imagery. In fact, a comparison between the U-2 imagery and the ERTS imagery will provide interesting information on the degree to which ERTS underestimates the amount of thin ice in a given area.

The U-2 experiment offers several advantages to the collection of strain data. The time of the flights can be specified by the experimenter in order to obtain maximum information about the ice motion. Its imagery has a very high resolution: objects 2 m in length can be identified. And during each experiment the laser measurements around the main AIDJEX camp will be made as frequently as conditions permit; during some periods, target determinations will be made on a continuous basis. These measurements will provide AIDJEX--at no extra cost--with two brief periods of high-frequency deformation data that would otherwise be missing completely from the measurement program.

Finally, the controlled photogrammetric experiment within the 100 km triangle will provide a calibration against which to test a photogrammetric way to obtain strain (Nye, personal communication) without ground control. This technique should be possible if either aircraft elevation or the distance between successive photographs is known "exactly." If the RB-57, which has an inertial guidance system, is used for the flights, it may be possible to implement this approach. If successful, this technique would allow photogrammetric strain experiments to be performed anywhere over the polar pack ice, independent of the availability of ground calibration.

SURFACE ROUGHNESS

The reasons, as well as the methods, for obtaining roughness profiles of the top and bottom surfaces of sea ice have already been discussed. As we noted, the basic data required for this program would be collected because of their usefulness in estimating the ice thickness distribution even if roughness were not of interest. Then it remains only to analyze the roughness data and make the necessary estimations of surface drag coefficients using the methods discussed by Banke and Smith [1973] and Hibler and Mock [1973]. The software packages required for this analysis have been developed and are available at CRREL and NAVOCEANO. The only problem is obtaining support for the analysis.

It should be noted that even when the laser (and sonar?) data are analyzed and converted into suitable drag coefficients, it will be worthwhile to work out the best way of calculating the regional averages required in the modeling efforts. Quite probably this will be done by first making a correlation between ice type, drag coefficient, and the time of year and then producing a weighted average based on the relative proportions of ice types in the study area. Fortunately the data required to produce these averages will be collected by other parts of the remote sensing program.

CONCLUSION

In this document we have attempted to present the requirements of the AIDJEX remote sensing program as it relates to developing an improved numerical model of the drift and deformation of sea ice. This report will serve as part of the input (which will also include the availability of sensor systems and platforms, as well as the particular research interests of the participating organizations) that is necessary to formulate an overall AIDJEX remote sensing plan. We expect to present the final version of this plan to the AIDJEX Committee in October 1974.

REFERENCES

- Ackley, S. F., and W. D. Hibler. Measurements of Arctic Ocean ice deformation and fracture patterns from satellite imagery. *SCOR/SCAR Polar Oceans Conference, Montreal, Quebec, May 1974* (in press).
- Ackley, S. F., W. D. Hibler, F. K. Kugzruk, A. Kovacs, and W. F. Weeks. 1974. Thickness and roughness variations of arctic multiyear sea ice. *IEEE Ocean '74 Conference, Halifax, Nova Scotia, 21-23 August 1974*. Institute of Electrical and Electronics Engineers, New York, N.Y.
- Adey, A. W., T. R. Hartz, R. E. Barrington, W. Rolfe, and W. E. Mather. 1972. Theory and field tests of a UHF radiometer for determining sea ice thickness. Communications Research Centre of Canada, Tech. Note No. 637, Ottawa, Ontario, Canada.
- Adey, A. W., and G. N. Reed. 1973. Radio frequency radiometry as a remote sensing technique in maritime reconnaissance and marine sciences in a northern environment. Communications Research Centre of Canada, Tech. Note No. 660, Ottawa, Ontario, Canada, 18 pp.
- Banke, E. G., and S. D. Smith. 1973. Wind stress on arctic sea ice. *Journal of Geophysical Research*, 78(33), 7871-7883.
- Campbell, K. J., and A. S. Orange. 1974. A continuous profile of sea ice and freshwater ice thickness by impulse radar. *Polar Record*, 17(106), 31-41.
- Campbell, W. J., P. Gloersen, W. Nordberg, and T. T. Wilheit. 1973. Dynamics and morphology of Beaufort Sea ice determined from satellites, aircraft, and drifting stations. NASA-Goddard Space Flight Center, Preprint X-650-73-194, Greenbelt, Maryland, 21 pp.
- Coon, M. D., G. A. Maykut, R. S. Pritchard, D. A. Rothrock, and A. S. Thorndike. 1974. Modeling the pack ice as an elastic-plastic material. *AIDJEX Bulletin No. 24*, 1-106. Univ. of Washington, Seattle, Wash.
- Crowder, W. K., H. L. McKim, S. F. Ackley, W. D. Hibler, and D. M. Anderson. 1974. Mesoscale deformation of sea ice from satellite imagery. *Advanced Concepts and Techniques in the Study of Snow and Ice Resources, Monterey, California, 2-6 December 1973*. National Academy of Sciences, Washington, D. C., pp. 563-573.
- Hibler, W. D. 1972. Removal of aircraft altitude variation from laser profiles of the arctic ice pack. *Journal of Geophysical Research*, 77(36), 7190-7195.
- Hibler, W. D., and S. J. Mock. 1974. Classification of sea ice ridging and surface roughness in the Arctic Basin. *Advanced Concepts and Techniques in the Study of Snow and Ice Resources, Monterey, California, 2-6 December 1973*. National Academy of Sciences, Washington, D.C., pp. 244-254.

- Hibler, W. D., S. F. Ackley, W. K. Crowder, H. L. McKim, and D. M. Anderson. Analysis of shear zone ice deformation in the Beaufort Sea using satellite imagery. *Symposium on Beaufort Sea Coastal and Shelf Research, San Francisco, California, January 1974, Arctic Institute of North America, Washington, D.C. (in press).*
- Lyon, W. 1963. The submarine and the Arctic Ocean. *Polar Record*, 11, 699-705.
- Nye, J. F., and D. R. Thomas. 1974. The use of satellite photographs to give the movement and deformation of sea ice. In this *Bulletin*.
- Shapiro, L. H., and J. J. Burns. 1974. Satellite observations of sea ice movement in the Bering Strait region. *Symposium on Beaufort Sea Coastal and Shelf Research, San Francisco, California, January 1974, Arctic Institute of North America, Washington, D.C. (in press).*
- Streten, N. A. Large-scale sea ice features in the western Arctic Basin as viewed by the NOAA-2 satellite. *Journal of Arctic and Alpine Research (in press).*
- Swithinbank, C. 1972. Arctic ice pack from below. In *Sea Ice: Proceedings of an International Conference, Reykjavik, Iceland, 10-13 May 1971*, ed. T. Karlsson. National Research Council, Reykjavik, Iceland, pp. 246-254.
- Texas A and M University. 1973. Radar studies of arctic ice and development of a real-time arctic ice type identification system. Remote Sensing Center, Texas A and M University, College Station, Texas. NOL Contract N60921-72-C-0076, 154 pp.

ELASTIC STRAIN IN THE AIDJEX SEA ICE MODEL

by

Robert S. Pritchard
AIDJEX

ABSTRACT

The AIDJEX sea ice model is extended by a careful consideration of the deformation measured relative to a reference configuration which changes according to the plastic flow. This approach makes the strain more meaningful than it was previously. The kinematic relations properly allow both finite stretch and rotation. The resulting kinematic relation reflects the feeling that sea ice response is independent of any fixed reference configuration. This formulation has been achieved by writing an incremental kinematic relation using the Finger deformation tensor. A special relation is presented for the case when elastic strain is small, as with sea ice. The elastic response and yield criterion as well as the plastic flow rule remain unchanged from those presently in use. The flow rule is derived by maximizing the rate at which plastic work is done. This approach unifies the development and also helps us to study the material instabilities that occur when the material softens. The material model satisfies the principle of material frame indifference. The model has been subjected to known deformation histories and the response is satisfactory. In many cases the stress history is indistinguishable from that of the previously used elastic-or-plastic model.

INTRODUCTION

The AIDJEX Modeling Group has developed a mathematical model to describe the motion of arctic sea ice on length scales of 100 km [Coon et al., 1974]. Our choice of an elastic-plastic representation was justified by considering the microscale processes that occur on smaller length scales. Here, we take for granted the physical justification of an elastic-plastic response and

This work was funded by National Science Foundation Grant OPP71-04031 to the University of Washington to support the Arctic Sea Ice Study.

concern ourselves with improving the model so that it works in more general deformations.

The shortcoming of the material model presented in Coon et al. [1974] is in the kinematics. The elastic strain was not defined in terms of the motions, and the assumed form does not provide an elastic response that is invariant under rotation of the material. Furthermore, the simpler elastic-or-plastic model used for actual calculations does not provide a continuous stress history for a given continuous strain rate history. In one- or two-dimensional dynamic problems these discontinuities are unsatisfactory. Upon deriving the kinematics, we find it necessary and desirable to present the entire mechanical response. This allows us to apply a unified approach to the derivation and to determine what parts of the model may be generalized.

In the following sections we discuss other plasticity representations and then use them to improve the AIDJEX model. The crucial development is in the kinematic relations. However, all elements of the elastic-plastic material response are presented: kinematics, elastic response and yield surface, and the flow rule. These topics are considered in separate sections. Then the kinematics are simplified by assuming small elastic strains. Finally, the model is tested by subjecting it to a prescribed deformation history. Results of these calculations are presented in the form of yield strength and stress path histories.

BACKGROUND

The literature is rich with elastic-plastic constitutive laws. Our kinematic relations depend on the work of Lee [1969, 1971], Herrmann [1969], Haddow and Hruday [1971], Wang [1973], and Hahn [1974]. In those works, elastic strain was introduced in terms of deformation relative to a moving reference configuration. To accomplish this derivation we require three configurations (Fig. 1): a fixed reference configuration \underline{k} , the configuration occupied by the body at each time $\underline{\Gamma}$, and an intermediate reference configuration $\underline{\Gamma}_p$ that changes in time according to the plastic flow. The elastic response follows the work of Naghdi and Trapp [1974]. Deformation between the instantaneous configuration and the elastic unload configuration

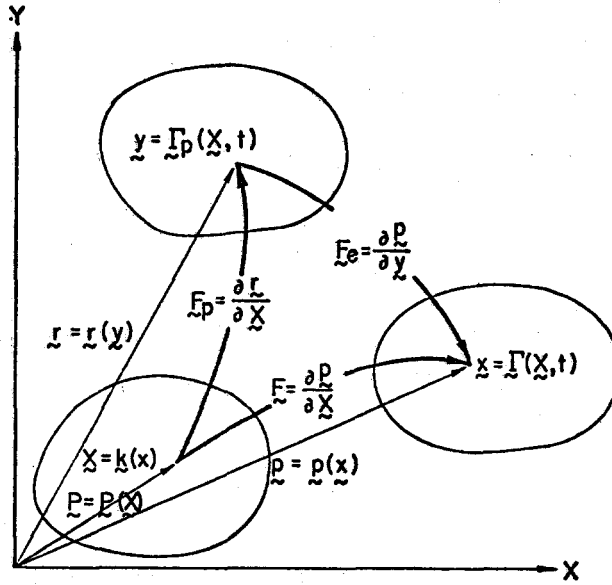


Fig. 1. Relationship between three configurations defining strain.

provides the strain measure influencing the elastic response. The yield surface depends on one parameter as in many other geologic materials, but the parameter is different from those used for soils or rocks [Nelson, Baron, and Sandler, 1971]. As a result, the material may either harden or soften and is unstable in the sense of Drucker [1950]. Such materials are discussed by Palmer, Maier, and Drucker [1967]. The general elastic-plastic model of Green and Naghdi [1965] and limitations imposed by Green and Naghdi [1971] are also useful. We attempt to take the best parts of these models and combine them into a sea ice model.

We are interested in predicting the motion of sea ice that is constrained to lie on the surface of the ocean. Thus particle velocity $\tilde{v}(\tilde{x}, t)$ is the time rate of change of position $\tilde{x} = \tilde{\chi}(x, t)$ on the sea surface, where x and t indicate the particle x at time t and $\tilde{v} = \dot{\tilde{x}}$. The velocity gradient $\tilde{L} = \partial \tilde{v} / \partial \tilde{x}$ is a second-order tensor with four components in the two-dimensional problems. The stretching is obtained as $\tilde{D} = 1/2(\tilde{L} + \tilde{L}^t)$ and the spin as $\tilde{W} = 1/2(\tilde{L} - \tilde{L}^t)$. We identify material particles x by position \tilde{x} in the reference configuration $\tilde{x} = \tilde{k}(x)$, again a two-dimensional space. Generally, the reference configuration is the actual configuration at the initial time

of interest. The deformation from the reference configuration is $\underline{\Gamma}$, where $\underline{x} = \underline{\Gamma}(\underline{X}, t)$, the position at time t occupied by particle X which occupies position \underline{X} in the reference configuration.

The deformation gradient (see Figure 1 for the geometric interpretation)

$$\underline{F} = \frac{\partial \underline{x}}{\partial \underline{X}}$$

provides the information necessary to measure both strain and rotation. By the polar decomposition theorem [Truesdell and Toupin, 1960]

$$\underline{F} = \underline{R} \underline{U} = \underline{V} \underline{R}$$

where \underline{R} is the rotation tensor, \underline{U} is the right stretch tensor, and \underline{V} is the left stretch tensor. The material rate of change of \underline{F} is a function of the velocity gradient

$$\dot{\underline{F}} = \underline{L} \underline{F}$$

We may now introduce a completely analogous set of quantities related to the moving reference configuration, called the elastic unload configuration, indicated here by $\underline{y} = \underline{\Gamma}_p(\underline{X}, t)$. Specifically, we have a deformation gradient $\underline{F}_p = \partial \underline{x} / \partial \underline{X}$, which decomposes into $\underline{F}_p = \underline{R}_p \underline{U}_p = \underline{V}_p \underline{R}_p$, and a plastic velocity field \underline{v}_p with velocity gradient $\underline{L}_p = \partial \underline{v}_p / \partial \underline{y}$, which decomposes into plastic stretching $\underline{D}_p = 1/2(\underline{L}_p + \underline{L}_p^t)$ and spin $\underline{W}_p = 1/2(\underline{L}_p - \underline{L}_p^t)$. The meaning of each of these quantities is clear because each is defined in a manner completely analogous to those introduced in the deformation from the fixed reference to the final configuration.

We now introduce the deformation from the elastic unload configuration to the final configuration

$$\underline{x} = \underline{\Gamma}[\underline{\Gamma}_p^{-1}(\underline{y}, t), t]$$

The elastic deformation gradient \underline{F}_e is a measure of change between these two configurations

$$\underline{F}_e = \frac{\partial \underline{x}}{\partial \underline{y}}$$

The three different deformation gradients \tilde{F} , \tilde{F}_p , and \tilde{F}_e are related by

$$\tilde{F} = \tilde{F}_e \tilde{F}_p$$

KINEMATICS USEFUL TO THE SEA ICE MODEL

In the previous paragraphs, we have discussed several deformation measures. Two of these were defined with respect to an arbitrary, but fixed, reference configuration and the third with respect to a moving reference configuration. Components of each measure may be interpreted in terms of physically meaningful and measurable quantities.

According to Pritchard [1974], most investigators feel that sea ice has no preferred configurations and thus no reference configuration that arises naturally. This fact leads us to formulate the material response independently of any fixed reference configuration.

In the mechanical constitutive law, the material properties and the yield surface are assumed to depend on the history only through the ice thickness distribution at the present time. Even at the microscale level, it is seen that any preferred configuration is "forgotten by the material" whenever a lead or ridge is formed. In the mathematical description of the constitutive law, the absence of a preferred configuration is evidenced by the fact that strain rate, not strain, influences the stress state.

We want a formulation of incremental kinematics involving our physically interpretable variables, \tilde{F}_e , \tilde{L} , and perhaps \tilde{L}_p . The elastic deformation gradient is not measured relative to a fixed configuration, and we cannot automatically introduce all the previous variables; instead, we must calculate them by inferring their relationship from previously derived variables. For instance, the material time rate of change of \tilde{F}_e is $\dot{\tilde{F}}_e$ and is obtained from

$$\dot{\tilde{F}} = \dot{\tilde{F}}_e \tilde{F}_p + \tilde{F}_e \dot{\tilde{F}}_p$$

Substituting for $\dot{\tilde{F}}$ and for $\dot{\tilde{F}}_p$ in an analogous manner, we find that

$$\dot{\tilde{F}}_e = \tilde{L} \tilde{F}_e - \tilde{F}_e \tilde{L}_p$$

We could use this equation to determine $\underline{\dot{F}}_e$, except that \underline{L}_p cannot be determined. As many authors have shown, a degree of uncertainty exists in the deformation decomposition, that is, in deciding how much of the rotation to call elastic and how much to call plastic. And once the decision is made, another question arises: how do we evaluate the effect of that apportionment on the plastic velocity gradient \underline{L}_p so that we can evaluate $\underline{\dot{F}}_e$?

We circumvent this difficulty by introducing the Finger deformation tensor [Truesdell and Toupin, 1960]:

$$\underline{B}_e = \underline{F}_e \underline{F}_e^t$$

which, by the polar decomposition theorem, is also

$$\underline{B}_e = \underline{V}_e^2$$

Taking the material rate of change of \underline{B}_e and substituting the expression for $\underline{\dot{F}}_e$ gives

$$\dot{\underline{B}}_e = \underline{L} \underline{B}_e + \underline{B}_e \underline{L}^t - 2 \underline{F}_e \underline{D}_p \underline{F}_e^t$$

The most important feature in this equation is that the plastic spin does not have to be known to determine $\dot{\underline{B}}_e$. This fact will allow us to make an assumption about the decomposition of \underline{R} into \underline{R}_p and \underline{R}_e without having to determine the effect of that assumption on \underline{W}_p . The final form of the kinematic equation contains the elastic rotation \underline{R}_e , but this will be seen to be satisfactory on derivation of the flow rule.

In most elastic-plastic material models used to describe response of metals the plastic dilatation, $\text{tr } \underline{D}_p$, is assumed zero. This assumption is not made for sea ice. The basic reason is that sea ice is a two-dimensional material and the dilatation is a measure of area change, rather than volume change as in a three-dimensional material. This note of caution is included because our use of the direct notation hides the dimensionality of the problem. We also point out that in this sense the classical plasticity models must be generalized to describe sea ice.

MATERIAL RESPONSE RELATIVE TO CHANGING REFERENCE CONFIGURATION

Material response is assumed to be elastic relative to the changing reference configuration. Stress states are limited by the yield constraint to lie within the yield surface. The elastic response proposed by Coon et al. [1974] is

$$\underline{e} = \frac{1}{4M_1} \underline{1} \operatorname{tr} \underline{g} + \frac{1}{2M_2} \underline{g}'$$

and the yield constraint is

$$\phi(I, II', p^*) \leq 0$$

The stress \underline{g} in this two-dimensional theory is actually the stress resultant. It is the difference between the integral of the Cauchy stress through the thickness of the ice and the hydrostatic load applied by the water in which it floats. The invariants are

$$\begin{aligned} I &= \operatorname{tr} \underline{g} \\ II' &= \operatorname{tr} \underline{g}' \underline{g}' \end{aligned}$$

where

$$\underline{g}' = \underline{g} - \frac{1}{2} \underline{1} \operatorname{tr} \underline{g}$$

The elastic moduli depend on the instantaneous thickness distribution through the mean thickness \bar{h} . As stated previously, p^* is the yield strength, also dependent on G .

The elastic strain \underline{e} is chosen to be the extension

$$\underline{e} = \underline{V}_e - \underline{1}$$

a quantity which may be determined from the kinematic relations derived earlier in this paper.

Both the elastic response and the yield constraint satisfy the principle of material frame indifference [Truesdell and Noll, 1965] and consequently must be isotropic. Therefore, the chosen response is the most

general form acceptable. This could be generalized by allowing the plastic deformation and the instantaneous thickness distribution to affect the elastic response. In a general nonlinear elastic response, the elastic moduli may depend on I and II' .

PLASTIC WORK AND THE FLOW RULE

The flow rule is derived by maximizing the rate at which plastic work is dissipated. This approach has been used by Drucker [1950] and by Hill [1950, 1958]. Although it does not provide a means of demonstrating uniqueness of solution as with stable material [Drucker, 1955; Palmer, Maier, and Drucker, 1967], it does provide a unified approach.

The stress power is (assuming a symmetric stress tensor)

$$\dot{w} = \text{tr } \underline{\underline{\sigma}} \underline{\underline{L}}$$

In terms of our kinematic quantities, this may be written

$$\dot{w} = \text{tr } \underline{\underline{\sigma}} (\dot{\underline{\underline{F}}} \underline{\underline{F}}^{-1} + \underline{\underline{F}} \underline{\underline{L}} \underline{\underline{F}}^{-1})$$

We anticipate simplifications and decompose into elastic part w_e and plastic part w_p

$$w_e = \text{tr } \underline{\underline{\sigma}} \dot{\underline{\underline{F}}} \underline{\underline{F}}^{-1}$$

$$w_p = \text{tr } \underline{\underline{\sigma}} \underline{\underline{F}} \underline{\underline{L}} \underline{\underline{F}}^{-1}$$

The plastic working (rate at which plastic work is done) is written

$$w_p = \text{tr } \underline{\underline{R}}^t \underline{\underline{V}}^{-1} \underline{\underline{\sigma}} \underline{\underline{V}} \underline{\underline{R}} \underline{\underline{L}}_p$$

Eigenvectors of $\underline{\underline{\sigma}}$ and $\underline{\underline{V}}$ are coincident because the elastic response is isotropic. Therefore, the product $\underline{\underline{\sigma}} \underline{\underline{V}}$ is commutative [Wilkinson, 1965] and this simplifies the plastic working to

$$w_p = \text{tr } \underline{\underline{R}}^t \underline{\underline{\sigma}} \underline{\underline{R}} \underline{\underline{L}}_p$$

which is independent of the rate of elastic deformation. Since $\sigma^t = \sigma$, the stress is symmetric, and we find that the rotated stress $\tilde{R}_e^t \sigma \tilde{R}_e$ is symmetric. Thus, only the plastic stretching contributes to the plastic working:

$$w_p = \text{tr } \tilde{R}_e^t \sigma \tilde{R}_e \tilde{D}_p$$

The flow rule results from maximizing w_p for a given deformation subject to the yield constraint. A thorough development for unstable materials is given by Palmer, Maier, and Drucker [1967]. The appropriate normal flow is

$$\tilde{R}_e \tilde{D}_p \tilde{R}_e^t = \lambda \frac{\partial \phi}{\partial \sigma}$$

where λ is a positive scalar multiplier. For the present, the yield surface has been assumed to be convex and to include the origin. We have not yet considered relaxing this limitation.

We point out that the stress response in the present elastic-plastic material is unaffected by the arbitrary choice of \tilde{R}_e . This is consistent with the restriction imposed by Naghdi and Trapp [1974] that the rotation decomposition have no influence on the response.

APPROXIMATION FOR SMALL ELASTIC STRAIN

We now seek to approximate this model for the case when elastic strain ϵ is small. This is important for application of this model to sea ice, in which case elastic strains are thought to be of the order of 0.1 percent. We point out that the elastic response in this application is assumed to be linear, with elastic constants given by

$$M_1 = 10^6 \bar{h} \quad M_2 = \frac{1}{2} \times 10^6 \bar{h}$$

Units of M_1 and M_2 are in newtons per meter and those of \bar{h} are in meters. Furthermore, for notational convenience we let $\tilde{R}_e = \underline{1}$ since the choice does not affect the stress response.

The three kinematic equations are combined to give one differential equation in the elastic strain

$$(\underline{1} + \underline{e})\dot{\underline{e}} + \dot{\underline{e}}(\underline{1} + \underline{e}) = \underline{L}(\underline{1} + \underline{e})^2 + (\underline{1} + \underline{e})^2 \underline{L}^t - 2(\underline{1} + \underline{e})\underline{D}_p(\underline{1} + \underline{e})$$

A systematic approximation technique begins with replacing \underline{e} by $\varepsilon \underline{e}$ for a small constant ε . Then by collecting like powers of ε , we find consistent approximations:

$$\begin{aligned} 2\varepsilon\dot{\underline{e}} + \varepsilon^2(\underline{e}\dot{\underline{e}} + \dot{\underline{e}}\underline{e}) &= \underline{L} + \underline{L}^t - 2\underline{D}_p + 2\varepsilon(\underline{L}\underline{e} + \underline{e}\underline{L}^t - \underline{e}\underline{D}_p - \underline{D}_p\underline{e}) + \\ &\quad \varepsilon^2(\underline{L}\underline{e}^2 + \underline{e}^2\underline{L}^t - 2\underline{e}\underline{D}_p\underline{e}) \end{aligned}$$

The lowest-order approximation is obtained by neglecting terms of order ε and ε^2 to give

$$\underline{D}_p = \underline{D}$$

During plastic flow this is the kinematic relation used in the elastic-or-plastic AIDJEX ice model [Coon et al., 1974].

The next order of approximation is obtained by neglecting terms of order ε^2 while retaining terms of order ε . We find

$$\varepsilon\dot{\underline{e}} = \underline{D} - \underline{D}_p + \varepsilon[(\underline{L} - \underline{D}_p)\underline{e} + \underline{e}(\underline{L} - \underline{D}_p)^t]$$

However, $\underline{L} - \underline{D}_p = \underline{D} - \underline{D}_p + \underline{W}$ and we have already shown that $\underline{D} - \underline{D}_p$ is of order ε when deriving the lowest-order approximation. The terms $\varepsilon(\underline{D} - \underline{D}_p)\underline{e}$ and $\varepsilon\underline{e}(\underline{D} - \underline{D}_p)$ are actually of order ε^2 and may be neglected. The final result is

$$\varepsilon\dot{\underline{e}} = \underline{D} - \underline{D}_p + \varepsilon(\underline{W}\underline{e} + \underline{e}\underline{W}^t)$$

We now return to the original notation and replace $\varepsilon \underline{e}$ by \underline{e} to obtain the following kinematic relation

$$\dot{\underline{e}} = \underline{D} - \underline{D}_p + (\underline{W}\underline{e} - \underline{e}\underline{W})$$

The combination of three terms containing strain may be called the co-rotational strain rate $\overset{\circ}{\underline{e}}$

$$\overset{\circ}{\underline{\underline{e}}} = \dot{\underline{\underline{e}}} - \underline{\underline{W}}\underline{\underline{e}} + \underline{\underline{e}}\underline{\underline{W}}$$

Such a definition is often made for stress [Truesdell and Noll, 1965]. The important feature of $\overset{\circ}{\underline{\underline{e}}}$ is that it is an objective tensor in that it transforms according to the law of second-order tensors during a change of reference frame. We do not use this fact, but it is comforting to find that our kinematic relation for the small elastic strain approximation satisfies all the desired invariance properties.

SAMPLE RESPONSE

All elements of the material response have been presented. We now show how the model behaves by subjecting it to a specified deformation history [Coon and Pritchard, 1974]. Assume that there is no spin ($\underline{\underline{W}} = 0$) and the prescribed stretching $\underline{\underline{D}}$ is uniaxial,

$$\underline{\underline{D}} = \begin{pmatrix} d & 0 \\ 0 & 0 \end{pmatrix}$$

If we subject the body to a period of contraction ($d < 0$) followed by a period of extension ($d > 0$), the features of loading and unloading accompanied by either hardening or softening are observed. The magnitude of d is of no consequence. It affects only the duration of the experiment.

Initially the material is assumed to be stress free and the thickness distribution is uniform up to a thickness of 10 m. This means that each thickness category from 0 to 10 m covers the same area.

$$G(h) = \begin{cases} 0.1 h & 0 \leq h \leq 10 \text{ m} \\ 1 & h > 10 \text{ m} \end{cases}$$

During the test we assume that thickness growth rates correspond to Jan. 1 conditions [Coon et al., 1974]. The yield curve chosen for this work is the polynomial form

$$\phi = II' - \frac{1}{2} I^2 \left(1 + \frac{I}{2p^*}\right) \quad I \leq 0$$

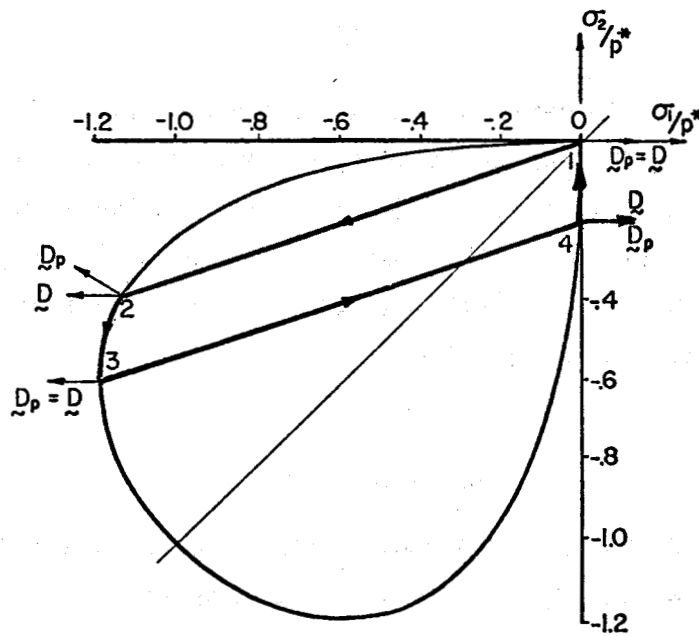


Fig. 2. Stress path during uniaxial contraction and extension.

which is shown in Figure 2 plotted in normalized principal stress space. This type of plot remains unchanged for this yield curve even though p^* changes. This functional form has been used recently by Rothrock [1974] and by the AIDJEX modeling group in sea ice dynamics calculations. In Figure 2 we may draw vectors indicating direction of both the stretching and the plastic stretching. Before discussing the stress path, we introduce Figure 3, which gives the normalized stress-strain response for this uniaxial strain history. With Figures 2 and 3 we can accurately describe the stress response. The path from point 1 to point 2 is elastic, with the slope dictated by the ratio of M_2/M_1 of the form

$$\frac{\sigma_2}{\sigma_1} = \frac{M_1 - M_2}{M_1 + M_2}$$

At point 2 response becomes elastic-plastic. The stretching vector continues to point in the σ_1 direction. The plastic stretching \underline{D}_p becomes non-zero along the path from point 2 to 3. It is normal to the yield curve at each particular point. When point 3 is reached, all stretching is plastic ($\underline{D}_p = \underline{D}$), and this stress state is maintained as long as contraction continues.

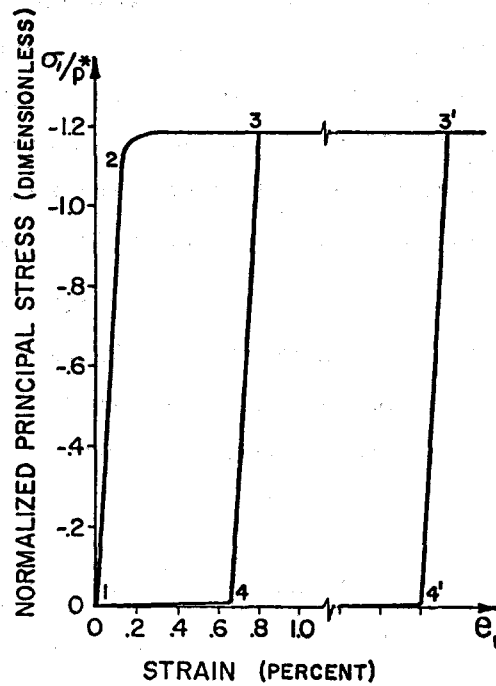


Fig. 3. Normalized stress-strain curves.

In Figure 3 this is shown by the horizontal line from point 3 to 3'. When extension begins, the unloading occurs from point 3 (or 3', depending on the period of contraction). The unloading from point 3 to 4 is elastic. In Figure 3 this slope is independent of the duration at point 3. This is not strictly true, because \bar{h} is modified by plastic flow differently from p^* . Thus, even though both hardening and softening cases may be shown on the one curve by normalizing with respect to p^* , some differences may occur on unloading. We point out that when the body is elastic, only thermodynamic effects can change the thickness distribution and there is no redistribution between ice categories. The final unload from point 4 to 5 closes the stress cycle. The state is elastic-plastic, with \bar{D} and \bar{D}_p shown as before. If the extension continued, the stress would stay at zero and all stretching would be plastic. By this process the strain cycle could also be completed. The normalized forms of these plots have been chosen because the results then appear identical to ideally plastic results.

In Figure 4 we present the yield strength history. The strength increases by approximately 200 percent during the contraction of .5 percent.

It then decreases to less than the initial value when the body is extended by 10 percent. We note that the strain scale on Figure 3 has been grossly distorted to show the unload from point 3'. At strain rates actually used, the experiment duration is 30 days. During this time the yield strength is also increased by the thermal effect of the growth of ice. The yield strength shows the effects of both thermal and mechanical input.

Since hardening occurs when contraction takes place, behavior is stable during contraction. However, on expansion p^* drops and along path 4-5 the behavior is unstable. In normalized stress space, the yield surface is constant. Hence we may use the result from ideal plasticity [Palmer, Maier, and Drucker, 1967] that

$$\text{tr} \frac{d}{dt} \left(\frac{\tilde{\sigma}}{p^*} \right) D_{\tilde{p}} = 0$$

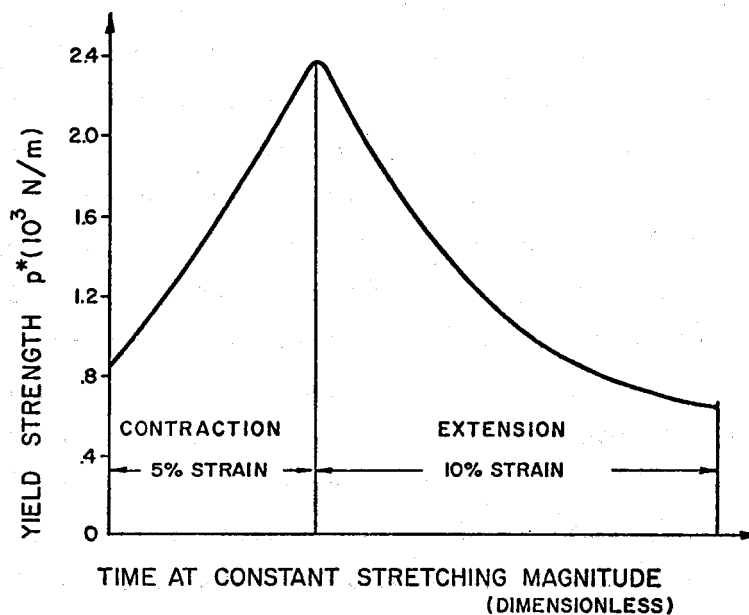


Fig. 4. Yield strength history.

This result depends on the yield surface being constant when expressed in normalized stress space. If we look at material stability in terms of $\text{tr } \dot{\underline{\sigma}} \underline{D}_p$, then

$$\text{tr } \dot{\underline{\sigma}} \underline{D}_p = \frac{\dot{p}^*}{p^*} \text{tr } \underline{\sigma} \underline{D}_p$$

and the sign of \dot{p}^* controls stability of the material because both p^* and the plastic working are non-negative. Thus, softening causes an instability, whether from thermodynamic or from mechanical causes. This is true regardless of both the yield surface shape and the stress state at which flow occurs. This response is expected and anticipated under many conditions, but it is the kind of behavior that must be studied with care.

CONCLUSIONS

The mechanical constitutive law overcomes the objections to the elastic-or-plastic model of Coon et al. [1974]. It gives physical meaning to elastic strain and responds correctly under finite rotations.

We have expressed the constitutive law in terms of the velocity gradient, the kinematic quantity that has meaning to sea ice specialists.

The model is consistent with the continuum mechanics models. It satisfies all invariance requirements.

The model is limited to those materials that have isotropic elastic response and isotropic yield functions.

Although the material model is two-dimensional and derived specifically for sea ice, it has a broader application than that. By including finite deformation and finite plastic dilatation we have developed a model more general than others in the literature.

The incremental formulation is useful in computer programs that solve dynamic problems such as wave propagation or shock mechanics. Kinematic relations take the form of an additional conservation law, the conservation of space (compatibility).

The response to the uniaxial strain shows the desired stresses. We must point out that geophysical materials do not allow laboratory testing of specimens. Therefore, it is difficult to choose between constitutive laws and to judge how good one is. The only test is to obtain solutions to the full field equations under conditions that can be checked by experiment. The AIDJEX Main Experiment will occur from March 1975 to June 1976. During the experiment enough data will be taken to allow us to determine how good the material model is.

Future work includes modifying the flow rule, the yield constraint, and perhaps the elastic response. It is necessary to extend the energetics arguments to include the elastic strain energy and sources due to growth and ablation of surface ice. Better models might need to allow anisotropic behavior (ridges and leads may not be isotropically oriented), and the material response might need to depend on plastic deformation as in the more general theory of Green and Naghdi [1965].

ACKNOWLEDGMENT

The author thanks the AIDJEX staff, especially other members of the ice modeling group, for cooperation during the course of this work.

REFERENCES

- Coon, M. D., G. A. Maykut, R. S. Pritchard, D. A. Rothrock, and A. S. Thorndike. 1974. Modeling the pack ice as an elastic-plastic material. *AIDJEX Bulletin No. 24*, Univ. of Washington, Seattle, pp. 1-106.
- Coon, M. D., and R. S. Pritchard. 1974. Application of an elastic-plastic model of arctic pack ice. *Proceedings of the Symposium on Beaufort Sea Coastal and Shelf Research, January 1974, San Francisco, California*, Arctic Institute of North America, Washington, D.C. (in press).
- Drucker, D. C. 1950. Some implications of work hardening and ideal plasticity. *Quart. Appl. Math.*, 7(4), 411-418.
- Drucker, D. C. 1955. On uniqueness in the theory of plasticity. *Quart. Appl. Math.*, 14(1), 35-42.

- Green, A. E., and P. M. Naghdi. 1965. A general theory of elastic-plastic continuum. *Arch. Ratl. Mech. Anal.*, 18, 251-281.
- Green, A. E., and P. M. Naghdi. 1971. Some remarks on elastic-plastic deformation at finite strain. *International Journal of Engineering Science*, 19, 1219-1229.
- Haddow, J. B., and T. M. Hrudey. 1971. The yield condition and flow rule for a metal subjected to finite elastic volume change. *Journal of Applied Mechanics*, 38, 708-712.
- Hahn, H. T. 1974. A finite-deformation theory of plasticity. *International Journal of Solids Structures*, 10, 111-121.
- Herrmann, W. 1969. Nonlinear stress waves in metals. In *Wave Propagation in Solids*, ed. J. Miklowitz, ASME, 129-183.
- Hill, R. 1950. *Plasticity*. London: Oxford University Press.
- Hill, R. 1958. A general theory of uniqueness and stability in elastic-plastic theory. *Journal of the Mechanics and Physics of Solids*, 6, 236-249.
- Lee, E. H. 1969. Elastic-plastic deformation at finite strains. *Journal of Applied Mechanics*, 36, 1-6.
- Lee, E. H. 1971. Plastic-wave propagation analysis and elastic-plastic theory at finite deformation. In *Shock Waves and the Mechanical Properties of Solids*, ed. J. J. Burke and V. Weiss. Syracuse, N.Y.: Syracuse University Press, pp. 3-19.
- Naghdi, P. M., and J. A. Trapp. 1974. On finite elastic-plastic deformation of metals. *Transactions ASME*, 254-260.
- Nelson, I., M. L. Baron, and I. Sandler. 1971. Mathematical models for geological materials for wave-propagation studies. In *Shock Waves and the Mechanical Properties of Solids*, ed. J. J. Burke and V. Weiss. Syracuse, N.Y.: Syracuse University Press, pp.289-351.
- Palmer, A. C., G. Maier, and D. C. Drucker. 1967. Normality relations and convexity of yield surfaces for unstable materials on structural elements. *Journal of Applied Mechanics*, 34, 464-470.
- Pritchard, R. S. 1974. What? Strain? What strain? *AIDJEX Bulletin No. 26*, Univ. of Washington, Seattle, Wash., pp. 59-74.
- Rothrock, D. A. 1974. The energetics of plastic deformation in pack ice. In this Bulletin. Also submitted to the *Journal of Applied Mechanics*.

- Truesdell, C. A., and W. Noll. 1965. The nonlinear field theories of mechanics. *Encyclopedia of Physics*, III/3, ed. S. Flugge. Berlin: Springer-Verlag.
- Truesdell, C. A., and R. Toupin. 1960. The classical field theories of mechanics. *Encyclopedia of Physics*, III/1, ed. S. Flugge. Berlin: Springer-Verlag.
- Wang, Y. S. 1973. A simplified theory of the constitutive equations of metal plasticity at finite deformation. *Journal of Applied Mechanics*, 40, 941-947.
- Wilkinson, J. H. 1965. *The Algebraic Eigenvalue Problem*. London: Oxford University Press.

THE ENERGETICS OF PLASTIC DEFORMATION IN PACK ICE

by

D. A. Rothrock
AIDJEX

ABSTRACT

A large-scale area of pack ice contains ice of various thicknesses from zero to many meters. Such an area can be modeled as an element of a plastic continuum. As the area deforms, thin ice is ridged into thicker ice in a way that depends on the strain rate and the instantaneous thickness distribution. By equating the plastic work to the production of gravitational potential energy and the frictional dissipation in this ridging process, we relate the size of the yield curve to the thickness distribution and find a constraint on the shape of the curve. The compressive strength p^* evaluated in this way is more than an order of magnitude smaller than the loads required either to crush or to buckle the ice.

INTRODUCTION

Pack ice is an aggregate of many pieces of floating ice sheets. In significant deformation, these pieces override one another, breaking off blocks and forming long sinuous piles of rubble, called pressure ridges, both above the ice, where they become the dominant features, and beneath the ice projecting down into the ocean. The description of the mechanical properties of such an aggregate of floes has been a recognized glaciological problem for more than two decades. Pack ice has been modeled variously as a viscous material [Campbell, 1965], an incompressible, inviscid fluid [Rothrock, 1973], and a cavitating fluid [Nikiforov et al., 1967; Doronin, 1970]. The first theory of pack ice as a plastic material was presented by Coon [1972], who likened the ice in shear to a granular material. To calculate a maximum compressive load p^* , Coon proposed two controlling mechanisms: breaking of pieces in bending by rafting or ridging, and the

buckling of these pieces under the horizontal load. Calculated from these mechanisms, p^* depended on the thickness of ice involved. Thus, Coon presented a family of yield surfaces for different ice thicknesses.

In a closer examination of pressure ridging, Parmeter and Coon [1973] developed a kinematic model in which they retained Coon's mechanism of breaking in bending. The buckling was not modeled; in fact, no stresses in the horizontal plane were considered explicitly. They deduced the horizontal stress by equating the work of this stress to the increase in potential energy in the ridge. As in Coon's theory, this stress depended on the particular thickness of ice being ridged, although in a more complicated way.

It is our purpose here to generalize the energetics arguments of Parmeter and Coon to the case of real pack ice in which ice of many different thicknesses ridges simultaneously. To do so, we refer to the thickness distribution of a large-scale element of pack ice, using the governing equation for this distribution introduced by Thorndike and Maykut [1973]. After defining the plastic work, we will formulate two energy sinks in terms of the thickness distribution: the generation of (gravitational) potential energy and the frictional losses in the rubble pile of a ridge. We neglect two other known energy sinks. The first of these, the loss due to fracture of the ice sheet into blocks as ridging proceeds, was shown by Parmeter and Coon to be negligible. The second is the frictional loss in shearing between floes; we have no estimate of its magnitude, but it is probably no greater than the sinks we are including.

THE PLASTICITY

The elements of plasticity theory which we require here are (1) a yield criterion, $F(\sigma) = 0$, to determine whether plastic behavior can occur, and (2) a flow rule, to relate the plastic strain rate $\dot{\epsilon}^P$ to the stress σ . It should be emphasized that, in our two-dimensional problem, what we call stress has the dimensions of force per unit length and is the difference between the integral of the Cauchy stress through the thickness of the ice

and the hydrostatic load applied by the water in which the ice floats [Nye, 1973; Coon et al., 1974].

For an isotropic material, the orientation of the principal axes of stress cannot affect the response, so the yield criterion can be taken to depend on the principal stresses σ_1 and σ_2 . It is convenient to define invariants σ_I and σ_{II} in terms of the stress tensor and in terms of principal values

$$\sigma_I = \text{negative pressure} = \frac{1}{2}(\sigma_1 + \sigma_2) = \frac{1}{2}\sigma_{ii} \quad (1)$$

and

$$\sigma_{II} = \text{maximum shear stress} = \frac{1}{2}(-\sigma_1 + \sigma_2) = \pm \sqrt{-\det \underline{\sigma}'}. \quad (2)$$

The stress deviator is denoted by $\underline{\sigma}'$:

$$\sigma_{ij}' = \sigma_{ij} - \frac{1}{2}\sigma_{\ell\ell}\delta_{ij}.$$

The σ_I and σ_{II} axes are obtained from the σ_1 and σ_2 axes by a 45-degree rotation and a scaling. The yield criterion is written as $F(\sigma_I, \sigma_{II}) \leq 0$ and defines a yield curve in the (σ_I, σ_{II}) plane (Fig. 1). Actually, $F = 0$ denotes a family of yield curves that depend on one parameter, the

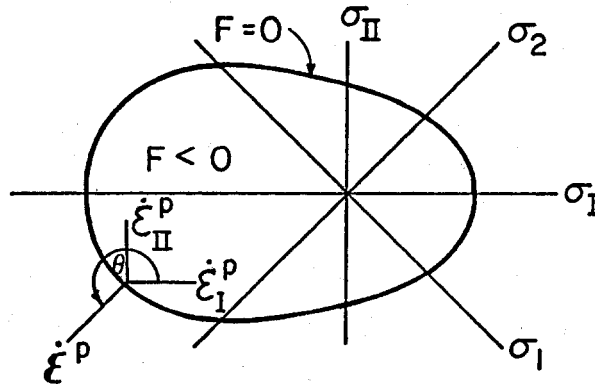


Fig. 1. The yield curve $F = 0$ in the (σ_I, σ_{II}) plane. The stress on the material must lie within or on this curve. The plastic flow rule requires that the plastic strain rate be normal to the yield curve.

compressive yield strength p^* , which is determined by the thickness distribution in a manner we will show. For our present purposes, we need not concern ourselves either with the strain rate decomposition or with the material behavior when the stress lies strictly within the yield curve. (The decomposition and the elastic behavior assumed in Coon et al. [1974] will do.)

To write the flow rule, it is convenient to define the strain rate invariants $\dot{\epsilon}_I^P$ (the divergence of velocity or $\dot{\epsilon}_{ii}^P$) and $\dot{\epsilon}_{II}^P$ (equal to $\pm 2(-\det \dot{\epsilon}^P)^{1/2}$ where $\dot{\epsilon}^P$ is the strain rate deviator). We will subsequently use the modulus of the strain rate $|\dot{\epsilon}^P|$, defined as $[(\dot{\epsilon}_I^P)^2 + (\dot{\epsilon}_{II}^P)^2]^{1/2}$ and the angle θ , defined as $\tan^{-1}(\dot{\epsilon}_{II}^P/\dot{\epsilon}_I^P)$. We use the associated flow rule

$$\dot{\epsilon}_k^P = \lambda \left. \frac{\partial F}{\partial \sigma_k} \right|_{F=0}, \quad k = I, II \quad (4)$$

which states that the plastic strain rate is normal to the yield curve (Fig. 1) but is of unspecified magnitude. Both this flow rule and the convexity of the yield curve follow from Drucker's postulate, which applies whether the material is hardening or weakening [Drucker, 1950; Palmer et al., 1967]. As will be shown below, our material does both.

Because of the alignment of principal axes of stress and strain rate, the plastic work $\sigma_{ij}\dot{\epsilon}_{ij}^P$ can be written as $\sigma_I\dot{\epsilon}_I^P + \sigma_{II}\dot{\epsilon}_{II}^P$. The central hypothesis made here and by Parmerter and Coon [1973] is that this work can be equated to the known sinks of energy in the ridging process; that is,

$$\sigma_I\dot{\epsilon}_I^P + \sigma_{II}\dot{\epsilon}_{II}^P = \left(\begin{array}{c} \text{Rate of potential} \\ \text{energy production} \\ \text{per unit area} \end{array} \right) + \left(\begin{array}{c} \text{Rate of frictional} \\ \text{energy loss} \\ \text{per unit area} \end{array} \right) \quad (5)$$

In what follows, we evaluate these two energy sinks in terms of the thickness distribution. Then, from a more explicit form of equation 5, we can define p^* and examine how it changes as the ice deforms.

THE THICKNESS DISTRIBUTION

Suppose the fraction of an area covered by ice of thickness between h and $h + dh$ is $g(h)dh$. Then, the thickness distribution $g(h, \underline{x}, t)$ must satisfy the balance equation

$$\frac{Dg}{Dt} = -g \operatorname{div} \underline{v} - \frac{\partial}{\partial h} (fg) + \psi \quad (6)$$

where D/Dt is the material derivative; and div , \underline{v} , and \underline{x} are the divergence, velocity, and position in the two horizontal dimensions [Thorndike and Maykut, 1973; Coon et al., 1974; Rothrock, 1974]. The quantity $f(h, \underline{x}, t)$ is the rate of accretion (dh/dt) by thermodynamic processes and is considered to be a given external parameter. The redistribution function, $\psi(h, \underline{x}, t)$ represents changes in open water and transformations from ice of one thickness to ice of another by ridging. When a finite fraction of area $g(h)dh$ is covered by ice of a single thickness h_1 (dh is zero), $g(h)$ is a delta function of the appropriate magnitude at $h = h_1$. Equation 6 is a balance equation for the area of ice in each thickness band ($h, h + dh$).

The redistribution function as written by Rothrock [1974]

$$\psi = |\dot{\epsilon}^P| \{ \alpha_o(\theta) \delta(h) + \alpha_r(\theta) w_r(h; g) \} \quad (7)$$

is linear in the strain rate. The delta function represents a source of open water (ice of zero thickness) that is produced by the separation of floes and the exposure of the sea surface to the atmosphere. The ridging mode w_r represents the conversion of thin ice into thicker ice by ridging and so is typically negative for some small values of h and positive for larger values of h (Fig. 2). Specifically, it has the form

$$w_r(h) = \frac{-a(h) + n(h)}{1 - N(\infty)} \quad (8)$$

where $a(h)$ is the distribution of thin ice lost during ridging, $n(h)$ is the distribution of thick (ridged) ice produced, and $N(\infty)$ denotes $\int_0^\infty n(h)dh$. The dependence of $a(h)$ and $n(h)$ on $g(h)$ will be made explicit below when some examples are given. The opening coefficient α_o specifies how much

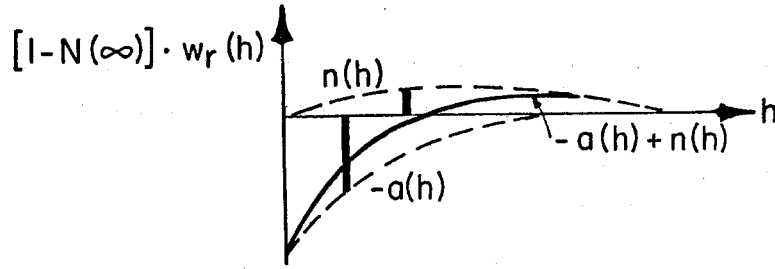


Fig. 2. The ridging mode $w_r(h)$. It is the difference between the area of thick ice being created, $n(h)$, and the area being annihilated, $a(h)$. In a particular ridge, the thin ice represented by the column on the left is converted into a smaller area of thicker ice (volume being conserved) represented by the second column.

opening is occurring; it should equal unity in pure divergence ($\theta = 0$) and zero in pure convergence ($\theta = \pi$). Similarly, the ridging coefficient α_r determines the amount of ridging; α_r equals zero when θ is zero and unity when θ is π . Because w_r is normalized ($\int_0^\infty w_r dh = -1$), the conservation of total area ($\int_0^\infty g(h) dh = 1$) provides that

$$\alpha_o(\theta) - \alpha_r(\theta) = \cos\theta. \quad (9)$$

Thus, given w_r , ψ is determined to within one function, say, $\alpha_r(\theta)$. Because of the material isotropy, both α_r and α_o are even functions of θ , and need be defined only in the range $[0, \pi]$.

The thickness distribution equation 6 can thus be written as

$$\frac{Dg}{Dt} = -g \operatorname{div} \underline{v} - \frac{\partial}{\partial h} (fg) + |\dot{\underline{\epsilon}}^p| \alpha_o \delta(h) - |\dot{\underline{\epsilon}}^p| \alpha_r \frac{a(h)}{1-N(\infty)} + |\dot{\underline{\epsilon}}^p| \alpha_r \frac{n(h)}{1-N(\infty)} \quad (10)$$

where the last term accounts for the production of ridged ice, the preceding term accounts for the loss by ridging of thin ice, and the term in α_o accounts for open water production.

POTENTIAL ENERGY

To quantify the production of gravitational potential energy by the ridging process, we begin by defining the potential energy relative to the sea surface. Suppose a floating block of ice has a draft h' and a free-board h'' , giving a total thickness $h = h' + h''$. If z is the vertical coordinate measured as positive upward from the sea surface, the potential energy of the ice per unit area is defined as

$$P_{ice} = \int_{-h'}^{h''} \rho_{ice} \hat{g} z dz = \frac{1}{2} \rho_{ice} \hat{g} (h''^2 - h'^2) \quad (11)$$

where \hat{g} is the acceleration of gravity, and the density of ice ρ_{ice} is assumed constant. The potential energy P_w of the displaced water per unit area is equal to the potential energy of the water in its displaced state (zero) less the potential energy of its undisplaced state; thus, we have

$$P_w = - \int_{-h'}^0 \rho_w \hat{g} z dz = + \frac{1}{2} \rho_w \hat{g} h'^2 \quad (12)$$

where the density of displaced water ρ_w is assumed constant. The potential energy of the ice-water system per unit area is equal to the sum of the energy of the ice and the energy required to displace the water

$$P = P_{ice} + P_w = \frac{1}{2} \rho_{ice} \hat{g} h''^2 + \frac{1}{2} \Delta \rho \hat{g} h'^2 \quad (13)$$

where $\Delta \rho = \rho_w - \rho_{ice}$.

P can be written as the sum of an isostatic term and a term involving the departure from isostasy

$$\frac{1}{2} \hat{\rho} \hat{g} h^2 + \frac{1}{2} \rho_w \hat{g} (h' - h \frac{\rho_{ice}}{\rho_w})^2 \quad (14)$$

where $\hat{\rho}$ is $\rho_{ice} \Delta \rho / \rho_w$, and $h \rho_{ice} / \rho_w$ is the value h' would have if the ice were locally isostatic. The departure from isostasy can be retained only with more information about the ice than is contained in the thickness

distribution, and we will neglect this term in what follows. However, the ratio of the nonisostatic energy to the isostatic energy

$$\frac{\rho_{\text{ice}}}{\Delta\rho} \left(\frac{h' - h\rho_{\text{ice}}/\rho_w}{h\rho_{\text{ice}}/\rho_w} \right)^2 \quad (15)$$

is not necessarily small, because of the small factor $\Delta\rho$ in the denominator. We can take ρ_w to be $1.0 \times 10^3 \text{ kg m}^{-3}$, ρ_{ice} to be $0.9 \times 10^3 \text{ kg m}^{-3}$, and therefore $\Delta\rho$ is $0.1 \times 10^3 \text{ kg m}^{-3}$. If the ice were 20% out of isostatic balance, for example--that is, if the quantity in parentheses in (15) were 0.2--this ratio (15) would be about 0.4.

We will digress briefly to examine the partition of potential energy, and to see that the building of a ridge requires energy not so much to pile up ice as to displace water as it "piles down" ice. In the isostatic case, h' and h'' are equal to $h\rho_{\text{ice}}/\rho_w$ and $h\Delta\rho/\rho_w$. Then, P_{ice}/P is equal to $(-\rho_{\text{ice}} + \Delta\rho)/\Delta\rho$, and P_w/P equals $\rho_{\text{ice}}/\Delta\rho$. For every unit of potential energy P of the floating ice system, the ice itself has a potential energy P_{ice} of -8 units, its center of mass being well below the water surface, and the displaced water has a potential energy P_w of +9 units. In another view, the first term on the right-hand side of equation 13 is identified as the energy P'' stored in the ice above the water surface, and the second term as the energy P' required to submerge the remainder of the ice. P''/P and P'/P are equal to $\Delta\rho/\rho_w$ (about 0.1) and ρ_{ice}/ρ_w (about 0.9). Thus, the potential energy of the above-water portion of the ice is fairly small: most of the potential energy is produced by forcing down the underwater portion of the ice. This energy of the underwater ice is still given by the difference of two large terms: the energy required to displace the water and the energy obtained by lowering the ice into its submerged position.

A macroscale area of sea ice, with its many ice thicknesses, has an isostatic potential energy per unit area of

$$P = c_p \int_0^\infty h^2 g(h) dh, \quad (16)$$

where $c_p \equiv \frac{1}{2} \hat{\rho} \hat{g}$. If $\hat{\rho}$ and \hat{g} are not functions of space \underline{x} or time t , the

balance equation for P is

$$\frac{DP}{Dt} = -P \operatorname{div} \mathbf{v} - c_p \int_0^\infty h^2 \frac{\partial}{\partial h} (fg) dh + c_p \int_0^\infty h^2 \psi dh \quad (17)$$

Each term on the right-hand side represents a particular effect. The first term measures the concentration or dilution of P by divergence. The second term describes the rate of change of potential energy caused by melting or freezing of ice--a purely thermodynamic source. The last term represents changes of the potential energy by mechanical processes that pile thin ice into thick ice, and is therefore the more explicit form we sought for the first term on the right-hand side of equation 5. By substituting expression 7 for ψ , we can write this term in the form

$$|\dot{\xi}^P| \propto_r p_p^* \quad (18)$$

where p_p^* is defined as

$$p_p^* = c_p \int_0^\infty h^2 w_r(h) dh \quad (19)$$

and gives that part of the total compressive strength p^* contributed by potential energy formation. Now we will derive the expression for the last term in (5) before assembling that equation and examining its consequences.

FRICIONAL LOSSES

The rate of frictional energy loss per unit area--the last term in (5)--can be written as

$$\int_0^\infty \left(\begin{array}{c} \text{Frictional energy loss} \\ \text{in ridging} \\ \text{per unit area lost} \end{array} \right) \times \left(\begin{array}{c} \text{Rate of area lost} \\ \text{per unit area} \\ \text{per unit ice thickness} \end{array} \right) dh \quad (20)$$

The second factor in (20) is simply the next-to-last term in equation 10.

There is no clearcut way to evaluate the frictional energy loss in ridging

per unit area lost (the first factor in equation 20). We will use the assumption used by Parmeter and Coon [1973] that, as shown in Figure 3, the ice sheet of thickness h_1 on the left is pushed into the rubble pile and emerges on the right as ice of thickness h_2 . The friction is assumed to be due to the sliding of the piles along the ice sheet for the full length of the triangular piles. This is somewhat self-contradictory, since the thin ice sheet is being broken and piled up while it is within these piles. But we do not know how to estimate the losses from blocks rubbing on other blocks within the pile, and the argument is that this idealized picture should provide a reasonable estimate of the frictional losses.

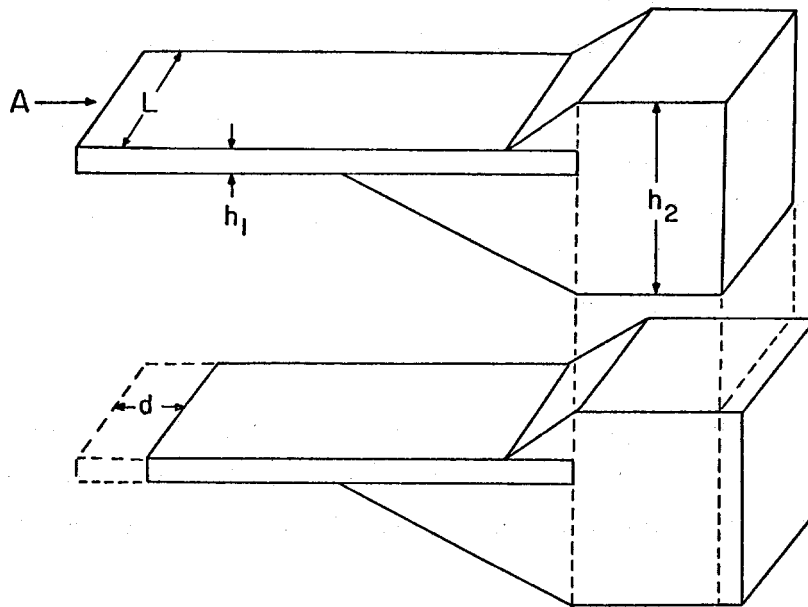


Fig. 3. A view from the side and somewhat above an idealized pressure ridge. The triangular piles and the thick ice (h_2) are composed of blocks broken from the sheet of thin ice (h_1) as it is pushed into the ridge by force A .

The frictional energy loss per unit area loss is simply the frictional force per unit length of ridge. This can be seen from Figure 3: the area of thin ice lost is $L \cdot d$, and the work done is $A \cdot d$, so the work per unit area lost is $Ad/(Ld)$, or A/L . Assuming Coulomb friction, this force per unit length is given by a coefficient of friction μ times the normal force per unit length between each pile and the sheet. This normal force is simply

the product of the weight density times the cross-sectional area of the pile. As before, we use a superscript " to refer to quantities above the sea surface, and a ' to refer to those below the sea surface. All geometrical quantities are defined in Figure 4. The frictional force per unit length is

$$\begin{aligned} & \mu'' \rho_{\text{ice}} \hat{g} \cdot \frac{(H'')^2}{2 \tan \phi''} + \mu' \Delta \rho \hat{g} \cdot \frac{(H')^2}{2 \tan \phi'} \\ & = \mu' \Delta \rho \hat{g} \frac{(H')^2}{2 \tan \phi'} \left\{ 1 + \frac{\mu'' \rho_{\text{ice}} \tan \phi' (H'')^2}{\mu' \Delta \rho \tan \phi'' (H')^2} \right\} \end{aligned} \quad (21)$$

If the coefficients μ'' and μ' are about equal, the second term in the bracket is only about 0.1 and can be neglected; this is because H''/H' is approximately equal to $\Delta \rho / \rho_{\text{ice}}$ by hydrostatics. We do not, however, know what values of μ' and μ'' are correct. Zubov [1943] gives coefficients of friction between ice and steel that vary from 0.03 to 0.50 (kinetic friction between dry sea ice and steel). Values for wet ice on both painted and unpainted steel lie between 0.10 and 0.40.

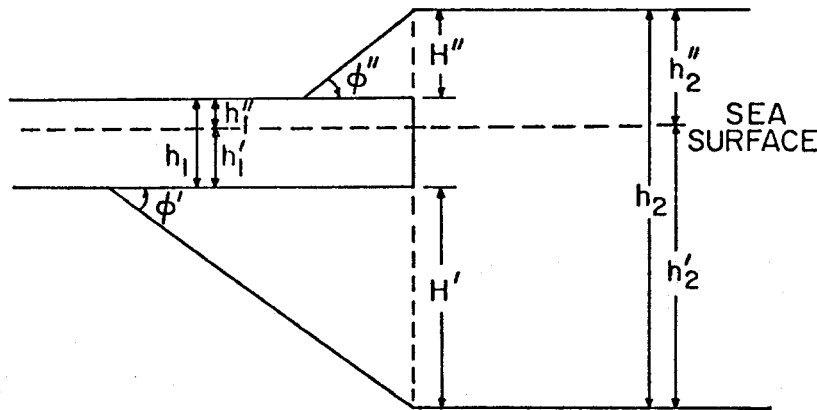


Fig. 4. Another cross section of a pressure ridge.

Those experiments involved contact between two flat surfaces. In the rubble pile of a ridge, the friction is more probably due to corners and edges of blocks digging into surfaces. In these circumstances, we can at

present only guess at the appropriate coefficient of friction. We cannot say whether μ' or μ'' is the larger: we might argue that since the under-ice pile is lubricated, μ' is less than μ'' ; or we might argue that since the bottom of the ice sheet is near the freezing point and therefore softer, the scouring effect would be greater there, making μ' greater than μ'' . Here, we will assume $\mu' = \mu'' \approx 0.1$ to 0.4 , and approximate the bracket in (21) by unity.

We want now to eliminate H' from (21) in favor of h_1 and h_2 . From Figure 1 we see that $H' = h_2' - h_1'$. Assuming the isostatic relation (which is only approximately satisfied)

$$\frac{h}{\rho_w} = \frac{h'}{\rho_{ice}}, \quad \text{for } h = h_1, h_2 \quad (22)$$

and the ridging law $h_2 = kh_1$, we have

$$H' = \frac{\rho_{ice}}{\rho_w} (k - 1)h_1 \quad (23)$$

The number k could be a function of h_1 , but we will assume it to be a constant. Combining (21) and (23), the force per unit length can be written as

$$c_f h_1^2 \quad (24)$$

where

$$c_f \equiv \frac{\mu' \Delta \rho g}{2 \tan \phi} \left(\frac{\rho_{ice} (k - 1)}{\rho_w} \right)^2 \quad (25)$$

The quantities h_1 in (24) and h in $a(h)$ are the same: the thickness of ice being ridged. The rate of frictional energy loss in ridging per unit area then takes the form

$$|\dot{\xi}^p| \propto_r p_f^* \quad (26)$$

where p_f^* is defined as

$$p_f^* = c_f \int_0^\infty \frac{h^2 a(h)}{1 - N(\infty)} dh \quad (27)$$

and represents that part of the compressive strength p^* caused by frictional losses in ridging.

THE ENERGY EQUATION

The energy equation (5) can now be written as

$$(\sigma_I \dot{\epsilon}_I^p + \sigma_{II} \dot{\epsilon}_{II}^p) \Big|_{F=0} = |\dot{\epsilon}^p| \alpha_r(\theta) p^* \quad (28)$$

where the right-hand side contains both the rate of potential energy production and the frictional energy loss combined in the factor p^* which we define as $p_p^* + p_f^*$.

We can immediately establish the points where the yield curve intersects the σ_I -axis. The curve is symmetric about the σ_I -axis since it is an even function of σ_{II} . At $\sigma_{II} = 0$, θ must take the values zero and π . Equation 28 and the conditions $\alpha_r(0) = 0$ and $\alpha_r(\pi) = 1$ show that $\sigma_I(\theta=0)$ takes the value zero and $\sigma_I(\theta=\pi)$ takes the value $-p^*$.

The yield function satisfying equation 28 is of the form $F(\sigma_I/p^*, \sigma_{II}/p^*)$; hence, the shape of the yield curve is determined by $\alpha_r(\theta)$ and is independent of p^* . This relation is best seen by defining nondimensional stresses $\chi = \sigma_I/p^*$ and $\eta = \sigma_{II}/p^*$ and regarding the yield criterion $F(\chi, \eta) = 0$ as the curve $\eta = \eta(\chi)$. The angle θ (between the χ -axis and the curve's normal) is given by $\tan\theta = -(d\eta/d\chi)^{-1}$. Equation 28 can then be rewritten as

$$\eta = -(\tan\theta)^{-1}\chi + \frac{\alpha_r(\theta)}{\sin\theta} \quad (29)$$

which is algebraic in the ridging coefficient α_r and differential in the yield function F since θ is known in terms of the gradient of F . This is Clairaut's equation; it has a straight line solution for each value of θ with slope $(-\tan\theta)^{-1}$ and η -intercept $\alpha_r/\sin\theta$. This equation also has

a singular solution consisting of the envelope of these straight lines, and it is this solution which we require for a yield curve (see Figure 5). Thus, there is a direct correlation between $\alpha_r(\theta)$ and the singular solution ($\eta = \eta(X)$ or $F = 0$). If $\alpha_r(\theta)$, and therefore a family of straight lines, is given, there exists a unique envelope. On the other hand, if the yield curve is given, it has only one set of tangent lines which determine $\alpha_r(\theta)$.

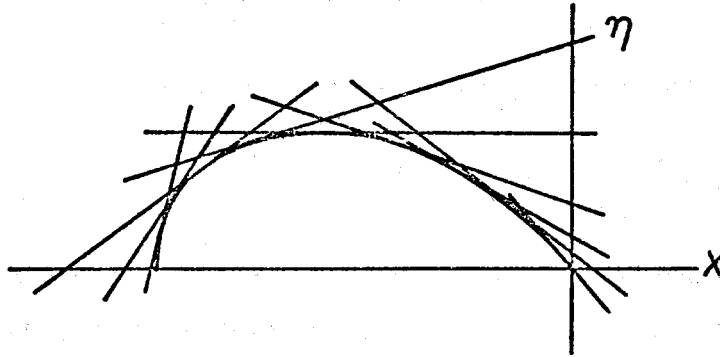


Fig. 5. The set of tangents specified by equation 29. Their envelope is the yield curve.

The restrictions that the yield function depends on only one parameter p^* and that this parameter does not affect the shape of the yield curve are not general restrictions; they are consequences of the assumed form of the redistribution function and of the assumed energy relation.

Neither the shape of the yield curve nor $\alpha_r(\theta)$ can be said to be known. Our procedure is to deduce what we can about the yield curve from our physical picture of pack ice and then to calculate α_r . We have asserted that the yield curve is symmetrical about the σ_I -axis and passes through the points $(0,0)$ and $(-p^*,0)$. Randomly oriented cracks should preclude tension in any direction, and so the yield curve should be confined to the quadrant in Figure 1 in which the principal stresses σ_1 and σ_2 are negative. Within these general constraints, any yield curve is physically acceptable. A general property of yield curves of this type is that shear stress can only be applied if pressure is applied simultaneously---a property well documented in some granular materials. A suitable yield curve is given by

$$\frac{\sigma_{II}}{p^*} = -\frac{\sigma_I}{p^*} \left(1 + \frac{\sigma_I}{p^*}\right)^{\frac{1}{2}} \quad (30)$$

which is illustrated in Figure 6 along with its $\alpha_r(\theta)$. Other possible shapes and α_r 's are given by Rothrock [1974].

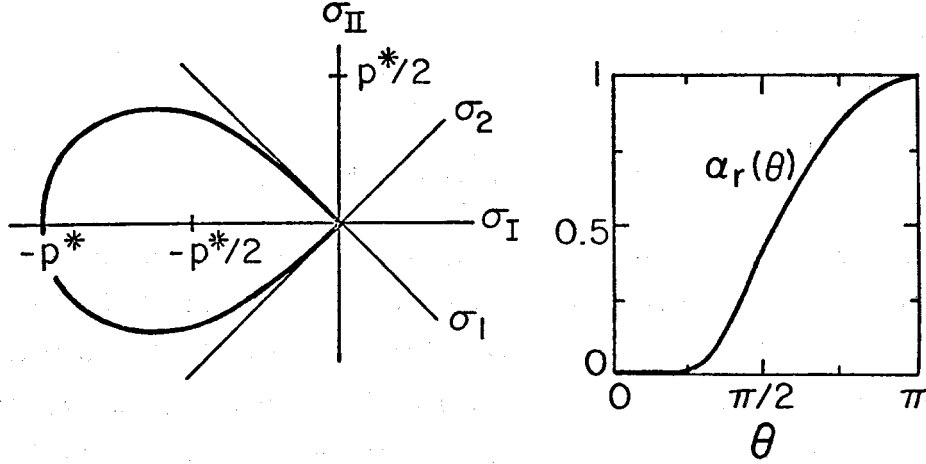


Fig. 6. The yield curve satisfying equation 30 and its associated $\alpha_r(\theta)$.

Several general relations can be stated between the shape of the yield curve and the properties of $\alpha_r(\theta)$. It helps to associate with each point on the yield curve a value of θ (many values at corners) and thus a value of α_r . Three of these relations are (1) that α_r is zero at the origin of the (σ_I, σ_{II}) plane and on straight-line segments of the yield curve through the origin, (2) that $\alpha_r(\theta)$ is a continuous, single-valued function for any closed, convex yield curve, and (3) that discontinuities in $d\alpha_r/d\theta$ correspond to straight-line segments of the yield curve [Rothrock, 1974]. A necessary condition on $\alpha_r(\theta)$ for the yield curve to be convex is

$$\frac{d^2\alpha_r}{d\theta^2} + \alpha_r \geq 0. \quad (31)$$

This can be shown by denoting $d\eta/d\chi$ by p (which equals $-\cot\theta$), and differentiating (29) with respect to χ to obtain

$$\chi = \frac{d}{dp} \left(\frac{\alpha_r}{\sin\theta} \right) = \sin^2\theta \frac{d}{d\theta} \left(\frac{\alpha_r}{\sin\theta} \right) \quad (32)$$

Convexity implies $d^2\eta/d\chi^2 = dp/d\chi \leq 0$, or $d\chi/dp \leq 0$. But $d\chi/dp$ is simply

$$\frac{d\chi}{dp} = \frac{d\theta}{dp} \cdot \frac{d\chi}{d\theta} = -\sin^3\theta \left(\frac{d^2\alpha_r}{d\theta^2} + \alpha_r \right) \quad (33)$$

Inequality (31) follows.

THE COMPRESSIVE STRENGTH p^*

There are several points to be made about p^* . What is the relative size of p_p^* and p_f^* ? How large is p^* and how is it calculated? How does it vary and cause hardening or weakening of the material? In all that follows, we assume a linear ridging law ($k = \text{constant}$). Then, $n(h)$ is equal to $a(h/k)/k^2$, $N(\infty)$ equals $1/k$ (since, by definition [Rothrock, 1974], $\int_0^\infty a(h)dh = 1$), and $\int_0^\infty h^2 n(h)dh$ is equal to $k \int_0^\infty h^2 a(h)dh$. Hence, p^* is

$$p^* = p_p^* + p_f^* = k c_p \left(1 + \frac{p_f^*}{p_p^*} \right) \int_0^\infty h^2 a(h)dh \quad (34)$$

The ratio p_f^*/p_p^* is simply $c_f/[c_p(k-1)]$ or

$$\frac{\mu'}{\tan\phi'} \cdot \frac{\rho_{ice}}{\rho_w} \cdot (k-1) \quad (35)$$

Taking $\mu' = 0.1$, $\tan\phi' = 0.8$, and $k = 5$, we find p_f^*/p_p^* is about 0.45. Increasing μ' to 0.4 gives a ratio of 1.8. Thus, the potential energy production and frictional work are about the same magnitude.

To calculate p^* , we need to know how $a(h)$ depends on $g(h)$. Following Rothrock [1974], we assume

$$a(h) = b(G(h)) \cdot g(h) \quad (36)$$

where $G(h) = \int_0^h g(\xi)d\xi$ is the cumulative thickness distribution ($0 \leq G \leq 1$).

For simplicity, we will take

$$b(G) = \begin{cases} \frac{1}{G^*}, & 0 \leq G \leq G^* \\ 0, & G^* \leq G \leq 1 \end{cases} \quad (37)$$

(The value $1/G^*$ ensures that $\int_0^\infty a(h)dh = 1$.) Thus, equation 36 states that $a(h)$, the amount of ice of each thickness being ridged, is given by the amount of ice present (g), weighted by a factor b which is zero for $G > G^*$. This means that only the thinnest G^* th fraction of the ice cover is subject to ridging. (A reasonable value of G^* is 0.15.) As an example, suppose the ice thinner than h^* ($\equiv G^{-1}(G^*)$) is uniformly distributed so that

$$g = \frac{G^*}{h^*} \quad \text{and} \quad G = \frac{G^*}{h^*} h \quad (38)$$

in $[0, h^*]$. Then $\int_0^\infty h^2 a(h)dh$ is found to be $(h^*)^2/3$. For $\hat{g} = 10 \text{ m sec}^{-2}$ c_p is $0.45 \times 10^3 \text{ kg m}^{-2} \text{ sec}^{-2}$. Using the smaller coefficient of friction (0.1) and a typical h^* of 1 m, we find p^* to have a value of $1.08 \times 10^3 \text{ N m}^{-1}$.

Since p^* depends on $a(h)$, which in turn depends on $g(h)$, the strength of the material will change as $g(h)$ changes. Equation 6 states that both deformation and thermodynamics can cause $g(h)$ to change. Melting and divergence weaken the ice; freezing and convergence strengthen it. Examples of the response of a single element of pack ice driven by a 40-day sequence of observed strain rates are discussed in Coon et al. [1974] and Coon and Pritchard [in press], where it is shown that, within periods of several days under winter thermodynamics, the ice cover will alternately weaken and harden as the ice diverges and converges.

What is significant about the formalism presented here is that it predicts a compressive strength p^* very much smaller than might be estimated by other means. For example, if the deformation of pack ice required that the ice itself be crushed, the necessary load p_{cr}^* would be $\sigma_{cr} h$, where the crushing strength of sea ice σ_{cr} is about $4 \times 10^5 \text{ N m}^{-2}$ [Coon, 1972]. Or, if we treat the ice as a semi-infinite beam on an elastic foundation [Parmerter, 1974], we find it will buckle at a load p_b^* of

$$\left(\frac{E \rho_w \hat{g}}{12(1 - \nu^2)} \right)^{1/2} h^{3/2} \quad (39)$$

where Young's modulus E is about $3 \times 10^8 \text{ N m}^{-2}$ and Poisson's ratio ν is about 0.3. Table 1 shows how small p^* is compared to p_{cr}^* and p_{b}^* . The omnipresence of pressure ridges in the ice cover is due precisely to the smallness of p^* ; the mechanism of ridging occurs at the lowest levels of stress.

TABLE 1

VARIOUS COMPRESSIVE STRENGTHS IN UNITS OF 10^3 N m^{-1}
FOR THREE THICKNESSES, IN UNITS OF m

h or h^*	p_{cr}^*	p_{b}^*	p^*
0.1	40	17	0.01
0.5	200	185	0.27
1.0		524	1.08

The values of p^* given here are supported by another consideration. From the momentum equation [Coon et al., 1974], we know that a stress gradient of magnitude p^*/L , where L is the typical length scale (here about 10^6 m), must approximately balance the stress τ applied to the upper surface of the ice by the wind. A moderate value of τ is 0.1 N m^{-2} . If the dimensionless number $p^*/(\tau L)$ is small compared with unity, the flow should be plastic almost everywhere. If that number is large, plastic flow could only be forced in extension. The value $p^* \approx 10^3 \text{ N m}^{-1}$ gives a small value of $p^*/(\tau L)$ --about 10^{-2} ; hence, the flow should usually be plastic. And, indeed, ridging is observed all over the arctic ice cover, and ridging in this model is synonymous with plastic flow.

CONCLUSION

From a consideration of the energy dissipated in pressure ridge formation, we have proposed constitutive equations for the plastic deformation of pack ice. The theory is built partly on a mechanical picture of ridging developed by Parmeter and Coon [1973], partly on a set of assumptions within the redistribution function ψ about the dependence of ridging on strain rate and on thickness [Rothrock, 1974], and partly on some simple ideas from plasticity.

The limitations of the theory are not clear at present, but the numerous assumptions, all of which need further consideration, are evident. There are known mechanisms of floe interaction which have been excluded from consideration here: friction in shear between floes, the formation of shear ridges, and rafting (overriding) of floes. There are factors influencing the (pressure) ridging process which have been ignored or crudely approximated: nonisostatic potential energy, voids in newly formed ridges, and the coefficient of friction and, in fact, the whole phenomenon of friction in a rubble pile whose typical size is only several times that of the blocks which form it. The pack ice may, in reality, choose to obey other than the normal flow rule assumed here. The ice cover may have significant tensile stress at times when cracks heal sufficiently (by freezing). Isotropy may not be a justifiable approximation.

There are these and undoubtedly other assumptions which must be scrutinized. In the process, this theory may be found seriously deficient. But it has the advantage over all the ad hoc models listed in the introduction that its assumptions are explicit: the small-scale process thought to control the deformation of large-scale areas has been identified, idealized, and parameterized into a plastic constitutive equation.

ACKNOWLEDGMENT

I am grateful to Max Coon, Reid Parmeter, and Alan Thorndike for discussions which clarified the content and presentation of this paper. This work was supported under National Science Foundation grant OPP71-04031 to the Arctic Sea Ice Study at the University of Washington.

REFERENCES

- Campbell, W. J. 1965. The wind-driven circulation of ice and water in a polar ocean. *Journal of Geophysical Research*, 70, 3279-3301.
- Coon, M. D. 1972. Mechanical behavior of compacted arctic ice floes. *Preprints, Offshore Technology Conference, Houston, Texas, 1-3 May 1972*, Paper No. OTC 1684. American Institute of Mining, Metallurgical, and Petroleum Engineers.
- Coon, M. D., G. A. Maykut, R. S. Pritchard, D. A. Rothrock, and A. S. Thorndike. 1974. Modeling the pack ice as an elastic-plastic material. *AIDJEX Bulletin No. 24* (May 1974), pp. 1-105.
- Coon, M. D., and R. S. Pritchard. Application of an elastic-plastic model of arctic pack ice. *Proceedings of the Symposium on Beaufort Sea Coastal and Shelf Research, San Francisco, California, 7-9 January 1974*, Arctic Institute of North America, Washington, D.C. (in press).
- Doronin, Yu. P. 1970. On a method of calculating the compactness and drift of ice floes (K metodike rascheta splochnosti i dreifa l'dov). *Proceedings of the Arctic and Antarctic Research Institute (Trudy Arkt. i Antarkt. In-ta)*, vol. 291, pp. 5-17. [English transl., *AIDJEX Bulletin No. 3* (Nov. 1970), pp. 22-39.]
- Drucker, D. C. 1950. Some implications of work hardening and ideal plasticity. *Quarterly of Applied Mathematics*, 7, 411-418.
- Nikiforov, Ye. B., Z. M. Gudkovich, Yu. I. Yefimov, and M. A. Romanov. 1967. Principles of a method for computing ice redistribution under the influence of wind during the navigation period in arctic seas (Osnovy metodiki rascheta pereraspredeleniya l'da b arkticheskikh moryakh b navigatsionnyy period pod vozkeystviem vetra). *Proceedings of the Arctic and Antarctic Research Institute (Trudy Arkt. i Antarkt. In-ta)*, 275, pp. 5-25. [English transl., *AIDJEX Bulletin No. 3* (Nov. 1970), pp. 22-39.]
- Nye, J. F. 1973. The physical meaning of two-dimensional stresses in a floating ice cover. *AIDJEX Bulletin No. 21* (July 1973), 1-8.
- Palmer, A. C., G. Maier, and D. C. Drucker. 1967. Normality relations and convexity of yield surfaces for unstable materials or structural elements. *Journal of Applied Mechanics*, 34, Trans. ASME, 464-470.
- Parmerter, R. R. 1974. A mechanical model of rafting. *AIDJEX Bulletin No. 23* (January 1974), 97-115.
- Parmerter, R. R., and M. D. Coon. 1973. Mechanical models of ridging in the arctic sea ice cover. *AIDJEX Bulletin No. 19* (March 1973), 59-112.

Rothrock, D. A. 1973. The steady drift of an incompressible arctic ice cover. *AIDJEX Bulletin No. 21* (July 1973), 49-78.

Rothrock, D. A. 1974. Redistributions and their yield surfaces in a plastic theory of pack ice deformation. *AIDJEX Bulletin No. 23* (January 1974), 53-81.

Thorndike, A. S., and G. A. Maykut. 1973. On the thickness distribution of sea ice. *AIDJEX Bulletin No. 21* (July 1973), 31-47.

Zubov, N. N. 1943. *Arctic Ice* (Izdatel'stvo glavsevmorputi). Moscow. [English transl., U.S. Naval Oceanographic Office, NTIS no. AD 426 972.]

COMPARISON OF SHEAR STRESS CALCULATIONS BETWEEN TWO PROFILE METHODS USING SOME DRAG-PLATE MEASUREMENTS

by

Chi-Hai Ling
U.S. Geological Survey
Tacoma, Washington 98416

When one uses several velocity profiles to find a single value for the roughness parameter z_0 of a surface, the confidence interval narrows considerably and the values of the friction velocity seem more consistent with real measurements than when z_0 is allowed to vary for each profile [Ling and Untersteiner, 1974]. But how good is the boundary stress so calculated when compared with direct stress measurements as determined from a drag plate?

To answer this question, we took the drag-plate measurements made on the Great Plains of Kansas by a group from UCLA [Lettau and Davidson, 1957, pp. 400-552; for a description of the site, see pp. 377-383] and compared them with the friction velocity, u_* , determined by the profile methods with variable z_0 and with a single value of z_0 . Between 1 August and 8 September 1953, the UCLA group made 35 drag-plate measurements at the surface* and 94 velocity profiles at 0.5, 1, 2, 4.15, and 8 m. Of those profiles, 6 were judged to be nonlogarithmic and 2 deviated widely from the wind direction of the others; these 8 were discarded and the remaining 86 profiles were grouped by surface wind direction:

1. 128°-157° from north (8 profiles)
2. 159°-190° from north (59 profiles)
3. 191°-213° from north (19 profiles)

The 8 m data were then deleted from the profiles because they deviated from

*Johns Hopkins University also measured boundary stress with a drag plate during the same project, but the measurements from UCLA are considered to be more accurate [Vehrencamp, 1953].

the logarithmic profile. The roughness parameters (z_0) and the friction velocity (u_*) were then calculated by both the conventional and the Ling and Untersteiner method--which for brevity we refer to here as the L&U method. The results are compared below.

The logarithmic relationship

$$u = (u_*/k) [\ln (z - d)/z_0]$$

is used in both methods, regardless of whether the atmospheric condition is neutral or not. (The logarithmic nature of the profiles indicates a neutral lapse rate, however.) Here u is the velocity parallel to the surface, u_* the friction velocity, k the von Karman constant, z the distance from the surface, d the displacement height [Lettau, 1957], and z_0 the roughness parameter.

The value of d is set equal to zero. In the L&U method, z_0 is found for each wind direction group by minimizing the quantity

$$\sum_{j=1}^M \sum_{i=1}^N (A/B - C)^2$$

where

$$A = u_{ij} \sum_{i=1}^N [\ln (z_{ij}/z_0)]^2$$

$$B = \sum_{i=1}^N u_{ij} \ln (z_{ij}/z_0)$$

$$C = \ln (z_{ij}/z_0)$$

M = number of profiles in a group

N = number of measurements in a profile

The friction velocity is found by using

$$u_{*j} = F/G$$

where $F = k \sum_{i=1}^N u_{ij} \ln (z_{ij}/z_0)$

$$G = \sum_{i=1}^N [\ln (z_{ij}/z_0)]^2$$

The boundary shear stress is $\tau = \rho u_*^2$, where ρ is the density of air. For the three wind direction groups, z_0 is 2.59 cm for the first group, 1.02 cm for the second, and 1.54 cm for the third. One might say that the roughness parameter is not very sensitive to the wind direction in this case.

Since the value of k in the atmosphere has not been firmly established, a number of k values have been used to compare values of calculated shear stress from the profile methods with the drag-plate measurements. A plot of average deviation D_a versus k is shown in Figure 1; it is defined as follows:

$$D = \left| \frac{T_p - T_m}{T_m} \right|$$

$$D_a = \frac{1}{35} \sum_{i=1}^{35} \left| \frac{T_p(i) - T_m(i)}{T_m(i)} \right|$$

where T_p is the stress calculated from the profile method and T_m is the stress measured from the drag plate.

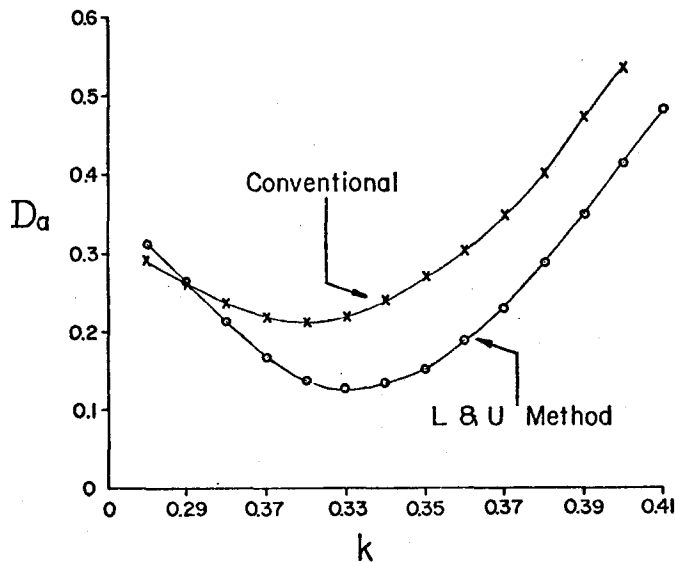


Fig. 1. Average deviation of boundary stress D_a versus von Karman constant k .

For the L&U method, a k value of 0.33 gives a best fit (or minimum average deviation) with $D_a = 12.8\%$, while for the conventional method the best fit value of k is 0.32 with $D_a = 21.2\%$. For $0.30 \leq k \leq 0.41$ the L&U method always gives a smaller D_a and therefore a better agreement with the drag-plate measurements. Businger et al. [1971] found k to be equal to 0.35. When this value is used, the corresponding D_a will be 15.2% for the L&U method and 27.0% for the conventional method. Figure 2 shows the percentile deviation. It confirms the fact that the L&U method of profile determination of u_* agrees better with the drag-plate measurements. Table 1 shows best fit values of boundary stress from calculation as well as values of measured stress. Of 35 cases, the L&U method agreed better in 24 cases, while the conventional method agreed better in 11 cases.

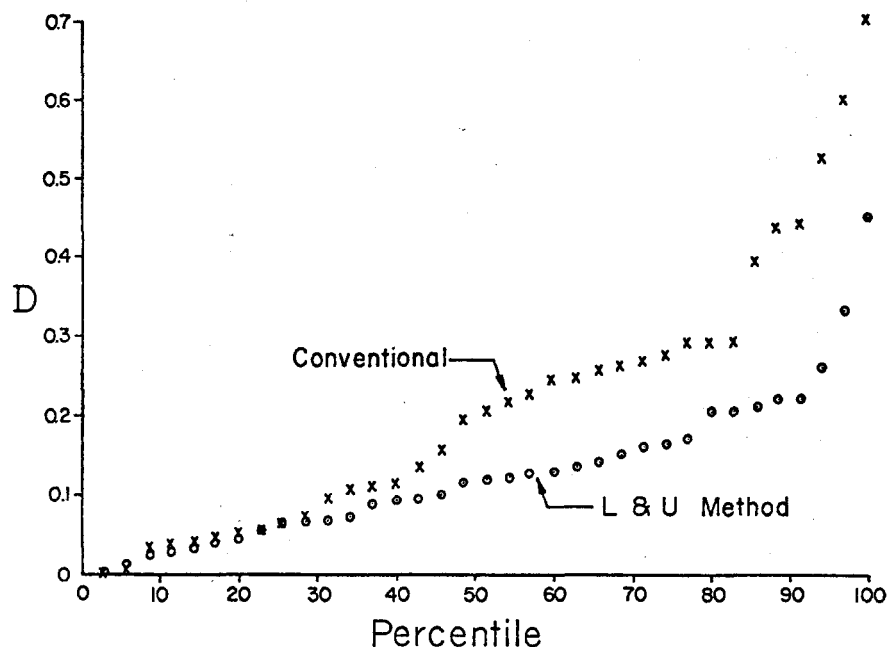


Fig. 2. Deviation in terms of percentile.

TABLE 1

COMPARISON OF BOUNDARY STRESS OBTAINED BY CONVENTIONAL METHOD
AND L&U METHOD (units in dyn/cm)

Case	Conventional with $k = 0.32$	Drag Plate	L&U Method with $k = 0.33$
1	0.4888	0.34	0.3492 v†
2	0.4541	0.38	0.4286 v
3	0.5737	0.40	0.3348 v
4	0.3371	0.43	0.3616 v
5	0.6315	0.49	0.5582 v
6	0.7824	0.49	0.5013 v
7	0.6172	0.49	0.3862 v
8	0.5803	0.65	0.6075 v
9	0.8084	0.66	0.6314 v
10	0.7381 v	0.69	0.7394
11	0.8068 v	0.71	0.8172
12	0.6307	0.71	0.7567 v
13	0.6917 v	0.73	0.5823
14	0.7341	0.97	0.9171 v
15	1.0619	0.97	1.0550 v
16	1.0646 v	1.03	1.1512
17	1.1250 v	1.13	1.0279
18	1.1022 v	1.14	1.0021
19	0.8275	1.16	0.9153 v
20	1.0901 v	1.22	1.4873
21	0.9431	1.25	1.2929 v
22	1.2020 v	1.26	1.3416
23	1.2915 v	1.28	1.1618
24	1.3442	1.30	1.3106 v
25	1.4701 v	1.38	1.6106
26	1.0970	1.51	1.3189 v
27	1.2816	1.52	1.5412 v
28	1.4707 v	1.55	1.3423
29	1.2555	1.58	1.4271 v
30	0.8298	1.74	0.9533 v
31	1.3215	1.80	1.7294 v
32	0.5764	1.91	1.4143 v
33	1.1879	1.95	1.3068 v
34	2.0298	2.72	3.0209 v
35	2.1057	2.95	2.3539 v

† (v) means better agreement with the drag-plate measurement.

ACKNOWLEDGMENT

The writer of this report is very grateful to Alan Thorndike and Drew Rothrock for their helpful comments. The computation of this work was supported by the Arctic Sea Ice Study under National Science Foundation grant OPP71-04031.

REFERENCES

- Businger, J., J. C. Wyngaard, Y. Izumi, and E. Bradley. 1971. Flux profile relationships in the atmospheric surface layer. *Journal of Atmospheric Science*, 28, 1021-1025.
- Lettau, H. H. 1957. Computation of Richardson numbers, classification of wind profiles, and determination of roughness parameters. *Exploring the Atmosphere's First Mile*, vol. 1. New York: Pergamon Press, pp. 328-336.
- Lettau, H. H., and B. Davidson. 1957. *Exploring the Atmosphere's First Mile*, vol. 2. New York: Pergamon Press, pp. 337-383, 400-552.
- Ling, C.-H., and N. Untersteiner. 1974. On the calculation of the roughness parameter of sea ice. *AIDJEX Bulletin No. 23* (January 1974), 117-125. (In press, *Journal of Geophysical Research*.)
- Vehrencamp, J. E. 1957. Measurements of boundary shear stress. *Exploring the Atmosphere's First Mile*, vol. 1. New York: Pergamon Press, pp. 99-103.

HYDROSTATIC LEVELING ON FLOATING ICE

by

J. R. Weber

Earth Physics Branch

Department of Energy, Mines and Resources

Ottawa, Canada

ABSTRACT

Hydrostatic levels installed on floating ice to measure ocean tilt are affected by vertical and horizontal accelerations of the ice platform, temperature changes of the level fluid, temperature and salinity changes of the well water, atmospheric pressure gradients, differential flow of the water below the wells, and the Coriolis force (ice velocity). Some errors resulting from these effects can be corrected or, if they are small enough, neglected. In order to achieve a tilt-measuring sensitivity of $\pm 1.6 \cdot 10^{-7}$ radians the drift velocity must be known to ± 1.1 cm/sec and the horizontal acceleration to $\pm 1.6 \cdot 10^{-4}$ cm/sec².

THE HYDROSTATIC LEVEL

Hydrostatic levels were used for measuring ocean tilt in 1969 near the North Pole [Weber and Lillestrand, 1971], in 1970 in the Gulf of St. Lawrence [Johannessen et al., 1970], and in 1972 during the AIDJEX pilot study in the Beaufort Sea [Weber, 1972]. The instrumentation has been improved considerably since then, and automated for use during the AIDJEX main experiment in 1975-76.

The principle of hydrostatic leveling is shown schematically in Figure 1. Two open reservoirs (pots A and B) are connected by a tube of length S , and the system is filled with a low-viscosity fluid. If the system is immobile and under equal atmospheric pressure at A and B and has a constant fluid density throughout, the fluid surfaces in the two pots form part of

the same equipotential surface that is independent of the tube configuration between A and B. Since mean sea level is an equipotential surface, the distance between it and the fluid surfaces in the pots (Δh_1 or Δh_2) is constant provided the pots are at sea level or very close to it. The hydrostatic level will therefore measure the tilt of the ocean relative to mean sea level or to the geoid. The tilt is $(\Delta h_1 - \Delta h_2)/S$ (see Fig. 1).

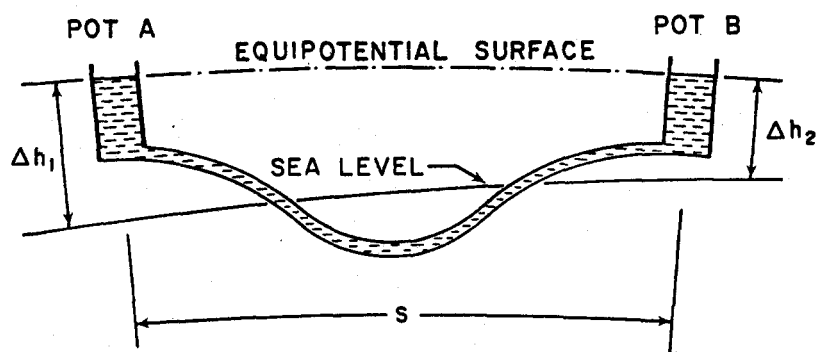


Fig. 1. Principle of measuring ocean tilt by hydrostatic leveling. The equipotential surface is parallel to the mean sea level.

An instrument installed on a drifting floe to measure ocean tilt is affected by a number of internal and external factors: vertical and horizontal accelerations, temperature changes in the fluid, temperature and salinity changes in the well water, atmospheric pressure gradients, differential flow, and the Coriolis force. Since the only reference levels are fluid surfaces, the system (1) is independent of the movement of the instrument support relative to the ice, (2) is independent of the vertical movement of the ice relative to the fluid ocean surface, (3) measures absolute tilt, and (4) lends itself readily to automatic recording. On the other hand, errors are introduced by temperature changes within the fluid, salinity changes in the ocean water, and atmospheric pressure gradients. These errors can, however, be minimized or corrected by proper system design.

The leveling system we used is shown in Figure 2. Two PVC pipes, each 3 m long, are frozen into the ice to form two wells whose water is heated

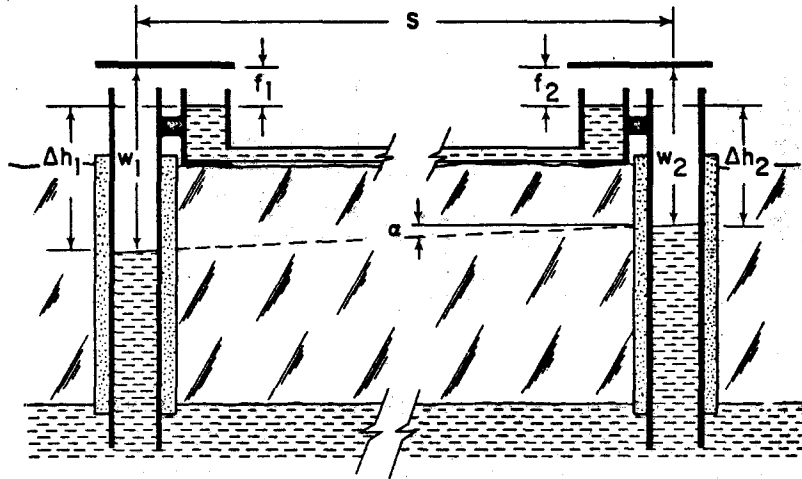


Fig. 2. Schematic diagram of the hydrostatic level used for measuring ocean tilt from a floe. The level differences between two level plates and the fluid surfaces f_1 , f_2 , w_1 , and w_2 are measured with meters from which the fluid level differences Δh_1 and Δh_2 are determined. The tilt is $(\Delta h_1 - \Delta h_2)/S$.

electrically to prevent freezing. Two pots are rigidly bolted to the pipes and connected by a horizontal Tygon tube, and the system is filled with a low-viscosity silicone fluid. In developing this system we attempted to keep the measurements of the level difference, $\Delta h_1 - \Delta h_2$, within a tolerance of ± 0.002 cm, resulting in a sensitivity of $\pm 1.6 \times 10^{-7}$ radians, with a level length of 120 m.

DYNAMIC RESPONSE

To understand the effects of accelerations on the hydrostatic level we must first study the dynamic response of the system.

The two pots of the hydrostatic level, shown in Figure 3, are of the same size. The cross-sectional areas of the pots and of the tube are A and α , and the length of the tube is S . At rest the length of the fluid column in the pots is h_0 . Assume that the fluid level is initially displaced by the length h_0 from the equilibrium level. It can be shown [Egedal, 1937; Scheel, 1956, Eaton, 1959; Eto, 1966] that the differential equation of motion is

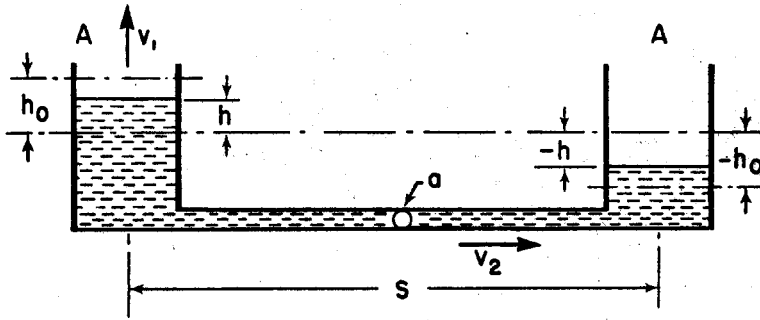


Fig. 3. Schematic diagram of hydrostatic level with cross-sectional areas of the pots, A , and of the tube, a . When displaced by the distance h_0 the fluid surfaces return to their equilibrium level. Fluid displacement takes place when an acceleration w acts upon the level; v_1 and v_2 are the fluid velocities in the pots and in the tube, respectively.

$$\ddot{h} + 2\delta\dot{h} + \omega^2 h = 0 \quad (1)$$

where h is the displacement of the fluid levels from the equilibrium level, $\delta = 4\pi\nu/a$, $\omega^2 = 2ga/SA$, ν is the kinematic viscosity of the fluid, and g is the gravitational acceleration. The equation has three solutions depending on whether ω^2 is greater than, equal to, or less than δ^2 .

(i) $\omega^2 > \delta^2$ (underdamped system):

$$h = h_0 \frac{1}{\sin \psi_1} e^{-\delta t} \sin(\mu_1 t + \psi_1) \quad (2)$$

$$\text{where } \mu_1 = \sqrt{\omega^2 - \delta^2}$$

$$\psi_1 = \arctan \mu_1 / \delta$$

(ii) $\omega^2 = \delta^2$ (critically damped system):

$$h = h_0 (1 + \delta t) e^{-\delta t} \quad (3)$$

(iii) $\omega^2 < \delta^2$ (overdamped system):

$$h = h_0 \frac{1}{\sinh \psi_2} e^{-\delta t} \sinh(\mu_2 t + \psi_2) \quad (4)$$

$$\text{where } \mu_2 = \sqrt{\delta^2 - \omega^2}$$

$$\psi_2 = \operatorname{arctanh} \frac{\mu_2}{\delta} = \frac{1}{2} \ln \frac{1 + \mu_2/\delta}{1 - \mu_2/\delta}$$

These three modes are illustrated in Figure 4, where the dynamic response has been calculated of a 120 m level of given pot dimensions, filled with a silicone fluid and operated at -20°C . The only variable is the tube diameter. The three modes of damping are: underdamped for 1" and 2" diameter, critically damped for 1/2" diameter, and overdamped for 1/4" diameter.

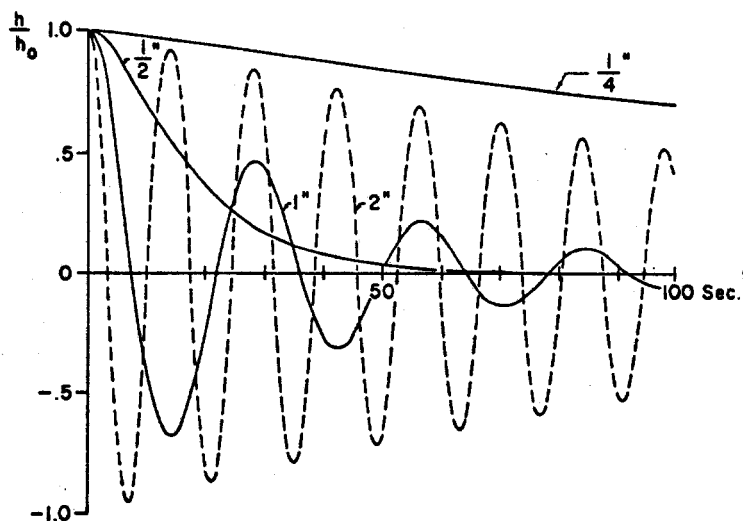


Fig. 4. Dynamic response of a hydrostatic level of 120 m length with pot diameters of 4.64 cm and filled with a fluid of 1.10 centistokes viscosity, calculated for four tube diameters. The system is overdamped for a 1/4-inch tube, critically damped for a 1/2-inch tube, and underdamped for 1-inch and 2-inch tubes.

The pack ice is set in motion by winds and water currents that cause wave motions (vertical accelerations associated with wave motions) and in ice drift (horizontal accelerations associated with wind); we have to study vertical and horizontal motion separately. The period of the ocean waves ranges from about 5 to 100 seconds with amplitudes of up to a few tens of millimeters and accelerations of a few milligals. If the hydrostatic leveling system is underdamped with a resonance frequency that lies within the frequency of the ocean waves, it will oscillate continuously. The ice drift is either divergent or convergent. If the drift is divergent,

horizontal accelerations will be more or less continuous; if the drift is convergent, internal ice pressure will build up until the ice breaks resulting in sudden horizontal accelerations. If the system is much overdamped, sudden horizontal accelerations or sudden atmospheric pressure changes (associated with wind gusts) will induce new disturbances before the old ones have died out and the system will never come to rest. We must therefore choose the design parameters so that the system is nearly critically damped.

DESIGN PARAMETERS

The sensitivity of the system is given by the ratio of the smallest fluid level differences Δh that can be measured and the level length S . The movement of the water level in the well limits Δh . Under perfectly calm conditions the level heights w_1 and w_2 (Fig. 2) can be measured to an accuracy of about $\pm 0.8 \times 10^{-3}$ cm. If we assume that each level height w_1 , w_2 , f_1 , f_2 can be measured to an accuracy of 1.0×10^{-3} cm, then the accuracy of the quantity $\Delta h = \Delta h_1 - \Delta h_2$ will be $\pm 2.0 \times 10^{-3}$ cm. The level length S is limited by economic considerations only. With $S = 120$ m, the sensitivity of the system will be $\pm 1.6 \times 10^{-7}$ radians.

We designed the system for an operating temperature of -20°C . Critical damping specifies that $\omega^2 = \delta^2$, or by substituting the system parameters with ω and δ (eq. 1),

$$\frac{2ga}{SA} = \frac{16\pi^2 v^2}{a^2} \quad (5)$$

By replacing the cross-sectional areas, a and A , of the pipes with their diameters, d and D , and by substituting the numerical value $g = 983 \text{ cm sec}^{-2}$, the following equation is obtained:

$$\frac{d^6}{D^2 S} = 0.1302 v^2 \quad (6)$$

It is desirable that (1) S be large, for increased sensitivity, (2) d be small, for economy and easier handling of the tubing in low temperature, and (3) D be large, to accommodate floats for automatic recording and to reduce the effect of capillarity and the sticking of the fluid column on the pot walls due to dirt. Therefore, a fluid must be chosen whose kinematic viscosity is small. In addition, the fluid should have the following properties: small coefficient of thermal expansion (to minimize temperature effects); a specific gravity that is either very high (insensitive to atmospheric pressure changes) or about 1 (effects of atmospheric pressure gradients will be compensated in the wells); low freezing temperature; and low solubility to air (to minimize the danger of formation of air locks). Two fluids were considered: mercury, and Dow Corning 210 fluid 0.65 centistokes, a low-viscosity silicone fluid. Table 1 lists specific gravity, viscosity, and coefficient of thermal expansion for the two fluids at -20°C and 0°C . Also listed for comparison are the corresponding properties of water at 20°C , since water has been used in hydrostatic leveling for geodetic purposes [Waalwijk, 1964]. Figure 5 shows the kinematic viscosity of mercury and Dow Corning 210 fluid as a function of temperature.

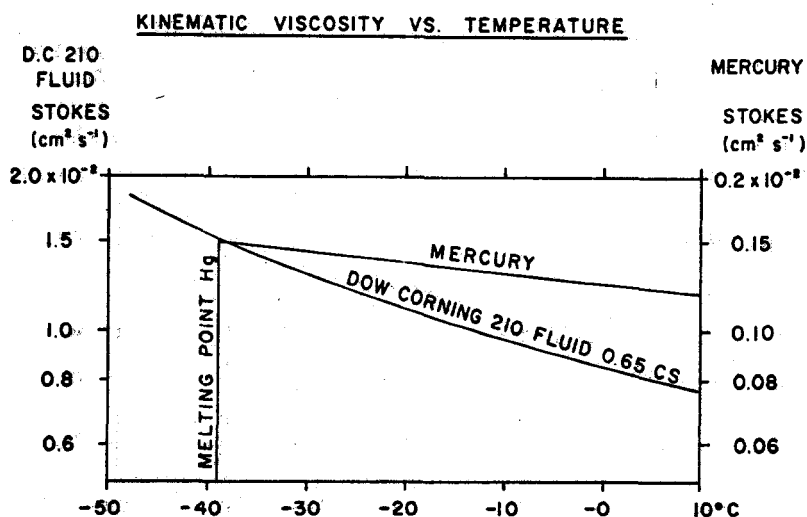


Fig. 5. Kinematic viscosity versus temperature curves for mercury and for Dow Corning 210 fluid 0.65 cs.

TABLE 1

PHYSICAL PROPERTIES (AT -20°C AND 0°C) OF TWO FLUIDS USED IN HYDROSTATIC LEVELS, COMPARED WITH THOSE OF WATER AT $+20^{\circ}\text{C}$

Property	Temp. $^{\circ}\text{C}$	Dow Corning 210 fluid	Mercury	Water
Specific gravity (g cm^{-3})	-20	0.810	13.645	
	0	0.789	13.595	
	+20			0.9982
Dynamic viscosity (Poise, $\text{cm}^{-1} \text{g sec}^{-1}$)	-20	0.89×10^{-2}	1.855×10^{-2}	
	0	0.67×10^{-2}	1.685×10^{-2}	
	+20			1.055×10^{-2}
Kinematic viscosity (Stokes, $\text{cm}^2 \text{sec}^{-1}$)	-20	1.10×10^{-2}	0.136×10^{-2}	
	0	0.85×10^{-2}	0.124×10^{-2}	
	+20			1.006×10^{-2}
Coefficient of thermal expansion ($^{\circ}\text{C}^{-1}$)	0	1.34×10^{-4}	1.814×10^{-4}	2.07×10^{-4}

Table 2 compares the physical properties of two 120 m levels, both of which at -20°C are critically damped and have a response time of about 90 sec. (The response time is the time it takes for an initial displacement $h = h_0$ to decay to $1/1000$ of its original value, according to eq. 3.) One has a tube diameter of 0.635 cm ($1/4''$) and a pot diameter of 2.0 cm and is filled with mercury; the other has tube and pot diameters of 1.27 cm ($1/2''$) and 4.64 cm, respectively, and is filled with silicone fluid. Table 2 also lists the period of resonance at 0°C when the systems are underdamped, the temperature differences between the pots and the temperature gradients in the pots corresponding to error displacements of 1×10^{-3} cm of the fluid levels and the displacement caused by atmospheric pressure gradients of 30 $\mu\text{bar/km}$. It can be seen that the mercury level is less sensitive to temperature and atmospheric pressure changes.

The decision to use silicone rather than mercury as the fluid was made mainly because the silicone level has a larger pot diameter and because mercury when exposed to air forms a surface scum that introduces additional complications. These two disadvantages seem to outweigh the benefits derived from the better physical characteristics of mercury as illustrated in Tables 1 and 2.

TABLE 2

COMPARISON OF TWO HYDROSTATIC LEVELS, ONE FILLED WITH MERCURY,
ONE WITH SILICONE FLUID

Length of tube: 120 m

Maximum allowable uncorrected displacement of fluid column

in pot: $\pm 2 \times 10^{-3}$ cm

Sensitivity: $\pm 1.6 \times 10^{-7}$ radians

Description	Mercury	Dow Corning 210 silicone fluid
Inside diameter of tube	0.476 cm	1.27 cm
Inside diameter of pot	2.0 cm	4.64 cm
Height of fluid column in pot	12.0 cm	12.0 cm
Freezing temperature of fluid	-39°C	< -60°C
Response time $h = 10^{-3} h_0$ at -20°C	96 sec	85 sec
Period of resonance at 0°C	155 sec	87 sec
Maximum allowable temperature difference between pots	$\pm 0.45^\circ\text{C}$	$\pm 0.06^\circ\text{C}$
Maximum allowable temperature gradient in pot	0.07°C/cm	0.01°C/cm
Displacement of fluid in pot column caused by atmospheric pressure gradient of 30 $\mu\text{bar/km}$	0.27×10^{-3} cm	4.5×10^{-3} cm

EFFECT OF EXTERNAL DISTURBANCES

The difference, or the change in difference, between the fluid surface of the hydrostatic level and the surface of the ocean water is measured either by touching the fluid surfaces with the pointed stainless steel rod of a depth micrometer or by sensing the displacement of floats electronically by means of displacement transducers. Level measurements with depth micrometers can be repeated to an accuracy of a few microns, and displacement transducers can measure displacements to a high accuracy with a resolution that is essentially infinite. Therefore, the sensitivity of the instrument is limited not by the accuracy with which level differences of the fluid can be sensed, but by the movement of the water surfaces in the wells and

by external disturbances such as temperature changes, atmospheric pressure changes, and ice movements. These external effects can be neglected if the resulting fluid level displacement does not exceed $\pm 1.0 \times 10^{-3}$ cm; they must be corrected if they are greater.

We shall now investigate these effects in detail. In particular, where the external disturbances are manifested by an error displacement of the fluid levels, we shall determine the maximum value of these disturbances before corrections have to be applied.

(i) Vertical accelerations

The period of ocean waves in pack ice ranges from 5 to 100 sec [Hunkins, 1962]. At temperatures above -20°C the system is underdamped and may resonate if the resonance frequency is in the 5-100 sec range. Indeed, when operating under summer conditions at 0°C when the tube is submerged in slush, the period of resonance is 87 sec (Table 2). In this case the tube length can be doubled, thus increasing the sensitivity by a factor of two.

(ii) Temperature changes in the fluid

Consider the hydrostatic level of Figure 6 (solid lines). If the fluid is stationary, then

$$p_1 + \rho_1 h_1 g = p_2 + \rho_2 h_2 g = \text{const.}$$

where p is the atmospheric pressure and ρ is the fluid density. If we assume that the density is temperature-dependent, $\rho = \rho(T)$, then the displacement of the fluid column in pot B, Δh , due to the temperature change, ΔT , is

$$\Delta h = h_2 - h_1 = \alpha h_2 \Delta T$$

where α is the coefficient of thermal expansion of the fluid.

The temperature difference between the two pots can be measured, but we do not know, nor do we have a way to measure, the average temperature difference of the fluid between descending and ascending tubes. It is therefore important to keep the tube as horizontal as possible. This requirement is illustrated in Figure 6 (broken line). If the tube is conducted over several obstacles such as ice bumps or pressure ridges, and if

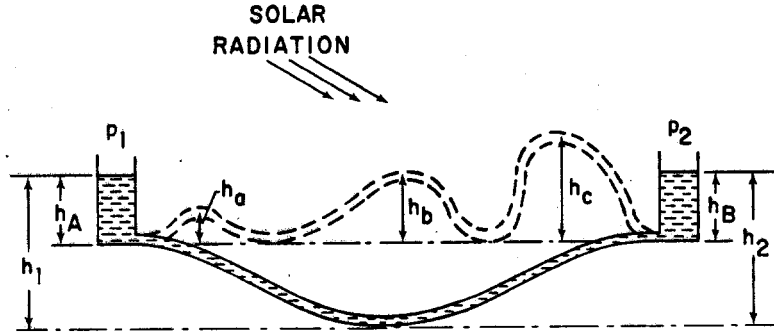


Fig. 6. The effect of undulation of the tube of hydrostatic level is cumulative. If solar radiation causes differential heating of the fluid of 0.1°C between the two sides of an obstacle, the sum of all the heights of the obstacles $h_a + h_b + h_c$ may not exceed 7.5 cm.

solar radiation causes more heat absorption on one side of the obstacles than on the other side, resulting in differential expansion of the fluid, then the total error introduced, Δh , will be cumulative:

$$\Delta h = \underbrace{\alpha \Delta T_{AB} (h_A - h_B)}_{\Delta h_{AB}} - \underbrace{\alpha (h_a \Delta T_a + h_b \Delta T_b + \dots)}_{\Delta h^*} \quad (7)$$

where h_a , h_b , etc., are the heights of the obstacles and ΔT_a , ΔT_b , etc., are the average temperature differences between the two sides of the obstacles. The first term, Δh_{AB} , represents the error introduced by the temperature difference ΔT_{AB} between the fluids in the two pots. To determine the value of Δh_{AB} to better than ± 0.01 mm the temperature difference of the fluid between the two pots must be either measured or controlled to better than $\pm 0.06^{\circ}\text{C}$. With thermistors the temperature can easily be measured or controlled with an accuracy of $\pm 0.01^{\circ}\text{C}$. But care must be taken that the pots are well insulated and have a large heat capacity relative to the fluid in order to avoid temperature gradients in the fluid greater than $\pm 0.01^{\circ}\text{C}/\text{cm}$.

The second term, Δh^* , represents the error introduced by differential heat absorption as the tube crosses the obstacles. Since the values of the ΔT 's are unknown, the value of Δh^* is unknown. Fortunately Δh^* can be minimized by minimizing the undulations of the tube, and Δh^* becomes zero

when the tube is perfectly horizontal. We may now ask: what is the maximum value of the sum of all the vertical displacements $h_S = h_a + h_b + \dots$ that can be tolerated for each degree of temperature difference ΔT in order that $\Delta h^* < 10^{-3}$ cm?

From the second term of equation 7 it follows that

$$\Delta h = -\alpha \Delta T (h_a + h_b + \dots) = -\alpha h_S \Delta T$$

This means that if the temperature difference ΔT between the ascending and the descending side of each bump is 0.1°C , the sum of the heights of all the bumps may not exceed 7.5 cm! It is therefore important to install the hydrostatic levels on a very flat floe of winter ice and to cover the tubes with snow to minimize any effects of differential heat absorption.

(iii) Temperature and salinity changes of the well water

Both temperature and salinity changes of the well water affect the length of the water column in the well. Fortunately, under winter conditions, two characteristics of the Arctic Ocean surface water are greatly in our favor. One is that its coefficient of thermal expansion is nearly zero, so that we can safely neglect effects of slight temperature changes. The other characteristic is that temperature and salinity are nearly constant in the top 50 m, changing less than $\pm 0.02^\circ\text{C}$ and ± 0.02 ‰.

(iv) Atmospheric pressure gradients

An atmospheric pressure gradient along the hydrostatic level acts on the surface of the hydrostatic fluid in the pots of the level and on the surface of the water in the wells. If the hydrostatic fluid and the water in the wells were of the same density, the displacement due to the pressure gradient would be the same in the pots and in the wells and the pressure gradient would not affect the tilt measurement. Because the densities of the two liquids are not exactly the same, an uncompensated net displacement remains:

$$\Delta h = \frac{\Delta p}{g} \left(\frac{1}{\rho_F} - \frac{1}{\rho_W} \right) \quad (8)$$

where Δp is the pressure difference between the two ends of the level, ρ_F is the density of the hydrostatic fluid, and ρ_W is the density of the well water.

In the high arctic latitudes during April no atmospheric pressure gradients in excess of 30 $\mu\text{bar}/\text{km}$ would be expected to persist for any length of time (George Gilbert, Defence Research Board, Ottawa, personal communications). For a 120 m level this corresponds to a maximum pressure difference $\Delta p = 3.6 \mu\text{bar}$. Substituting this value into equation 8 together with the density values $\rho_F = 0.79 \text{ g/cm}^3$ and $\rho_W = 1.024 \text{ g/cm}^3$ gives a maximum expected displacement Δh of 0.001 cm. This means that in our particular application atmospheric pressure gradients can be neglected.

(v) Differential flow

The water flowing at speed v past the bottom end of the wells (Fig. 2) reduces the water pressure and causes a decrease of the water column $h = v^2/2g$, according to Bernoulli's equation. A decrease of 0.001 cm in the water column will thus be caused by a current of 1.4 cm sec^{-1} , or 50 m per hour. This effect introduces a significant error whenever the differential flow of water between the ends of the hydrostatic level exceeds 50 m per hour. It is therefore important to avoid the effect of local turbulence by locating the end of the level at some distance from any pressure ridge.

(vi) Horizontal accelerations

Any tiltmeter, whether it be of the hydrostatic, spirit level, or pendulum type, is affected by horizontal accelerations. There are two modes of accelerations to be considered. The first is of short duration and occurs during convergent flow when mounting internal ice pressure causes the ice to break. As a result the fluid levels in the pots are displaced and the disturbance is manifested as a transient displacement of the fluid levels. It is important that these transients be short-lived so that they have disappeared before new transients are generated. The transients are shortest when the system is critically damped (Fig. 4). A measure of their duration is the response time, which we define as being the time it takes for an initial displacement $h = h_0$ to decay to $h = h_0 \times 10^{-3}$. Table 2 shows that the response time of our level is 85 sec.

The second mode concerns steady accelerations as experienced by wind-driven floes. Assume that the level is being exposed to a constant acceleration $w = dv_2/dt$ in the direction of its axis (Fig. 3). Since $v_1 A = v_2 a$,

where v_1 and v_2 are the velocities of the fluid in the pots and in the connecting tube, respectively, the corresponding acceleration of the fluid in the pots is $dv_1/dt = (a/A)w$. Hence, from equation 1 we obtain the differential equation of motion of the fluid levels:

$$\ddot{h} + 2\delta\dot{h} + \omega^2 h = \frac{a}{A} w \quad (9)$$

The solution for critical damping ($\delta^2 = \omega^2$) is

$$h(t) = \frac{aw}{A\omega^2} \left(1 - e^{-\omega t} (1 + \omega t) \right) \quad (10)$$

or, by substituting $\omega^2 = 2ga/SA$, and by expressing $h(t)/S$ by the apparent tilt, $\alpha(t)$,

$$\alpha(t) = \frac{w}{2g} \left(1 - e^{-\omega t} (1 + \omega t) \right) \quad (11)$$

From these equations it follows that a displacement of 0.001 cm in the fluid levels will be caused by a constant acceleration of $w = 1.55 \times 10^{-4}$ cm sec⁻², or 20 m hr⁻², and an acceleration of 290 m hr⁻² will cause an apparent tilt of 5×10^{-7} radians. During Project North Pole--1969, when the fine structure of the ice movement was studied by ranging from acoustic transponders on the ocean floor, accelerations of up to several hundred meters per hour were found to be common. Therefore, measuring ocean tilt to an accuracy of better than, say, 10^{-6} radians requires precise information on the ice movement.

(vii) The Coriolis force

As the hydrostatic level travels with the floe at velocity v , it is affected by the Coriolis force (Fig. 7). The vector of the Coriolis acceleration is $\vec{c} = 2(\vec{\omega} \times \vec{v})$, where $\vec{\omega}$ is the angular velocity of the earth's rotation. We need only consider the horizontal component of the Coriolis force. Its magnitude is $c = 2v\omega \sin\phi$, where ϕ is the geographical latitude. The Coriolis force, which is directed 90° to the right of the velocity vector, deflects the pot surfaces by the amounts $h_c/2$ and $-h_c/2$ relative to the equipotential surface. The tilt of the level due to the Coriolis force is

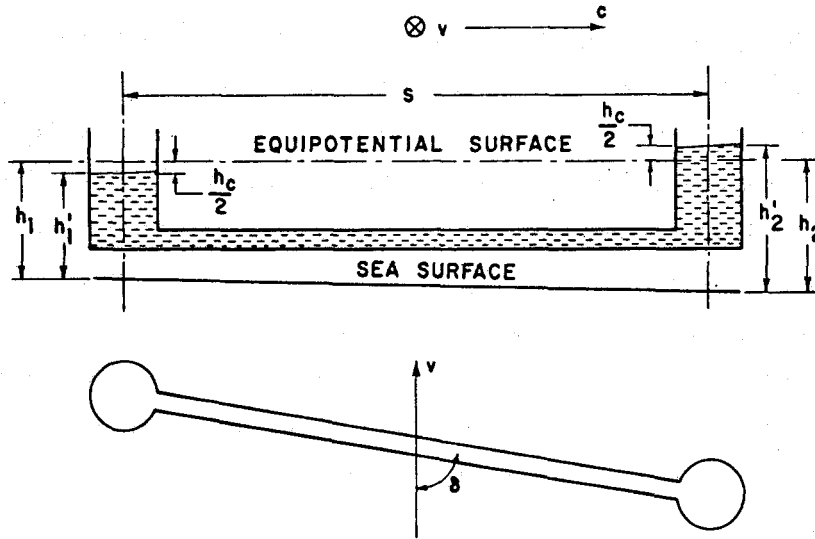


Fig. 7. Effect of the Coriolis force. A level moving with the angle δ to the velocity vector v is deflected by the amount $h_c/S = (2v\omega \sin\phi / g) \cos\delta$, where ω is the earth's angular velocity and ϕ is the latitude.

$$\frac{h_c}{S} = \frac{2v\omega \sin\phi}{g} \cos\delta \quad (12)$$

where δ is the angle between the level axis and the velocity vector. The observed tilt is $\alpha_o = (h_1' - h_2')/S$, and the true tilt (as measured relative to the equipotential surface) is

$$\alpha_t = \frac{h_1 - h_2}{S} = \frac{h_1' - h_2' + h_c}{S}$$

or

$$\alpha_t = \alpha_o + \frac{2v\omega \sin\phi}{g} \cos\delta \quad (13)$$

If the ice moves at the same velocity as the water, then the ocean tilt is entirely due to the Coriolis force and we would observe no tilt, because

$$\alpha_t = \frac{2v\omega \sin\phi}{g}$$

The velocity that produces an apparent tilt equal to the sensitivity of the level (1.6×10^{-7} radians) is, in the polar region, $v = 1.1$ cm/sec, or 40 m/hr. By comparison, the accuracy with which the relative velocity can be determined, for instance, by Transit satellite navigation is of the order of ± 2 cm/sec averaged over two or three observations per hour. For Decca and similar radio navigational aids the accuracy is of the order of ± 0.5 cm/sec, and by ranging from sonar transponders on the ocean floor the corresponding value is of the order of ± 0.1 cm/sec. Therefore, to make full use of the potential accuracy of the hydrostatic leveling system, precise radio navigational aids or sonar ranging methods must be used in determining the drift velocity.

ACKNOWLEDGMENT

Thanks to the Polar Continental Shelf Project of the Department of Energy, Mines and Resources for its support.

REFERENCES

- Eaton, J. P. 1959. A portable water tube tilt meter. *Bull. Seism. Soc. Am.*, 49, 301-316.
- Egedal, J. 1937. Observations of tidal motions of the earth's crust. *Geof. Publ.*, 11, Oslo, Norway.
- Eto, T. A. 1966. A recording water tube tilt meter. *Bull. Disaster Prevention Res. Inst.*, 15, 21-33.
- Hunkins, K. 1962. Waves on the Arctic Ocean. *J. Geophys. Res.*, 67, 2477-2489.
- Johannessen et al. 1970. Cruise report from the ice drift studies in the Gulf of St. Lawrence, 1970. Marine Sciences Centre, Manuscript Report No. 15, McGill University, Montreal, Quebec.
- Scheel, G. 1956. Systematische Fehler des hydrostatischen Nivellements und Verfahren zu ihrer Ausschaltung. Deutsche Geodatische Kommission, Reihe B, Heft 27.
- Waalewijn, I. A. 1964. Hydrostatic levelling in the Netherlands. *Survey Review*, 17.

Weber, J. R. 1972. Ocean tilt. *AIDJEX Bulletin No. 14*, Univ. of Washington, Seattle, Wash., pp. 32-34.

Weber, J. R., and K. L. Lillestrand. 1971. Measurement of tilt of a frozen sea. *Nature*, 229(5286), 550. (Reprinted in *AIDJEX Bulletin No. 6*, 1971, pp. 1-9.)

ICE ISLAND REPORT

by

Pat Martin and Alan Thorndike

AIDJEX

The Canadian Polar Continental Shelf Project notified the AIDJEX Office in April 1974 that a large ice island was located about 160 km north of the MacKenzie River delta. The U.S. Office of Naval Research expressed interest in the ice island as a possible site for a research station to replace the one on T-3, and as a possible logistics base for AIDJEX operations in 1975-76. The AIDJEX Office offered to place a buoy on the ice island to be tracked by the Interrogation, Recording, and Location System (IRLS) of Nimbus D, and NASA agreed to operate the system through autumn 1974 for this purpose.

An extensive search to find the island again was begun in late April. By the time the ice island was sighted again, two Canadian groups, PCSP and the Canadian Defence Reconnaissance Group, and three U.S. groups, the U.S. Navy Fleet Weather Facility Ice Observing Group, the Naval Oceanographic Office Birdseye mission, and the Naval Arctic Research Laboratory, had flown at least 15 missions in the search area. As a rule, the visibility on these flights was poor, affording only a patchy view of the ice from high altitude and a much reduced field of view from low altitude. Fleet Weather relocated the ice island on 14 June at 71°31'N, 135°45'W and reported two pieces sighted. PCSP made three flights during the week of 17 June from the base at Tuktoyaktuk, but were unable to find the ice island due to poor visibility and lack of precise aircraft navigation.

A Decca radio positioning network was scheduled to go into service for PCSP on 1 July, but plans were made to get the transmitting stations on the air immediately after the operating crews were on station. Good signals were available from all stations on 23 June, and plans were made to search for the island on 24 June with a Twin Otter aircraft on lease to the Canadian

Beaufort Sea Project. An estimate of the drift of the ice island since the last reported position was made based on the local winds in Tuktoyaktuk. The indicated drift was to the west-southwest about 60 kilometers, and search patterns were chosen for both good and poor visibility based on the estimated drift.

The weather for the search flight was good, with only small, thin patches of low clouds. The sea ice on the course to the last reported ice island position was fractured and loose, but without any extensive open water. The pilot for the flight was Don Korody. Frank MacLean, chief of Decca operations, was along to monitor Decca performance. Bob Grauman represented the Canadian Atmospheric Environment Service and the Beaufort Sea Project. Pat Martin, Phil Taylor, and Alan Thorndike, all from AIDJEX, were on board to assist in the navigation and search.

The primary navigation aid for this flight, and all later flights, was Decca. Frequent readings were taken to ensure that errors did not occur in the lane counts due to brief interruptions in the radio signals. Only one such interruption occurred during any flight, and that was on a return to Tuktoyaktuk, which required no precise position reference. The excellent performance of the Decca system despite the rush to get into operation was a major factor in the success of the operation.

Position fixes were also obtained from bearing measurements to several radio navigation beacons on shore as a backup for Decca. These fixes appeared to be good to within a few miles except for occasional easily recognized errors.

Because of the good weather and excellent visibility the search was flown at 4500 meters altitude. The ice island was found 50 kilometers from the previous position on the first search leg. The surface conditions on the ice island, especially melt ponds, blended with the surrounding sea ice to a surprising degree, and the actual sighting was made directly over the island when the lineations were clear. The two pieces reported by Fleet Weather were the result of one end of the island having broken loose since April. The two pieces were still in contact at one point, although the smaller piece had shifted a few hundred meters and rotated slightly and was

surrounded by open water. A third piece of glacier ice, about 700 meters long and 70 meters wide, was found about two miles southeast of the island, probably broken from the smaller piece since April.

Pictures were taken from high altitude and complete circuits were flown around the islands at both high and low altitude. The islands were free of other active fractures and were in no apparent danger of further breakup. The freeboard of the islands adjacent to open water appeared to be only a meter or so. Some small piles of rocks not seen in the April photos were sighted in a heavily hummocked area on the south side of the larger piece. Eight fuel drums were spotted in a central area of the larger piece. A VHF beacon was dropped near the drums as a homing aid, but the range of this unit turned out to be too short to be of any value. No attempt was made to land and the plane returned to Tuktoyaktuk.

A total of three flights were made to the ice island on 25 and 26 June in a Bell 205 helicopter piloted by Ed Porcho that was at the disposal of PCSP in Tuktoyaktuk. The flying time to the islands from Tuk was about two hours. The passengers on the first helicopter flight were Frank Hunt, Field Manager for PCSP, Bob Grauman of AES, and Pat Martin and Alan Thorndike of AIDJEX. The objectives were to install an experimental automatic weather station with magnetic tape recording and satellite data relay via ERTS, which installation would provide valuable experience to the AES-Beaufort Sea instrument development program, to perform a preliminary survey of the dimensions and freeboard of the larger island, and to recover fuel drums and rock samples to aid in the proper identification of the island. Hunt and Grauman made the installation immediately adjacent to the fuel drums near the center of the widest part of the larger island, and dug out the drums. Two were returned to Tuk. Martin and Thorndike collected samples of rock, dust, and snow, measured the island's freeboard along the edge that had recently opened, and did the survey. A long, narrow, refrozen crack was seen near the south edge of the island.

Upon arrival back in Tuktoyaktuk, Frank Hunt invited Warren Denner, Director of the Naval Arctic Research Laboratory in Barrow, Alaska, and Richard Dickerson, Chief Pilot of NARL, to inspect the islands on a flight the next day. The invitation was accepted and plans were made to depart

for the ice island shortly after the arrival of the visitors from NARL on the 26th. The second flight departed the evening of the 25th to install the first IRLS buoy and investigate the long crack and hummocked area along the south side. The passengers were Pat Martin, Phil Taylor, and Alan Thorndike, who installed the IRLS buoy near the drums and AES automatic station and drilled holes through the ice of the hummocked area and the refrozen crack.

The passengers for the final flight on the 26th were Warren Denner and Richard Dickerson of NARL, Frank Hunt of PCSP, and Pat Martin, Phil Taylor, and Alan Thorndike of AIDJEX. The objectives were to install a backup IRLS station on the second-largest ice island fragment, to familiarize Denner and Dickerson with the islands, and to drill through the sea ice on the northwest corner of the larger piece. Unfortunately, the visibility at the islands was no better than a few hundred meters, which made it impossible to get a complete view of the islands, but the general size and surface features were apparent, and the buoy installation and drilling were successfully completed. It was necessary to take on fuel at the Decca station located on Hooper's Island on both the outbound and inbound legs due to the additional load and maneuvers in flight on this trip. Two additional pieces of what appeared to be glacier ice were seen within a few miles of one another at 71°N, 138°W on these trips. Both pieces were about one kilometer long. One was about one half a kilometer wide and the other was much narrower. Some thick blocks of sea ice had rafted onto the surface of the larger piece and a fragment had broken off across the entire width of one end.

DISCUSSION

Ice Morphology

Measurements of the principal dimensions of the larger island were made by theodolite survey, freeboard measurement, and drilling. Five flags were set out on prominent pressure ridges along the perimeter of the largest piece of ice, and these were surveyed from the buoy installation near the center of the island. Two 90 m base lines were laid out. The angles to

the five targets were measured with an optical theodolite. The results of the triangulation, tabulated in Table 1, were internally consistent to about 1%. In the direction of the lineations, the island is about 7 km long; its width perpendicular to the lineations is about 3 km.

TABLE 1
COORDINATES OF SURVEY TARGETS

Target	x [m]	y [m]
A	3700	-1100
B	4100	730
C	100	1700
D	-2900	-670
E	330	-1600

A sketch has been prepared based on these measurements and oblique aerial photographs taken in April and June, and details of the ice island surface features have been added from direct observations (Fig. 1). A slight indentation on the northwest shoreline of the larger piece holds a narrow embayment of flat sea ice which is about 1 km in length and 2 m thick ($x = -0.8$ km, $y = 1.2$ km). This ice might be suitable as an unprepared landing site. Access to the ice island is not obstructed by a pressure ridge.

Another embayment near the middle of the southeast side of the island is quite different from the first ($x = 1.5$ km, $y = -1.5$ km). The hummocks on its surface are about 1.5 m high and the appearance is distinctly different from the adjacent ice island, the border between the contrasting surfaces being marked by an intermittent ridge 0.5 m high. The only rocks found on the island were on this piece, including one boulder 0.5 m in diameter. The rocks were all angular and unsorted. Because of the unusual appearance of this area a hole was drilled through the ice in a level spot to determine the thickness, 9 m. The wetter ice and saltier taste which is common in the ice flakes from near the bottom of holes drilled through sea ice were absent in this hole. It may be that the hummock field can be

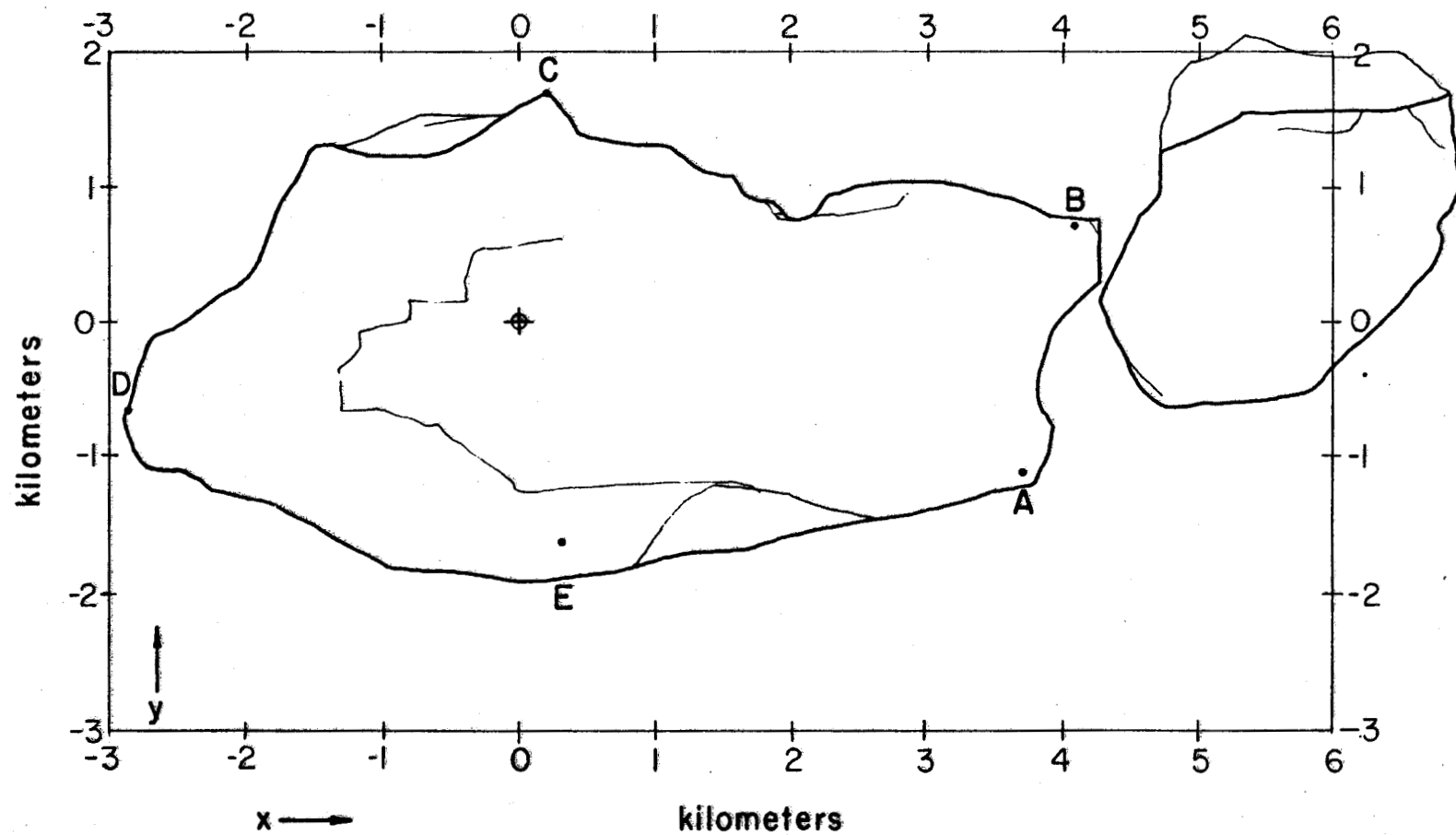


Fig. 1. Sketch of ice island (survey targets A-E).

explained by the variations in surface melting due to the presence of the rocks themselves, or to conditions which may have prevailed at the time the rocks were originally deposited on the ice. The small ridge at the contact with the less disturbed portion of the ice island might be explained by a large force applied to the hummock field.

A long refrozen fracture in the ice island begins near this hummock field ($x = 2.5$ km, $y = -1.5$ km) and runs along and across lineations over several kilometers on the large end of the bigger piece. In some places the width is clearly seen to be about 30 m, with distinctly parallel edges and a faintly visible medial crack. The thickness of the ice in this fracture was found, by drilling, to be about 4 m, which effort was interrupted by several thin and distinctly harder layers. The spacing of these layers about a meter apart permits the conjecture that they may be annual growth features in the ice, perhaps fresh ice formed from water trapped under the sea ice in the crack each summer. The medial crack was only about 30 cm wide and the ice was 15 cm below the level of the thicker sea ice. There were no clear signs of recent motion along the crack. In fact, it was not obvious where the other end of the crack intersected with the edge of the island. Near-vertical photographs suggest that there may be some relationship between the location of the crack and marked differences in the surface features of the ice island. If the island were to part along the most plainly visible portion of the crack, the effect would be to make the width of the larger piece more nearly uniform.

The only other fractures noticed were short and very narrow, along the lineations nearest and parallel to the ice island edge. It is possible that, as the ice island thins, the lineations, which are in fact depressions a few feet deep, become weak spots along which the ice fractures. Such a hypothesis would explain the strongly rectangular shape of the smaller ice island fragments seen on this trip.

Thickness

The two large pieces of ice had separated quite recently, leaving a clean break along which freeboard measurements were easily made. Since the

fracture runs normal to the lineations, the freeboard varies widely from troughs to ridges. The troughs were filled with snow and slush and generally had active drainage streams in them. The ice surface at the lowest points in the trough must have been very near sea level, but, because of the thick filling of slush, no measurements were made. Freeboard along the ridges ranged from just over 1 meter to just over 2 meters. In places it was possible to step over to a nearby piece of ice and look back through the lead to see the ice island's edge. The edge appeared very smooth and vertical and went out of sight (estimated 10 m). There was no apparent rounding or tapering of the ice island's surface near this fracture. We conclude then that the mean freeboard is in the neighborhood of 1.5 m and the total thickness about 15 m [Crary, 1954]. It would be interesting to have more information on the relationship of thickness to surface topography.

Rocks

The terrestrial origin of the ice island was evident in the concentrations of dust over most of the surface and in the presence of several rock piles in the hummocked area. Most of the rocks were sharply angular, and fresh surfaces were common, suggesting reduction of larger pieces by freeze-thaw action. The dust was found concentrated at the snow-ice interface and along exposures at crack and drainage features. In places the dust had concentrated to the extent that cylindrical holes a few inches in diameter were being melted several inches into the ice. Samples of the dust and rocks were recovered for analysis and possible identification of the source area.

Fuel Drums

The fuel drums found on the larger ice island fragments were empty and partially rusted. They were painted drab brown and carried U.S. military markings for automotive gas dated 1957. The history of these drums is being investigated. From the evidence gathered to date, it is not unlikely that the ice island calved off the Ward Hunt ice shelf along the northern coast of Ellesmere Island in 1967. It may be possible to identify the surface features of the island from photographs of the ice shelf of that time.

Automatic Stations

The one IRLS buoy with the configuration proven in the successful operation of the IRLS array following AIDJEX in 1972 has communicated successfully with Nimbus D. Unfortunately neither the AES-ERTS data relay nor the backup IRLS installation has communicated successfully with their respective satellites to date. The AES data recording experiment is presumed to be working. Position and engineering data are being received from the IRLS buoy for one orbit each day. The ice island was within 30 kilometers of its position on 26 June in early September, when westward drift resumed, following the seasonal pattern common in this area at this time of year. The position of the island on 29 September was 72°20'N, 146°02'W. If the island follows the drift of other tracked floes and islands, it will be north of Point Barrow by late winter, and northwest of Point Barrow in the summer of 1975. Because it is relatively thin, it seems unlikely that the ice island will run aground along this track.

SUMMARY

An extensive search in poor visibility finally reestablished the position of the ice island reported by PCSP. This search phase was a major effort, and the relocation of the ice island by Fleet Weather was a signal accomplishment. In the future, such searches would be greatly eased by the deployment of tracking and homing devices at the earliest moment. Following relocation several visits were made to the ice island to deploy instrumentation and to investigate the island. The results of this investigation are that the ice island's origin can probably be determined, and that the morphology of the ice islands is such that they would be suitable for research stations. The tracking by NASA is proceeding on a daily basis, and it should be possible to revisit the island easily.

REFERENCE

- Crary, A. P. 1954. Seismic studies on Fletcher's Ice Island, T-3. *Trans. Amer. Geophys. Union*, 35, pp 293-300.

REPORTS FROM THE PRINCIPAL INVESTIGATORS AIDJEX LEAD EXPERIMENT

In March and April 1974, scientific research groups from three universities participated in a lead experiment on the sea ice north of Point Barrow. The experiment, a part of AIDJEX, was designed to gather information about the interaction between the ocean and the atmosphere through open and freezing leads as well as to test equipment that will be used in the main AIDJEX year, 1975-76.

The reports that follow describe the activities of some of the studies carried out as part of or in conjunction with the lead experiment. The first two reports, by Kelley and by Smith, were submitted soon after the investigation was concluded and are more narrative and preliminary than the Geophysical Institute papers.

To orient the reader, we are repeating here--in slightly shortened form--the logistics coordinator's journal that appeared in Bulletin 26. [For a more complete account, see A. Heiberg, AIDJEX Lead Experiment, spring 1974, field operations report, *AIDJEX Bulletin No. 26* (September 1974), p. 23-31.]

23 February - 3 March. Preparation for artificial lead experiment on Elson Lagoon proceeding without difficulties. Program three days behind schedule due to late arrival of instrumentation. Deployment to lagoon scheduled for 4 March. Aerial reconnaissance 1 March over ice north Barrow encouraging. Several good leads observed 10 miles out. Deployment to ice anticipated around 11 March.

4 March. Experimental pond for artificial lead laid out on Elson Lagoon 4 miles northeast of camp. OSU and UW huts lifted to site by helicopter.

5 March. Instruments set up at pond by OSU and UW. Smith's group assembling instrumentation in preparation for deployment to ice next week. OSU and UW trouble-shooting sensor installation at lagoon.

- 6 March. Aerial reconnaissance to ice. Conditions continue favorable. UA ready for deployment to lagoon. OSU and UW still trouble-shooting.
- 7 March. UA set up at lagoon. Artificial lead still dry, awaiting solution to OSU and UW instrumentation problem. Modification to electronics circuitry in progress. Aerial reconnaissance continues.
- 8 March. OSU and UW equipment operational, pond to be flooded and artificial lead experiment to commence tomorrow. Deployment to ice scheduled for middle of next week.
- 9 March. Small pond established on lagoon for UA research. Ten m (radius) pond for OSU and UW filled with water at noon and steady flow established. Wind direction shifted and made existing pond unsuitable. New 10 m enclosure laid out. Helicopter on ice reconnaissance. Ice thickness tested adjacent to leads.
- 10 March. Smith's group assembling and installing equipment in huts.
- 11 March. New 10 m pond for OSU and UW filled with water and good data are collected through the night. UA still having pumping problems in small pond. Holmgren collecting data over large pond.
- 12 March. OSU, UW, and Holmgren finish work at second pond in early morning. Wind direction changes again and equipment is moved back to first pond, where the experiment gets going by early afternoon.
- 13 March. Reconnaissance to ice in R4D. UA experiment running at lagoon. OSU and UW finish at lagoon in late afternoon. Briefing by helicopter pilot and Coast Guard radio preparation for Friday deployment.
- 14 March. Helo huts moved back from lagoon and all buildings test-lifted by helicopter. Two Cessnas loaded and readied for next day's deployment. Late evening, the oceanographic team develops computer problems and deployment is postponed till 16 March.
- 15 March. Computer problems solved, everybody ready, manifests made up for 7 helicopter flights and 6 Cessna flights,
- 16 March. Final briefing at 7:30. Cessnas with Paulson, Smith, Toovak, and Lee off at 9:20. No suitable leads spotted by 11:00 within 25 miles of Barrow.
- 17 March. Cessna search for lead unsuccessful. If no lead is found tomorrow, oceanographic group will be deployed to a floe to check out equipment.
- 18 March. No lead by 12:30. Smith's group deployed to floe 17 miles north of Barrow. Problems with powerheads and auger for drilling holes causes delay in deployment, but by 7:00 p.m. Camp 1 is in operation, occupied by five oceanographers and one native support assistant.

19 March. Cessnas find lead at 11:00 and set down 20 miles north of Barrow. The lead is about 50 m wide and one mile long. UW, OSU, and UA programs deployed and in operation at Camp 2 by 4:00 p.m. Smith is at Camp 1 checking out his instrumentation. Weather calm, -30°F.

20 March. Helicopter flight to both camps to fix radios and supply Smith with spares. At camp 2, measurement continuing over thin ice crust. Late evening wind opens the lead again.

21 March. Experiment at camps 1 and 2 completed. At 3:00 p.m. everything is lifted back to NARL.

22, 23 March. Investigators checking and overhauling instrumentation in preparation for next deployment, scheduled for 24 March.

24 March. Cessnas off at 9:15, one with Paulson, Smith, and Toovak, the other with camp gear and Smith's drilling equipment. Target search area is a 24-mile sector north of NARL. By 10:30 no suitable lead is found; one Cessna loses alternator and mission is called off.

25 March. Cessnas off at 8:45. Same configuration as yesterday. Cessnas report lead 18 miles north of Barrow at 10:00. By 4:00 p.m., six helicopter and seven Cessna flights have shuttled everything to the ice except the UA generator and backup supplies. OSU and UW set up and running by 1:00. Five buildings and 17 people on the ice, including a radio repair man and a native support person. At 4:00 the camp radios for helicopter assistance. The lead is closing, the ice is ridging and threatening the downwind buildings. The helicopter is on its way to relocate buildings and start evacuating. The Air Force is asked to assist in evacuating the camps if necessary, but things quiet down and only the downwind side is evacuated. By 7:00 p.m. the last flight to the ice carried UA generator in a sling. Components of the generator tear off in flight and UA crew, being without power, return to NARL. Three huts, seven people left on the upwind side. Smith and Badgley collecting data through the night.

26 March. UA helo hut evacuated. Scientific programs terminated on the ice at noon. Everything is back on the beach by 2:00. Kelley's program on the ice terminated, Holmgren still involved.

27, 28, 29 March. Daily searches produce no leads.

30 March. Search in the morning and afternoon produces no lead. Still no change in weather. Winds out of northeast at 10 knots. Contingency plan worked out: If no lead by next week, OSU and UW will go back to the lagoon for a 20-m artificial lead experiment, and Smith will be deployed to a floe to take STD and current data. Ohtake from UA flies ice crystal sampler. A pond enclosure is constructed on the lagoon.

31 March. No change in weather, search produces no leads. Ohtake flies crystal sampler.

- 1 April. No weather change and no lead discovered in the morning. Ohtake flies crystal sampler. UW and OSU huts moved to lagoon.
- 2 April. No leads in the morning. Weather stable. Smith is deployed to a floe 24 miles from Barrow. UW and OSU in operation at the 20-m pond on the lagoon by early afternoon. Holmgren flies crystal sampler in the morning and terminates his program. OSU and UW collecting data through the night.
- 3 April. Twenty-meter pond frozen over and the program on the lagoon terminated by noon. Smith collects STD and current data on the floe down to the bottom (100 m). UW and OSU calibrating in the afternoon.
- 4 April. No leads. The RF 2200 radio in Smith's camp operates satisfactorily with double antenna, frequency 4625.
- 5 April. No leads. Smith moved back to NARL. Paulson, Smith give seminar on lead experiment in the NARL lounge.
- 6 April. No weather change. Search in the morning produces no lead.
- 7 April. Wind picks up, 20 knots at 90 degrees. Search in the morning indicates that the ice is moving; no acceptable leads, however.
- 8 April. Big lead (300 m) discovered at 018° and 28 miles. Too wide for OSU and UW, who terminate their program and start packing. Smith's group deployed and in operation by 5:00.
- 10 April. Smith's group evacuated after a successful experiment at the lead. The Lead Experiment is terminated. Scheduled departure from Barrow
12 April.

EFFECT OF OPEN LEADS ON THE EXCHANGE OF CO₂ BETWEEN THE ATMOSPHERE AND SURFACE SEA WATER

by

John J. Kelley
Institute of Marine Science
*University of Alaska, Fairbanks, Alaska 99701**

BACKGROUND

The influence of carbon dioxide on the global heat balance of the earth-atmosphere system has caused increasing concern over the last decade. From observations it may be generalized:

1. Before 1970, CO₂ was increasing at a rate of approximately 0.7 ppm per year (0.2 percent). Recent data show that this rate is now more than 1.0 ppm per year.

2. The rate of increase is probably due to the combustion of fossil fuels, and the amount of combustion is rising steadily.

3. The annual average concentration mixing ratio of CO₂ in the Arctic is 1 ppm higher than in the Antarctic.

4. There is a distinct seasonal oscillation of CO₂ concentration. The amplitude at the surface is about 12 ppm in the Arctic and about 1 ppm in the Antarctic, and it decreases with increasing altitude above the ground.

5. The sea water under the ice-covered arctic seas (Beaufort, Chukchi) is generally supersaturated in CO₂ with respect to air except when local phytoplankton blooms occur.

6. Subpolar seas that have distinct ice-free periods and are close to land (Barents, Kara, Bering) show equilibrium CO₂ concentrations varying from 100 ppm to more than 500 ppm. These wide variations are attributed to the effects of plankton blooms and influx of CO₂ from large rivers.

Carbon dioxide may be a useful tracer for elucidating and quantifying vertical and horizontal mixing phenomena in the oceans of the world. Although

*Temporarily with the Office of Polar Programs, National Science Foundation.

there is now a data base for the equilibrium partial pressure of CO_2 in surface water of several areas of the arctic and subarctic seas, there is still not much information on seasonal changes and even less on PCO_2 (partial pressure of CO_2 in water) in open leads and in the seasonal ice margin waters of the Beaufort and Chukchi seas.

The AIDJEX lead experiment off the coast of Barrow in spring 1974 provided an opportunity to evaluate the equilibrium partial pressure of CO_2 and the exchange of CO_2 between the air and the sea. With the aid of an AIDJEX-supported helicopter, NARL aircraft, and a modular laboratory it was possible to locate these experiments quickly at newly opened leads. Although ice conditions were less than favorable, we feel that the quality of the data we obtained is high enough to allow some initial predictions.

PARTIAL PRESSURE OF CO_2 IN WATER

Measurement of PCO_2 assumes that Henry's Law applies: the concentration of the gas dissolved in a liquid will be directly proportional to the pressure of the gas in equilibrium with the liquid. This may be expressed for CO_2 as

$$\text{PCO}_2 = X_{\text{CO}_2} P_t = [\text{CO}_2]_{\text{ppm}} P_t \cdot 10^{-6}$$

where X_{CO_2} is the mole fraction of CO_2 , which may be expressed as the volume mixing ratio in ppm, and P_t is the barometric pressure. Thus, at 1 atmosphere pressure, a concentration gradient of 1 ppm across the air-water interface is numerically equivalent to a partial pressure gradient of 1 microatmosphere.

PCO_2 at the sea water surface of artificial and natural open leads was determined by measuring the CO_2 concentration of air in equilibrium with the water by infrared spectrometry. The equilibrator consisted of a floating chamber in which air was cycled in a closed system (1 to 1.5 liters per minute) from the equilibrator to the gas analyzer and back to the chamber, where it was released to a frit just below the water surface. During the ambient air and reference gas portion of the cycle, the chamber was flushed

with air. Water vapor was removed from the air stream prior to analysis. Concentration of CO_2 were converted to standard pressure and reported in parts per million by volume (ppm/v) on a dry air basis. CO_2 partial pressure gradients across the air-water interface are calculated so that a positive number indicates that the water is supersaturated with respect to air ($\text{PCO}_2 - \text{pCO}_2$, where pCO_2 is the partial pressure of CO_2 in the air).

Preliminary evaluation of the data shows that the sea water in the natural lead approximately 26 km north of Barrow (19 March) was supersaturated in CO_2 with respect to air: the level of PCO_2 was 25 ppm more than the concentration of CO_2 in air, which was 333 ppm. The values for PCO_2 at the NCEL test site on ocean ice approximated those of the natural lead; but the data from the Elson Lagoon artificial lead were considerably different, varying from 70 to 100 ppm more than the ambient air, with one 24-hour period showing a strong diurnal trend.

Elson Lagoon is an extensive area of shallow water (less than 2 m deep under the artificial lead site) with few deep channels, and there is probably very little interaction with the sea. Where the salinity of the surface water in the natural lead varied between 32.14 ppt and 32.16 ppt, the salinity of the water pumped from beneath the ice on Elson Lagoon exceeded 42 ppt (42.414 ppt on 13 March). We had not expected any close correlation between the lagoon and the sea water, but we performed the CO_2 analyses to observe possible consequences of changes in water chemistry on the local biota.

RATE OF EXCHANGE

To estimate the amount of CO_2 transferred to or from the atmosphere when open water is exposed to the air, we measured the rate of exchange of CO_2 across the air-sea boundary. Our method, which uses a floating chamber, approximates a free or diffusional exchange rate as opposed to a force or turbulent rate. Therefore, our measurements would represent the minimum flux of CO_2 through the water surface. Although the chamber prevented direct wind stress on the water surface, some wave action was noted in the

chamber, so that the measured evasion ratios probably lie somewhere between free and forced rate values. We evaluated the CO₂ rate coefficient α :

$$\alpha = \frac{dQ/dt}{\Delta P} \cdot \frac{1}{A} \cdot 10^{-6}$$

where α = CO₂ rate coef, mg cm⁻² atmos⁻¹ min⁻¹

dQ/dt = time rate of change of CO₂ in chamber, mg min⁻¹

ΔP = PCO₂ (water) - pCO₂ (chamber).

We were able to measure the rate of exchange of CO₂ once across an open lead on the sea ice and once at the artificial lead on Elson Lagoon. These data are now being evaluated.

ACKNOWLEDGMENT

The AIDJEX logistics group and the NARL staff handled this experiment very efficiently. Funding support was provided by the Office of Naval Research, contract N00014-67-A-0317-0001AB.

OCEANOGRAPHIC INVESTIGATIONS DURING THE AIDJEX LEAD EXPERIMENT

by

J. Dungan Smith

Department of Oceanography

University of Washington, Seattle, Wash. 98195

The oceanographic component of the AIDJEX Lead Experiment was designed to provide information on the mechanical and thermodynamic processes active in the mixed layer of the Arctic Ocean that are directly attributable to the presence of open leads. Four deployments were made, the first and third to large floes of sea ice, the second and fourth to leads. The oceanographic and atmospheric experiments were to have been performed simultaneously on both edges of leads at the same locations so that heat and salt flux calculations could be compared and subsidiary tasks shared by both projects [Paulson and Smith, 1974]. Although this plan for joint work could not be followed because of the lack of sites suitable to both groups, the fact that both research groups were working in the same general area at the same time makes joint use of the two data sets feasible. For example, predictive theories based upon results from the artificial lead experiment carried out in early April permit heat flux estimates to be made from results of the last and most fruitful oceanographic experiment, on 8-10 April.

First Deployment

The first oceanographic deployment, to check the instruments and determine the general density and velocity structure over the Continental Shelf north of Point Barrow, was made on 18 March to a floe several hundred meters in diameter and 1.8 m thick, set tightly in thinner and more fractured ice. We quickly began to cut instrument holes through the ice with a 40 cm ice auger. Both the auger and its subsequent replacement broke down while we were cutting the second hole. We were finally able to repair it temporarily by replacing its rivets with bolts and bending the two outmost cutter teeth with vise grips to readjust the pitch, and the holes were

completed and the huts set in place. The ice chisel belonging to Kenny Toovak was found to be far superior to ours, and we used it in later deployments. But even with a properly working ice auger and Toovak's ice chisel, making a 1 m hole through ice ranging from 1.5 to 2 m in thickness is a difficult task and takes at least four man-hours.

Although no leads were seen in the immediate vicinity of the camp when it was established, the surrounding ice loosened up considerably during the first night. At about 0600 hr on the second morning, a crack propagated through the ice of the camp and went directly between the skids of a hut and under the generator tent. Fortunately it did not open and the building did not have to be moved until later in the day. That afternoon several large cracks, from 10 to 80 cm wide, propagated through the ice sheet on which the camp was situated. These ice motions were accompanied by surging in the instrument holes and vibration of the ice sheet, a situation quite similar to one observed at Camp 200 in 1970 [Coachman and Smith, 1970].

Two animals visited the camp during the three-day experiment. One, a small polar bear, arrived on the first day while the ice auger was being repaired and the camp had been quiet for some time. The other, a large ring seal, came up through the large instrument hole, saw us, and dove, to reappear a few minutes later in the 40 cm hole in the other hut.

The day after we established our first camp, the atmospheric group occupied a lead site that would have been suitable to both groups. Since we had had such difficulty cutting holes on the previous day and the equipment check-out was still incomplete, we decided to remain at the first camp rather than move to the lead location. At this time we thought there would be sufficient opportunity for joint work in the next three weeks. The choice to remain at the first camp was a good one, as the floes in the vicinity of the lead site had drifted into an undesirable configuration by the time the oceanographic camp could have been disassembled, moved, and reestablished.

Second Deployment

The second deployment was accomplished according to plan by both the oceanographic and the atmospheric groups. The experimental site was an

excellent one and the camps were assembled smoothly. The ice auger problem had been corrected at Point Barrow between deployments by adding a support to the cutting teeth. Unfortunately this camp was short-lived and oceanographic measurements were not obtained at both upwind and downwind locations; the downwind site became part of a pressure ridge before the first CTD lowering. Although the upwind camp was not abandoned until the following day, the current meter mast remained unassembled because of the hut's uncertain fate. Extremely interesting density structure was observed at this site.

Third Deployment

After returning to Point Barrow on the afternoon of 26 March, several minor repairs were made and the two short current meter masts were merged into one long one. After searching without success for leads for the next five days, we finally decided to deploy both huts to a multiyear floe on 2 April. At the first two camps the density profile had differed considerably from what we expected to find, in that there was no pronounced surface mixed layer. The third experiment was planned as a repeat of the first under more favorable conditions--namely, a complete absence of leads within several tens of kilometers of the camp. The equipment was operating properly and the results of this deployment were excellent.

Fourth Deployment

The search for leads continued without success until 7 April, when the wind speed finally began to increase again. A few leads were found that day, but none was suitable as an experiment site. The last search leads was planned for 8 April, and we decided to deploy no matter what was available. After an extensive search, an acceptable frozen lead was located. It had good polar ice on each side and several areas of open water. Unfortunately the wind was blowing directly down the lead rather than across it, and the areas of open water were geometrically complicated. Nevertheless, camps were established and data were being recorded by 2200 hours. Current and density data were collected until the afternoon of

10 April, when the camp was evacuated. Seals were often seen playing in the open water, and they very likely investigated the shiny current meter masts; for lack of any other explanation we attribute destruction of one current meter triplet to their curiosity.

PRELIMINARY RESULTS

Typical profiles of temperature and sigma- t for the last three oceanographic deployments--designated as ALEX (2), (3), and (4)--are shown in Figure 1. In Figures 2 and 3, examples of measured current profiles from the third and fourth experiments are given. Because of the wind direction and lead geometry, both camps during the last experiment produced results characteristic of downwind sites, so that the density profile in Figure 1 from ALEX (4) appears to be typical of ambient conditions in mid-April.

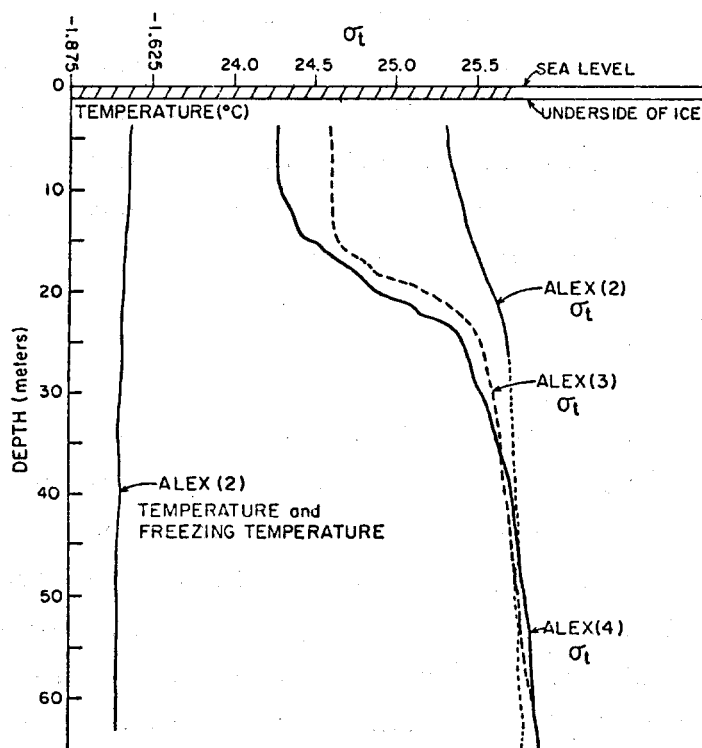


Fig. 1. Typical temperature and density profiles from various deployments during ALEX.

The long periods during which no leads could be found were also times of low wind speed; thus, the interval between ALEX (2) and ALEX (4) was one of quiescent meteorological conditions. The data indicate that the mixed layer became more strongly stratified with time during this quiet period, and the total fresh-water content on the shelf appears to have increased. Although spatial and temporal coverage is not sufficient to substantiate this suspicion, the mean profile taken at ALEX (4) is suggestive of southern Beaufort Sea conditions, and the temporal change of shelf water characteristics shown in Figure 1 appears to be due to decreased mixing of shelf-generated brines with Beaufort Sea water being advected into that region from the east.

Calibration of the CTD was checked by comparing the measured-temperature profiles in the mixed layer with freezing-temperature profiles calculated for that region using the equation of Fujino et al. [1974]. This procedure is accurate to about 1 millidegree and $0.02 \text{ }^{\circ}/\text{oo}$. Examination of randomly chosen profiles taken during the last three deployments confirmed that the conductivity cell worked properly and maintained an accuracy in excess of the $0.02 \text{ }^{\circ}/\text{oo}$ required for the experiment. In addition, many of the profiles examined to date show agreement between the measured temperature and the freezing temperature (at zero pressure) to better than 5 millidegrees throughout the entire water column, a result that demonstrates a surface origin, although not necessarily a local one, for the shelf water. Profiles taken during ALEX (2) show particularly close agreement in this regard. The temperature profiles for ALEX (3) and ALEX (4) have weak thermoclines in the vicinity of the haloclines, ones produced by the salinity dependence of the freezing temperature. Because the records have not yet been corrected for the differing time constants of the temperature and conductivity sensors, they have not been examined in detail for microstructure; however, weak layering can be seen on the halocline in some of the salinity profiles.

Data from ALEX (3) and ALEX (4) as well as occasional profiles from ALEX (2) indicate a mixed layer depth on the order of 16 m with a sharp pycnocline extending to 25 m. At the former location a jet centered deeply in the mixed layer with a velocity maximum ranging between 5 and 8 cm/sec was observed. The core of the jet was at 15 m when the camp was first

established, but it rose to 12 m during the first day. A typical velocity profile for this feature is shown in Figure 2. A shallower jet was found at ALEX (4). In this case the velocity maximum was less than 0.5 m beneath the ice and ranged between 3 and 12 cm/sec, the high values occurring in the late evening when the winds picked up and the low values occurring in mid-day when the wind speed was lower. Diurnal variations in insolation also may have been a factor in this daily velocity cycle, and proper separation of these effects will be possible as results from the artificial lead experiment become available. Even under maximum flow conditions, measurable velocities occurred only in a zone 5 m thick. The jets at ALEX (4) were oriented directly toward an area of open water about 200 m away and supplied fluid to the surface of that "pond," replacing material lost to the brine plume beneath. Lead-driven convection of this general type has been observed previously by Smith [1973], and is described by Smith [in press]. Jets of the type found at ALEX (3), also discussed in those reports, are manifestations

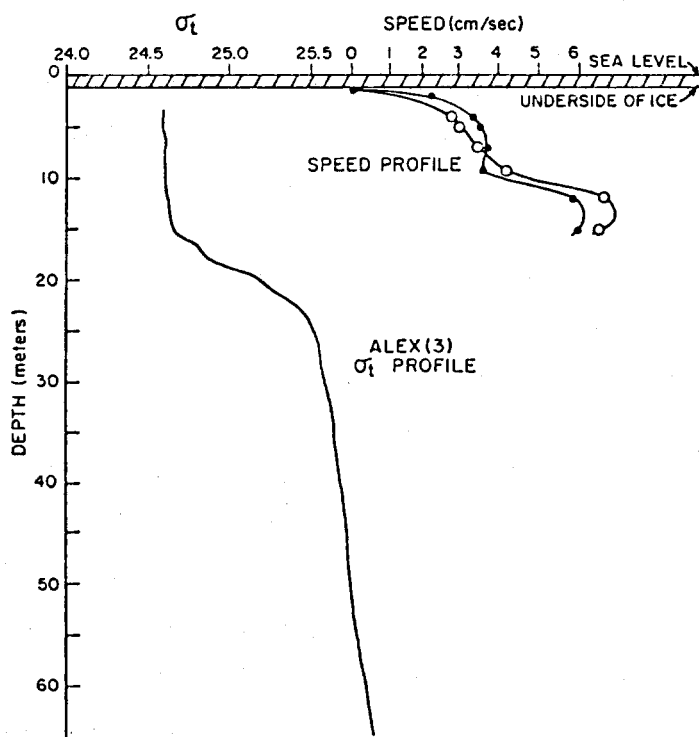


Fig. 2. Velocity and sigma- t profiles from ALEX (3).

of brine plumes incapable of penetrating the pycnocline; therefore, they run out along the base of the mixed layer. The source of the plume found during our third deployment was not in the immediate area of the camp and could not be located precisely; however, the flow was from 125° true north, making the shore lead a possible source. Data from the 1972 AIDJEX investigation indicate that such flows can be observed several tens of kilometers away from their source.

Profiles such as those shown in Figures 2 and 3 vary considerably with time; nevertheless, an attempt was made to calculate local Richardson numbers. For ALEX (3) data the results based upon 40-minute averages, such as graphed in the two figures, ranged from 1 to 10 except in the region only a few meters beneath the ice. However, when data averaged over only a few minutes were used, local shears increased and were sufficient to bring the Richardson number below its critical value of $1/4$, indicating the importance of temporal variations in profile shape. Similar results

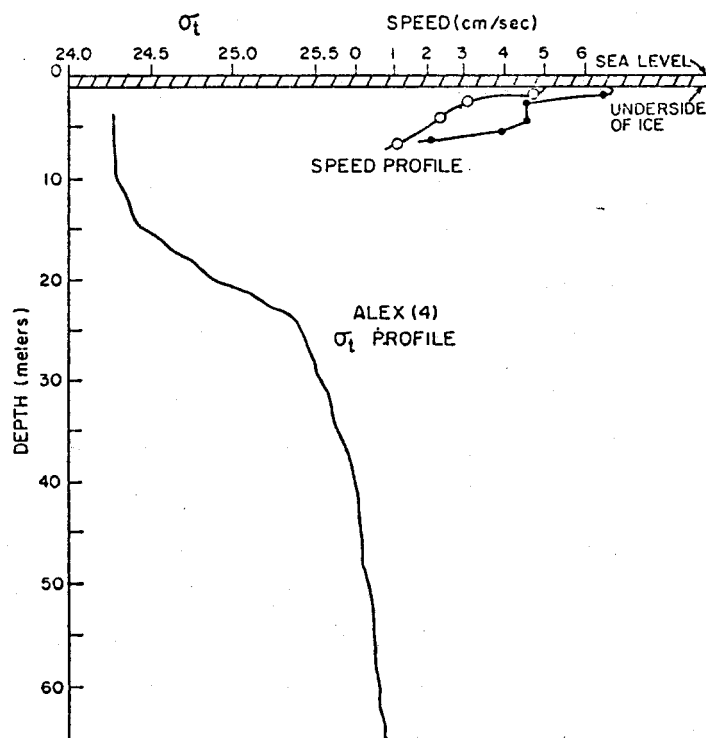


Fig. 3. Velocity and sigma- t profiles from ALEX (4).

were obtained from the ALEX (4) data; thus, it appears that wall-generated eddies are sufficient to maintain shear turbulence only in the upper few meters of the flow. In the deeper layers, shear instabilities arise at the edges of the jet when the flow becomes more uniform in the interior and less so at the extremities. Less heavily filtered profiles of the latter type are similar in character to the more structured 40-minute average data shown in Figures 2 and 3.

Navigation of the ice camps was accomplished through radar positioning of aircraft just prior to landing at the sites. This technique is not sufficiently accurate to provide usable drift rate calculations, but it is suitable to make ice drift speeds in excess of 1.0 cm/sec (approximately 1.0 km/day) extremely unlikely, precluding the possibility of shifting the zero reference significantly.

Unlike the events previously reported by Smith [1973], the jets shown in Figures 2 and 3 persisted for several days in an approximate steady state resulting in their modification by the Coriolis effect. In that report, Smith envisioned the deeper turbulent jets as expanding until the critical Richardson number was attained at their edge and then flowing in an essentially inviscid manner. Under these conditions the Coriolis effect would cause the jet to rotate to the right until it was flowing more or less parallel to the lead instead of normal to it. However, the pressure gradient would have to increase with distance down the lead to accommodate the increasing mass flux and cause the flow to accelerate.

More detailed information about lead-driven flow will become available as analysis of the ALEX data proceeds. However, due to a scarcity of suitable experimental sites, the ultimate goal of the project was not accomplished and probably will not be until a new experiment is staged from a sea ice camp. The presence of land to the southeast, the shallow water and shore lead on the inner shelf, and the limited helicopter range all combined to reduce drastically the area in which leads could be occupied. In addition, the possibility that a camp might drift out of helicopter range prevented us from using lead sites in the northwest sector. With a base on sea ice, drift would be more or less the same at the central and lead camps

and so would greatly reduce the danger of drifting out of helicopter range, as well as provide a full-range, 360°, area in which to search.

The mechanical and thermodynamic processes associated with lead convection have not yet been fully elucidated and, although the AIDJEX lead experiment has substantially increased our knowledge in this area, the lead experiment as originally planned is still required. The spring 1974 endeavor has shown that such an investigation would be feasible from a sea ice camp with presently available logistical and oceanographic techniques.

REFERENCES

- Coachman, L. K., and J. D. Smith. 1971. A report on the 1970 AIDJEX Pilot Study. *AIDJEX Bulletin* No. 4, 8-38.
- Fujino, K., E. L. Lewis, and R. G. Perkin. 1974. The freezing point of sea water at pressures up to 100 bars. *Journal of Geophysical Research* 79(12), 1792-1798.
- Paulson, C. A., and J. D. Smith. 1974. The AIDJEX lead experiment. *AIDJEX Bulletin* No. 23, p. 1-8.
- Smith, J. D. 1973. Lead-driven convection in the Arctic Ocean. *EOS*, 54(11), 1108-1109 (abstract only).
- Smith, J. D. Turbulent structure of the surface boundary layer in an ice-covered ocean. *Proceedings of the 1972 ICES Symposium on the Physical Processes Responsible for the Dispersal of Pollutants in the Sea, with Special Reference to the Nearshore Zone*. *Rapports et Proces-Verbaux Series*, ed. J. W. Talbot and G. Kullenberg (in press).

TURBIDITY IN THE ARCTIC ATMOSPHERE

by

B. Holmgren*, G. Shaw, and G. Weller
Geophysical Institute, University of Alaska
Fairbanks, Alaska 99701

ABSTRACT

Pyrheliometric and photometric measurements during the AIDJEX pilot studies in April 1972 and March 1974 show unexpectedly high values of the turbidity as expressed by the Ångström turbidity coefficient β . Vertical profiles of the optical extinction coefficient measured by airborne photometers indicate a peak in the extinction coefficient in the lower troposphere (300 m) in spring; this is attributed to ice crystal aerosols, and the aerosol production is explained in relation to open leads and moisture entrainment into the boundary layer. A secondary peak at about 2 km height is considered to be a semi-permanent haze layer, possibly of man-made origin, which is advected into the Arctic Basin.

INTRODUCTION

For the past few years, the Geophysical Institute at the University of Alaska has conducted studies of radiation fluxes over arctic surfaces aimed at determining the physical characteristics of pack ice, clouds, and aerosols as they affect the arctic radiation regime. In one of these studies during the 1972 AIDJEX pilot study, pyrheliometric measurements showed that the total turbidity of the atmosphere was higher than expected. The technique used for the turbidity determinations is an old one, introduced by Ångström [1929, 1930] as a means of separating the effects of the extinction by aerosols and water vapor in the atmosphere. It does so by the use of cut-off filters that divide the total solar intensity into separate bands.

*Now at Meteorologiska Institutionen, Observatorieparken, Uppsala, Sweden.

To determine the effects of leads in producing ice crystal aerosols, the transport of these aerosols throughout and above the boundary layer, and the effect of aerosols on atmospheric transmission, the Geophysical Institute continued its investigation during the AIDJEX lead experiment with a study of the boundary layer structure as monitored by a fairly recent tool, the sodar (acoustic radar) [McAllister, 1968]. To bridge the gaps between seemingly disparate measurements, vertical profiles of aerosols were obtained with an airborne sun photometer, size and concentration of ice crystals by sampling at the surface, and temperature and humidity profiles from twice-daily radiosoundings at Barrow.

INSTRUMENTS AND OBSERVATIONS

The sodar measurements and most of the pyrheleimetric and aerosol measurements were made at the NOAA Observatory near the Naval Arctic Research Laboratory four miles from Barrow. The sodar system and the main results of the sodar soundings have been described elsewhere in this Bulletin [Holmgren and Spears, 1974]. The determination of the Ångström turbidity coefficient was made using a Linke-Feussner actinometer with a quartz filter and Schott color bandpass filters OG1 and RG2 with upper cutoffs at $\lambda = 0.525$ and $0.630 \mu\text{m}$, respectively, and lower cutoffs at $2.8 \mu\text{m}$. The actinometer outputs were recorded on a portable battery-driven recorder that was checked against a precision mV-meter three times during the observation period of one month. Only the factory calibration was available for the actinometer itself; however, the resulting β -values were checked by simultaneous measurements with a multifilter, monochromatic sun photometer [Shaw, Reagan, and Herman, 1973].

Figure 1 shows a comparison between the Ångström turbidity coefficient β , as determined from the Linke-Feussner measurements, and the aerosol optical depth τ_M , derived with the multichannel sun photometer evaluated at $\lambda = 1 \mu\text{m}$ (τ_M is numerically equal to β at a wavelength of $1 \mu\text{m}$). The agreement between the two values is reasonably good--for the most part within ten percent--in spite of the sensitivity of the derived values of β to many subtle measurement and instrument errors [Shaw, 1974]. The rather good

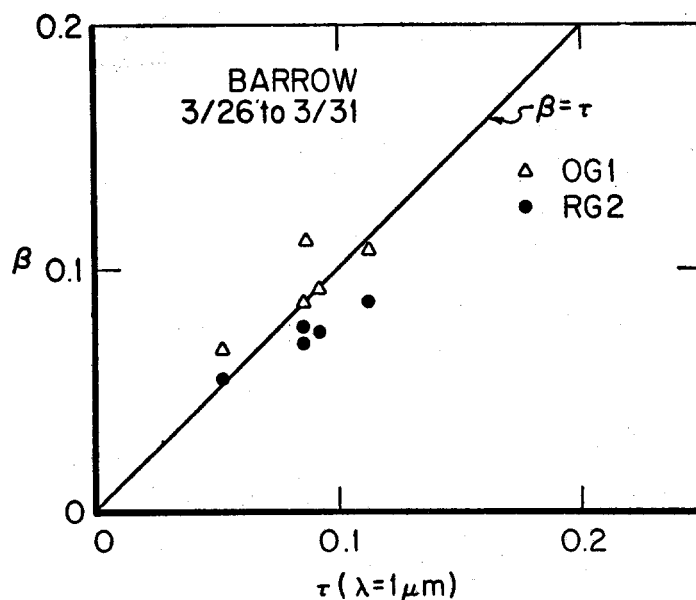


Fig. 1. Comparison between Ångström turbidity coefficient β , as determined from actinometer measurements, and the aerosol optical depth derived from multi-wavelength photometer measurements at $1 \mu\text{m}$.

agreement between two types of instruments gives confidence in the techniques used for analysis and serves as a check against unsuspected errors that can easily crop up in precision radiation measurements.

In addition to ground-level measurements of total vertically integrated optical depth, we also derived the vertical distribution of the volume extinction coefficient, β_{ext} . This was done by measuring the change in direct solar radiation at various altitudes with an airborne sun photometer. The instrument employed two narrow-band optical filters located at mean wavelengths of $0.55 \mu\text{m}$ and $0.85 \mu\text{m}$. Thus it was possible to derive the vertical profile of volume extinction coefficient in the midvisible and near infrared.

RESULTS OF PYRHELIOMETRIC MEASUREMENTS

Daily values of the Ångström turbidity coefficient β are plotted in Figure 2, while the intensities of total direct solar radiation are plotted in Figure 3. Asterisks in Figure 2 indicate days when ice crystals were

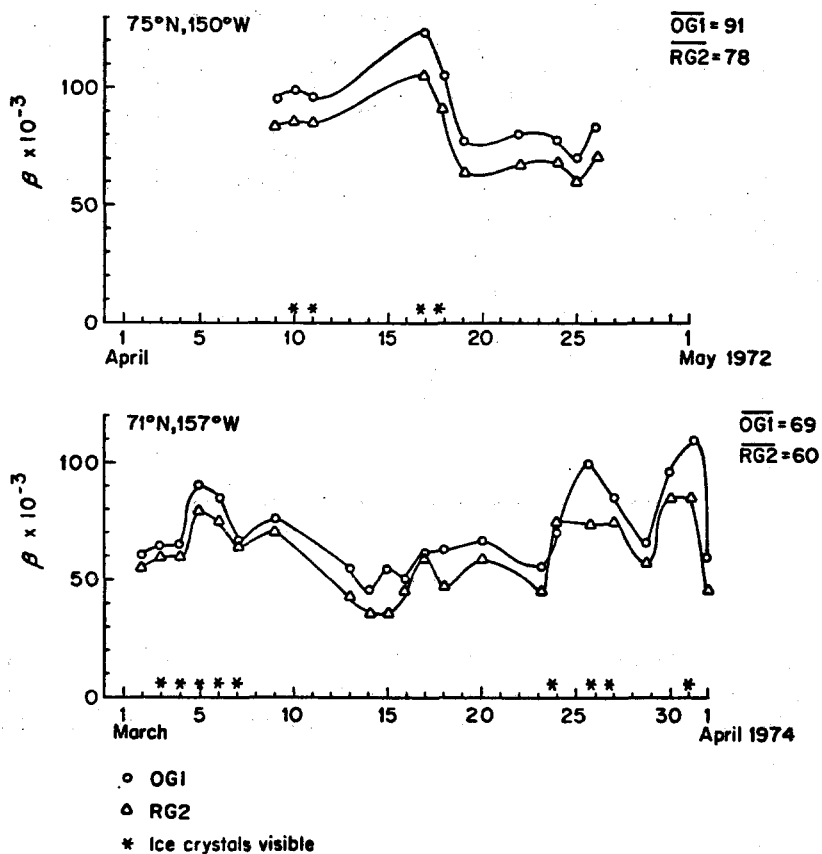


Fig. 2. Daily values of the Ångström turbidity coefficient β . Asterisks indicate days when ice crystals were visible.

visible. The incidence of visible ice crystals and high turbidity values (low solar intensities) are strongly correlated in Figure 2, although the correlation is by no means invariable.

The day-to-day variations in the 1974 Barrow data (lower part of Fig. 2) must not be taken too strictly, since the daily values are based on only one or, at the most, two determinations of β , usually around noon. Sudden short-period changes in surface visibility were noted a few times to cause large variations of the β -values. The daily values of April 1972, based as they are on eight or nine measurements per day on the average, should ensure more reliable daily means. In the 1972 data there was a tendency for the maximum β -values to appear in the forenoon.

The variation of atmospheric turbidity with time is even more sharply reflected in the variations that were observed in circumsolar sky brightness.

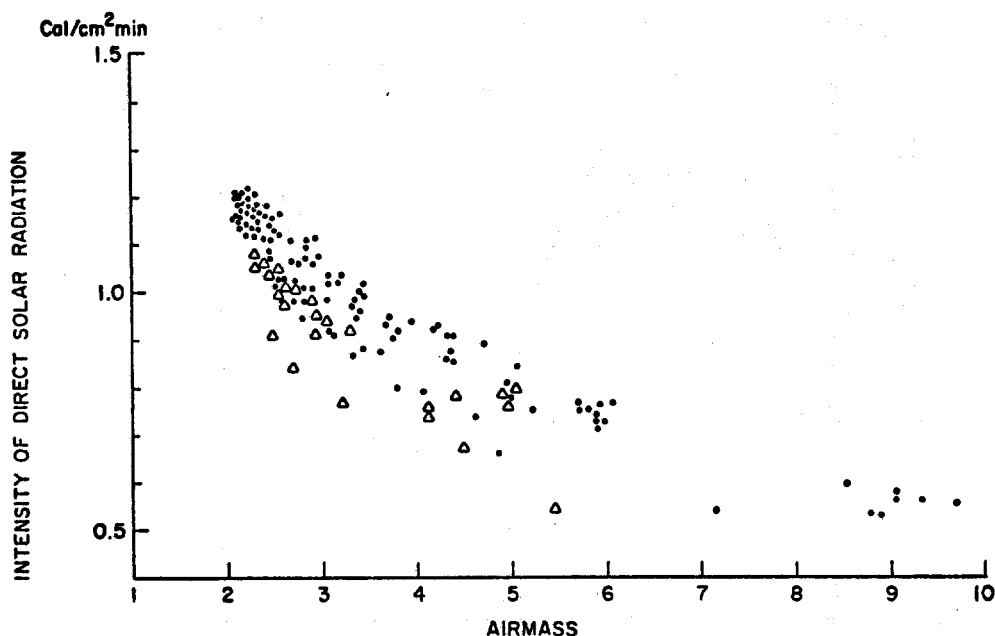


Fig. 3. Intensity of the direct solar radiation as a function of airmass at Barrow during March 1974 and at the AIDJEX camp, 75°N, 160°W, in April 1972. ● OG1 Δ RG2.

This is because the brightness of the sky near the sun is more or less directly related to enhanced forward-scattering or diffraction of sunlight by the ice crystals.

The curves in Fig. 4 show circumsolar sky brightness at mean angular distances from the sun of 1.2° (upper curve) and 6.2° (lower curve) throughout the day on 26 March 1974. Calculations of sky intensity for a pure molecular (Rayleigh-scattering) atmosphere, including effects from multiple scattering and reflected diffuse radiation from the surface, fall numerically about one order of magnitude below the lower curve shown in Figure 4. That is to say, the sky brightness at 6.2° from the sun is enhanced by about a factor of ten over what it would be in an absolutely pure atmosphere. The aureole "brightening" is even more marked at 1.2° from the sun (upper curve in Fig. 4).

Of special interest is the large temporal variation in circumsolar sky brightness, which incidentally fluctuated from minute to minute in response to the turbulent motions in the field, but is shown greatly smoothed. At

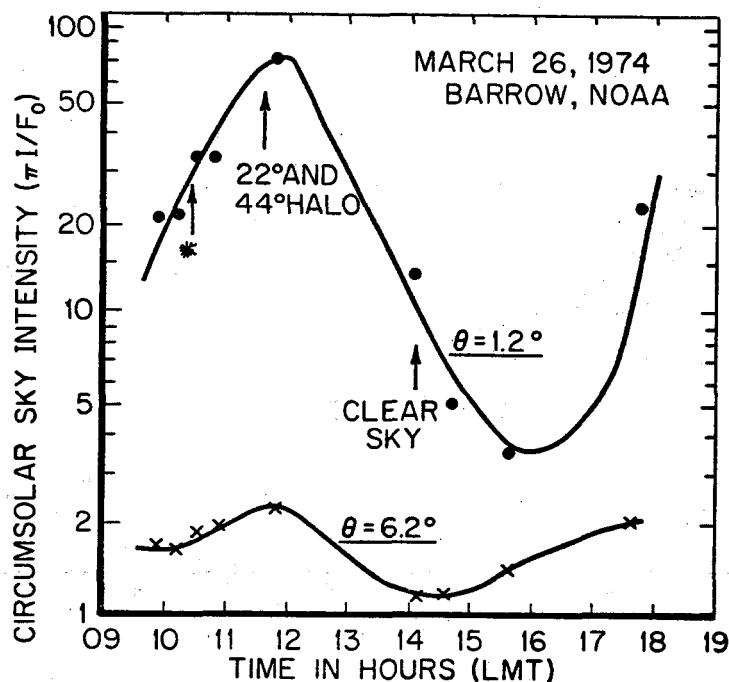


Fig. 4. Circumsolar sky brightness, $\pi I/F_0$, evaluated at angular distances of 1.2° and 6.2° from the sun throughout the course of a day at Barrow.

1030 AST a "diamond dust" display of ice crystals was noted. As the concentration of ice crystals increased in the morning, the sky brightness increased accordingly, until finally at about 1200 AST the display was sufficiently well developed to cause visible optical phenomena, including a 22° and 45° circumsolar halo and the start of a circumzenithal arc. Apparently the ice crystal precipitation then subsided throughout the afternoon with an attendant decrease in circumsolar sky brightness; this was especially pronounced at small angular distances from the sun. Finally, in late afternoon the sky brightness once again started to increase, indicating another buildup in ice crystal precipitation. A similar "reverse" pattern was noted in the total optical depth, although it was not nearly so dramatic or on so large a scale as the variations in sky brightness.

On the average, the observed β -values are probably too high to be ignored in radiative budget calculations of the arctic atmosphere. Holmgren [1971] found β -values of about 0.030 on Devon Island in the Canadian Archipelago in May 1962. The β -values at Barrow and over the pack ice are generally

more than twice as high as might be expected from those previous studies in the polar regions.

The visual observations indicate that several atmospheric processes are involved that explain the high turbidity at Barrow. The most apparent of these are discussed below:

1. It is often difficult to distinguish between cloud-free and cloudy conditions when high tenuous cirrus layers are present that are very difficult to see. We think that very thin cirrus may have influenced the readings on 3, 4, and 9 March.

2. For several days at the beginning of our observation period the winds were southwesterly, the observation site was on the lee side of Barrow, and the air temperature ranged from -35°C to -45°C . Ice fogs occurred frequently. Although it was difficult to distinguish the ice fog produced by the village in the lower layers from the ice fog formed over open leads west of Barrow, their combined effect definitely influenced the haziness and β -values measured on 3, 4, and 5 March. A similar but weaker effect was noted on 6 and 7 March. As to the rest of the data, the influence of Barrow is, in all likelihood, negligible, since the prevailing winds were northeasterly during the remainder of the observation period.

3. During numerous flights over the pack ice north and northwest of Barrow in search of suitable leads for the Lead Experiment, we encountered pronounced haze layers in the lower troposphere that occasionally reduced horizontal visibility to only a few miles. Especially during a spell of fine weather towards the end of March, the haziness looked like something one might encounter over big metropolitan areas in the south. The vertical profile in Figure 5, which was derived from measurements from aircraft of the direct solar radiation at two wavelengths, confirms these visual observations; it shows a broad haze layer at about 1600 m altitude. Haze layers could sometimes be traced at higher elevation, but they did not seem to be significant during this observation period. Observations of haze layers similar to ours have been discussed by Mitchell [1956].

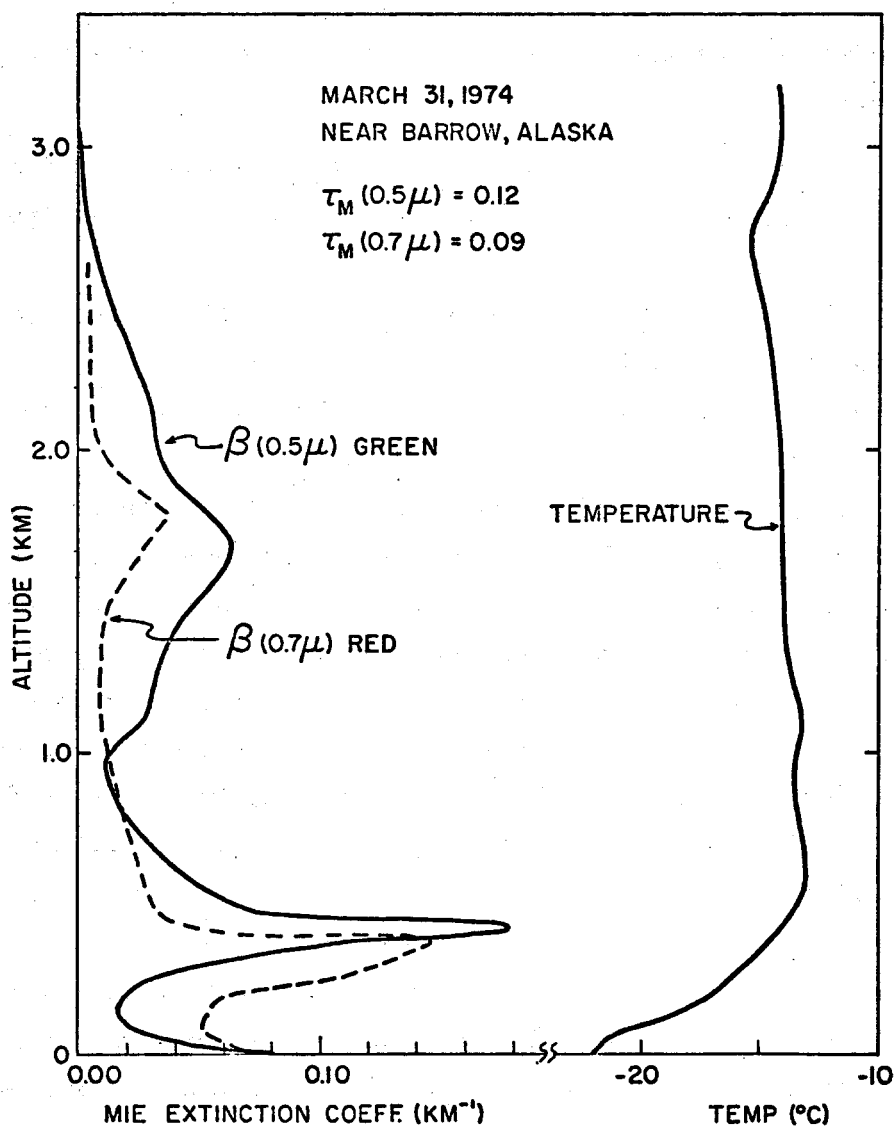


Fig. 5. Vertical profiles of aerosol (Mie) extinction coefficients and temperature.

Relation Between Turbidity and Mixing Layer Phenomena

The visual observations indicate that the highest turbidity values were obtained when there was an increase of aerosols in the lower troposphere. A brief mention of the characteristics of the boundary layer structure as observed from the sodar soundings and the routine radiosoundings may therefore be appropriate at this point.

In March 1974, there was, on the average, an inversion of 12°C from the surface up to an altitude of 1200 m, which was the average elevation for the maximum temperatures as determined from all 62 radiosoundings. The sodar records showed, most of the time, two basic types of atmospheric echoes within the probing range (about 25–650 m above the surface). In the lowest layer there was typically a diffuse backscattering layer in conditions with moderate to strong winds [see Holmgren and Spears, this Bulletin]. This backscattering layer corresponds to a forced mixing boundary layer that was first investigated in detail in the polar regions by Sverdrup [1933]. At the upper part of the mixing layer there is an accentuated echo of the band type, which may or may not be associated with a sharper capping inversion than is apparent from the balloon-borne radiosonde. At higher elevations, there are intermittent multiple band echoes, indicative of wind shearings and turbulence confined to thin sheets between layers of little or no turbulence. The indications are that the exchange coefficients and the turbulent fluxes of sensible heat, water vapor, and aerosols are generally an order of magnitude less within this stable regime than within the mixing layer. The vertical fluxes of momentum may, on the other hand, be associated with internal waves propagating within the upper stable layer and thus go on in spite of the lack of turbulent eddies.

Almost all of the 62 radiosoundings in March showed markedly lower mixing ratios at the surface than at a few hundred meters above the surface. The maximum mixing ratio was, on the average, found at an elevation of 860 m. The average mixing ratio at the surface was 0.33 g/kg and the average maximum ratio was 0.86 g/kg. The cold snow surface obviously serves as a more or less continuous sink for water vapor at this time of year. This is confirmed by energy balance observations reported by Weller and Holmgren [in press]. Also, the relative humidity with respect to water was lower at the surface than a short distance above it in all but a few soundings. At the surface, the humidity was typically at or just above the ice saturation point, which seems to be in accordance with the detailed humidity measurements made by Malmgren [1926] over the pack ice. Above the surface, especially in connection with strong inversions, the relative humidity increased to values of about 100% over a layer that varied from a few meters to several hundred

meters. The physical reality of the high relative humidities may be in doubt, considering that the radiosonde rises rapidly through a strong inversion which might induce riming on the carbon hygistor. However, observations by Ohtake [1970] in similar strong inversions suggest that an accuracy to within 5% may be expected.

Except for open and freezing leads, there are no major atmospheric moisture sources within the Arctic Basin during this time of year. The closest outside source area, and probably the most important one for the Barrow region, is the open seas southwest of Alaska. During some periods the humidity profiles show maximum mixing ratios at elevations that appear remarkably low, although it must be recalled that there is a general subsidence in the lower troposphere over the Arctic at this time of the year. Sample statistics of the humidity profile data show that 50% of all maximum mixing ratios are found below the 600 m level. During the period 26 March-1 April, which was characterized by steady winds out of the northeast sector and a pronounced haze layer roughly a thousand meters thick in the lower troposphere, the average height of the maximum mixing ratio was 500 m above the surface.

In the low part of the haze layers, probably at the top of or just above the mixing layer, the relative humidity was at or close to 100%; humidity in the upper part of the haze layer, however, was occasionally as low as about 50%. A comparison between the visual observations made during helicopter flights and the radiosoundings shows that humidity values above 70%-80% were associated with maximum haziness. This suggests that the haziness was caused partly by water vapor deposits on hygroscopic nuclei. In the upper part of the haze layers, where radiosoundings showed the relative humidities to be lower, a brownish-yellow tinge could sometimes be easily detected. Ice crystals were occasionally observed, either directly in the lowest layers or indirectly by a lower sun pillar. This latter phenomenon was usually seen only as a bright spot, indicating that noticeable concentrations of ice crystals were probably confined to the mixing layer (see below).

When ice crystal precipitation occurred, visibility in the surface layer was typically reduced to a few kilometers. Without ice crystal

precipitation and without high drifting snow, visibility improved to 15-20 kilometers or better. The turbidity and scattering conditions in the lowest layer were obviously most influenced by the ice crystals. By comparing the variations of the mixing layer depth, as obtained from the sodar record, with the variations of the concentrations of ice crystals it was found [Ohtake and Holmgren, 1974] that the ice crystal precipitation occurred primarily when the mixing layer was in an expanding phase. Generally, the mixing layer expanded during the morning hours in connection with increasing windspeed and increasing temperature in the surface layer, i.e., when the stability within the mixing layer decreased because of the increasing incoming solar radiation. On 15 selected days with steady wind conditions and average windspeeds of $5-6 \text{ m sec}^{-1}$ at the 3.5 m level, the mixing layer expanded on the average from 140 m to 185 m between 0900 and 1600 ADT.

With the mixing layer in the expanding phase, warm, humid, stable air is entrained into the cold turbulent mixing layer, probably mostly across a sharp inversion [Sverdrup, 1933]. This mixing across the interface may cause a slight supersaturation with respect to water and may activate ice nuclei; or alternatively, tiny ice crystals may grow to larger ones in the upper part of the mixing layer. During the evening the mixing layer depth decreases in connection with decaying turbulence at the upper part of the mixing layer as indicated by the formation of band echoes on the acoustic records. The entrainment of warm humid air stops and so does the ice crystal precipitation, indicating that the concept of two widely different turbulence regimes is essentially correct.

DISCUSSION

The observations show that the concentrations and the types of aerosols within the mixing layer are generally markedly different from the aerosols above the mixing layer and that the vertical aerosol distribution is critically dependent on the vertical temperature and humidity and wind variations. One natural question that arises concerning the haze layers is whether the open or freezing leads are essential for the high relative and absolute humidities observed at lower elevations. One objective of the sodar measurements

was, if possible, to investigate the influence of open leads on the boundary layer structure. For logistics reasons the sodar in the present study was operated on the tundra at the NOAA Observatory rather than on the pack ice. The minimum distance from the observatory to any open lead was several kilometers. Although wide leads may have had an effect on the depth and character of the mixing layer once or twice, the results were not conclusive [Holmgren and Spears, this Bulletin].

If water vapor from the leads can escape via convection into the stable layers above the mixing layer, one might expect that the residence times for water vapor in the atmosphere may increase drastically. If the moisture transport from a lead into the atmosphere is limited to the mixing layer, most of the moisture will be removed relatively quickly by condensation at the cold snow surface and by ice crystal precipitation; i.e., the effect of the lead will be mostly local. Such direct effects on the aerosols in the mixing layer were observed several times out on the pack ice as well as on the coast at Barrow. If water vapor is trapped above the mixing layer the effects of increased humidities on aerosols may be noticeable over much wider areas and may possibly increase the haziness and indirectly cause ice crystal precipitation far away from the leads, for instance, by entrainment into the mixing layer.

NOAA-3 satellite imagery from 25 March to 1 April shows several major open and freezing leads several kilometers wide stretching for hundreds of kilometers northward from Barrow in a crescent-shaped pattern. Leads of this size, especially when the air traverses several of them, modify the mixing layer considerably. Apart from being a source of moisture, the leads, in freezing, may contribute to aerosol production by releasing sea salt droplets or particles into the air by convection and wind action. After the initial freezing, brine is forced to the surface, probably by pressure building up in the brine pockets. The brine causes salt flowers to grow on the ice by riming. Part of the brine may be carried directly into the air as droplets or, alternatively, the crystals might be carried into the air by the wind action. Also, after freeze-up, the surface on the lead is considerably warmer than the pack ice [see Holmgren and Weller, this Bulletin] and convection may be induced for several days. We often saw a haze over the leads after freeze-up.

There is no doubt that leads contributed to the high turbidity values during the 25 March-1 April period; the lower peak in the extinction coefficient shown in Figure 5 is probably entirely due to ice crystals. However, the upper peak probably has a different origin. We do not presently know the origin of this haze layer, which could be observed horizontally from an aircraft flying at about that altitude (1.6 km) and had a yellowish appearance reminiscent of polluted air over industrial areas.

The effect of the haziness on the energy budget cannot be neglected. The layer of maximum haziness often coincides with the maximum temperature and maximum absolute and relative humidities; the haze layer will therefore cause an increased emission towards the surface and out into space. On the other hand, the extinction of the solar radiation within the haze layer might also increase because of some absorption by dust (indicated by the color of the haze layer) and because of a somewhat increased water vapor absorption in the scattering layer. The net effect of the haze layer is therefore not obvious at the present time.

Turbidity variations in the Arctic thus cannot be ascribed to any one factor. Further studies involving the techniques mentioned here, conventional pyr heliometry, sample collection and analysis of the chemical composition of the aerosols, photometric determinations of vertical aerosol profiles, analysis of the aerosol size distribution, and satellite imagery, are obviously needed before a proper assessment can be made of the role of aerosols in the Arctic energy budget.

ACKNOWLEDGMENT

This work was supported by ONR Contract No. N00014-67-A-0317-0010 and NSF Grant No. GU-40427. Logistic support was provided by the Naval Arctic Research Laboratory. The research is part of the Arctic Ice Dynamics Joint Experiment, coordinated through the AIDJEX Office.

REFERENCES

- Ångström, A. 1929. On the atmospheric transmission of sun radiation and on dust in the air, I. *Geografisker Annaler*, 11, 156-166.
- Ångström, A. 1930. On the atmospheric transmission of sun radiation, II. *Geografisker Annaler*, 12, 130-159.
- Holmgren, B. 1971. Climate and energy exchange on a sub-polar ice cap in summer. Arctic Institute of North America Devon Island Expedition, 1961-1963. *Madelanden fran Uppsala Universitets Meteorologiska Institutionen*, No. 107-12.
- Holmgren, B., and L. Spears. 1974. Sodar investigations of the effect of open leads on the boundary layer structure over the Arctic Basin. *AIDJEX Bulletin* No. 27 (this volume).
- IGY Instruction Manual. 1958. Radiation instruments and measurements. *Annals of the IGY*, vol. 5. New York, N.Y.: Pergamon Press.
- Malmgren, F. 1926. Studies of humidity and hoar frost over the Arctic Ocean. *Geofysiske Publikasjoner*, 4(6), 20 p.
- McAllister, L. G. 1968. Acoustic sounding of the lower troposphere. *J. Atmos. Terr. Phys.*, 30, 1439-1440.
- Mitchell, M. 1956. Visual range in the polar regions with particular reference to the Alaskan Arctic. *J. Atmos. Terr. Phys.*, Special Supplement, p. 195-211.
- Ohtake, T. 1970. Studies in ice fog. Geophysical Inst. Rept. UAG R-211, Univ. of Alaska, Fairbanks.
- Ohtake, T., and B. Holmgren. 1974. Ice crystals from a cloudless sky. *Proceedings of American Meteorological Society Cloud Physics Conference, Tucson, Arizona*, p. 317-320.
- Shaw, G. E. The vertical distribution of tropospheric aerosols at Barrow, Alaska. *Tellus* (in press).
- Shaw, G. E., J. A. Reagan, and B. M. Herman. 1973. Investigations of atmospheric extinction using direct solar radiation measurements made with a multiple-wavelength radiometer, *J. Appl. Meteorol.*, 12, 374-380.
- Sverdrup, H. U. 1933. Meteorology, Part 1: Discussion. *The Norwegian North Polar Expedition with the "Maud", 1918-1925. Scientific Results*, vol. 2. Bergen, Norway.
- Weller, G., and B. Holmgren. The microclimates of the Arctic tundra, *J. Appl. Meteorol.* (in press).

LOCAL RADIATION FLUXES OVER OPEN AND FREEZING LEADS IN THE POLAR PACK ICE

by

Bjorn Holmgren* and Gunter Weller
*Geophysical Institute, University of Alaska
Fairbanks, Alaska 99701*

ABSTRACT

Radiation fluxes were measured over open and freezing leads in the polar pack ice off Point Barrow, Alaska, during the AIDJEX lead experiment in March, 1974. When the leads freeze, the albedo increases rapidly because of internal reflections caused by air bubbles, brine pockets, and interfaces between ice platelets. Rime flowers on the surface also increase the albedo and lower the radiative surface temperature (-15°C) compared with the undisturbed new ice on the lead (-12.6°C) and the adjacent pack ice (-26.4°C). During the freezing process, surface temperatures of the lead drop slowly, however, so that no sharp changes of the long-wave radiation balance occur. Ice deformation and rafting, on the other hand, change the thickness of the new ice and may affect the long-wave radiation considerably. Typically, net outgoing long-wave fluxes for clear skies and moderate winds are of the order of $100\text{--}150$ millical $\text{cm}^{-2} \text{ min}^{-1}$, compared with 50 millical $\text{cm}^{-2} \text{ min}^{-1}$ over the adjacent pack ice. Ice crystals and water vapor produced by the leads cause a flux divergence of the long-wave radiation but do not greatly affect the short-wave radiation balance. Computed radiation balances are -146 cal cm^{-2} over the open water surface of the lead, and -160 cal cm^{-2} for the frozen lead a day later.

INTRODUCTION

During the AIDJEX lead experiment from February to April 1974, the Geophysical Institute of the University of Alaska carried out a program of radiation measurements over both artificial and natural leads as part of its study of the effect of leads in producing aerosols and in influencing the radiation climate of the Arctic atmosphere. One objective of the study was to investigate the connection between the opening of leads and the

*Now at Meteorologiska Institutionen, Observatorieparken, Uppsala, Sweden.

formation of the extensive and distinct haze layers often seen in the first kilometer of the atmosphere over pack ice and adjacent land areas.

This paper is concerned with local modifications imposed by leads on the regional radiation climate. Measurements of atmospheric turbidity, ice crystal aerosols, etc., that are more representative of regional aerosol and radiation conditions are discussed elsewhere in this Bulletin, as are their relation to atmospheric turbulent structures as observed by an acoustic sounder.

OBSERVATIONS AND INSTRUMENTS

Radiation was measured intermittently during a 5- to 6-day period over two artificial ponds made on the smooth shorefast ice of Elson Lagoon, northwest of the Naval Arctic Research Laboratory, and during a 30-hour period at a natural lead 20 km north of Barrow. The instrumentation included two sets of hemispheric radiation sensors, each set comprising two Eppley precision pyranometers for short-wave incoming and reflected radiation and one Fritschen all-wave net radiometer which were mounted on a horizontal boom that could be rotated around a vertical post drilled into the ice. One set of sensors was swung to a position about 1.5 m above the surface of the lead (the pyranometers at about 2 m from the lead edge, the net radiometer about 0.5 m beyond that, at the end of the boom); the other set was mounted over the snow-covered pack ice within a few tens of meters from the lead. Sensor output was recorded on a multichannel potentiometer.

A Barnes PRT-5 thermal radiometer with a field of view of 2° , a band-pass filter transmitting radiation between 8 and $14\text{ }\mu\text{m}$, and a low temperature range that allowed determination of radiation intensities corresponding to -60°C , was used to determine characteristic variations of emissions of the water and ice surfaces. Because of the low air temperatures, both the sensor head and the recorder were lined with insulating material in outdoor operations. Except for a few hours of recording, the emission values were read visually from the meter scale of the instrument.

The Eppley and Fritschen radiometers were each calibrated a few times for short-wave fluxes against a Linke-Feussner actinometer by screening the receiver surfaces from direct solar radiation [Liljequist, 1956]. These comparisons gave calibration constants for the net radiometers that differed less than one percent from those recommended by the manufacturers. The corresponding difference for the pyranometer was of the order of a few percent. The calibrations represented solar elevations about 20° above the horizon. From previous investigations of similar instruments [Liljequist, 1956; Ambach, 1963], it is apparent that the calibration factor for low solar elevations is generally not a constant. We found that discrepancies in the values measured with hemispheric radiometers during the lead experiment occurred at solar elevations below about 5° - 10° . This effect in the net radiometers was probably caused partly by screening of the direct solar radiation by the rim around the receiving upper surface. We will therefore primarily discuss net radiometer data that represent diffuse radiation fields, i.e., either the long-wave fluxes at night or the all-wave fluxes on overcast days. Albedo values for solar elevations less than 5° above the horizon are not included.

To prevent riming on the hemispheres, the net radiometers were equipped with standard heating rings and the short-wave sensors were equipped with a warm-air blower system. These precautions were usually adequate except during the most severe riming conditions at the open leads, when virtually nothing could prevent frost from forming on the instruments within a few minutes after their exposure to the air.

A few times we noticed salt deposits on the hemispheres. This suggests a transport of salt solution droplets into the air via splashing waves and wind. After freeze-up, it is possible that salt solution droplets are carried by the wind into the air when brine trapped within pockets in the ice is forced to the surface. The salt deposits on the hemisphere were removed with distilled water.

Low solar elevations caused problems related to shadows cast by the surface relief. Over water surfaces, the specular reflection of the direct solar radiation was sometimes not included in the recorded output because

of too short stretches of water towards the azimuth of the sun. Ambiguous data caused by the factors mentioned above are not included in this presentation.

EXPERIMENTAL RESULTS

Short-wave Fluxes

The incoming and reflected solar radiation and the net radiation were recorded over leads and pack ice during about five days divided into a few shorter periods. Obviously the measurements are of little interest from a climatological point of view. In order to give a background to the measurements over the leads, a few comments are made on the radiation climate using the more extensive radiation observations made during the AIDJEX experiments in April 1972. Actinometric measurements with Schott color filters OG1 and RG2 resulted in an average value of the Ångström turbidity coefficient β of 0.085 during April and a value of 0.065 for March. These values are from two to three times as high as what might be expected from previous turbidity measurements at sea level in polar regions [Liljequist, 1956; Dahlgren, personal communication]. Although part of the decrease in direct solar radiation is offset by increased sky radiation, the aerosols have an influence on both the short-wave and the long-wave radiation climate that cannot be neglected.

In Figure 1 are shown the variations of the short-wave and long-wave radiation components during AIDJEX in April 1972. It should be remarked that the incoming and outgoing long-wave fluxes were measured with Eppley precision long-wave pyranometers. Since the evaluation of the latter data, we have, in connection with new measuring series and calibrations, come to realize that the Eppley long-wave pyranometers are subject to serious errors especially after prolonged use. The instruments used during AIDJEX 1972 were new and we expect that the long-wave data should give at least the broad features of the variations, since numerous intercomparisons and calibrations were made against the Barnes PRT-5 thermal radiometer. A few notes may be made on the given data:

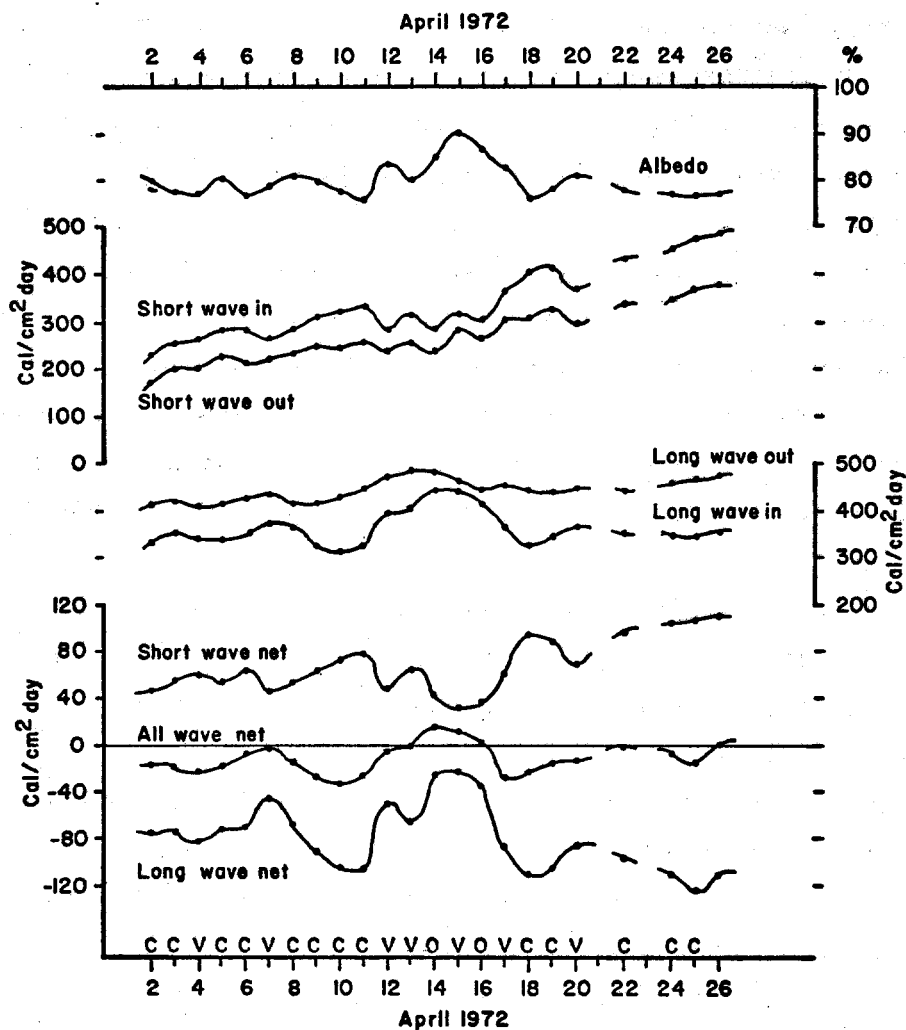


Fig. 1. Daily radiation data, AIDJEX, April 1972.

1. The net all-wave radiation goes from negative to positive daily values on the average. During clear sky conditions the radiation balance is negative or approximately zero at the end of April, while the balance is indicated to be positive with an overcast sky throughout the period.
2. During the cloudy period from 12 April through 17 April the albedo of the snow is notably high. This feature is probably related primarily to multiple reflections between the snow surface and the clouds [Liljequist, 1956]. The incoming solar radiation

becomes enriched in visible radiation, which has a higher reflectivity than the near-infrared radiation. New snow deposited during this period may also have had an effect on the increase of the albedo. A similar increase of the albedo was not observed during the measurements when the solar elevations were considerably lower, in March 1974.

3. The incoming solar radiation does not decrease much when a cloud cover forms over an extensive snowfield. During the six days with overcast sky or varying cloud conditions in the middle of April, the average decrease of the incoming radiation because of the clouds is only about 15%. On the other hand, the *absorbed* short-wave radiation decreases substantially because of the increase of the albedo.
4. During the same days there is a marked increase in the incoming and on the average a small increase in the outgoing long-wave radiation, resulting in a marked decrease of the long-wave radiation losses.
5. The net long-wave and the net short-wave radiation balances are negatively correlated. The variations of the net long-wave radiation are the greater and therefore dominate the variations of the all-wave radiation balance.
6. The atmospheric transmissivity appears to be comparable to values obtained from radiation measurements taken over several years at Barrow [Maykut and Church, 1973]. By comparison, these values are about 10% lower than those observed at the coastal fringe of Antarctica [Liljequist, 1956].

The albedo is one of the most critical factors in the radiation budget for pack ice as well as for leads. In Table 1 a summary of albedo values is given based on half-hourly records of the short-wave fluxes during the lead experiment in March 1974. The albedo values of the snow-covered pack ice fall within the range of 76%-90% as shown in Figure 1. The albedo values of ponds with water depths of 10-30 cm appear to be dependent on the cloud conditions. The albedo of the ponds is partly due to the water surface reflectivity as described to a sufficient degree of accuracy by the Fresnel

TABLE 1

ALBEDO MEASUREMENTS DURING AIDJEX LEAD EXPERIMENT

Day	Time A.D.T.	Albedo %	Surface Types	Clouds
03/09	12-17	84	Wind-packed snow on smooth sea ice.	Variable
03/09	14-17	59-70	Sea ice surface after removal of water in a pond.	Variable
03/10	9-17	82	Wind-packed snow on smooth sea ice.	Sc Ac Ci 10/10
03/10	9-17	64	Refrozen ice surface with a 0.5 mm layer of snow.	Sc Ac Ci 10/10
03/11	9-1730	76	Wind-packed snow, slightly disturbed by activities related to construction of a new pack.	As Ci 10/10
03/11	9-1430	64	Refrozen ice surface with a 0.5 mm layer of snow.	Ci 10/10
03/11	16-1730	40	About 30 cm of water above sea ice.	As 10/10
03/12	8-1730	80	Wind-packed snow over sea ice.	St As Cs 10/10
03/12	8-11	37	About 30 cm of water above sea ice.	As 10/10
03/12	1130-1730	43	Thin new ice on a pond. A water layer is found between the surface ice and the pack ice.	St As Cs 10/10
03/12	11-1830	84	Wind-packed snow with a rime layer on top.	St 1/10 - horizon
03/13	11-13	33*	About 15 cm of water on top of sea ice.	St 1/10 - horizon
03/13	14-1830	53	About 15 cm of water on top of sea ice.	St 1/10 - horizon
03/14	12-18	81	Wind-packed snow with rimed upper layer.	Cs 10/10 Pale sunshine
03/14	12-18	53	Refrozen pond with about 10 cm of new ice above a thin brine layer between the new ice and the pack ice.	Cs 10/10 Pale sunshine
03/20	10-1530	81	Wind-packed snow with knobby surface on pack ice.	Clear
03/20	10-1530	67	Refrozen natural lead ice thickness 8-10 cm. Frost crystals cover surface to 30%.	Clear

*Specular reflection of the direct solar radiation is not included.

law, and partly due to the returns from below the water surface which are governed by the absorption in the water and the pack ice. The albedo values of the artificial ponds appear to be at the upper range of values obtained for meltwater ponds in summer. Because of the cold content of the pack ice, freezing probably occurred at the bottom of the artificial ponds, whereas in summer melting generally occurs at the ice/water interface.

With a dense overcast, the short-wave radiation over an extensive snowfield is practically isotropic [Liljequist, 1956]. The calculated value for the albedo of a water surface is then 6%-7% [Lauscher, 1952]. To get the albedo on clear days, the Fresnel reflection must be calculated separately for the direct and the diffuse radiation. We did not collect any valid albedo measurements over open sea water. When we arrived at the lead on the afternoon of 19 March, the solar elevation was already low and shadows cast by the pack ice edge precluded usable measurements. To give an idea of the range of albedos to be expected, however, we cite some measurements by Ter-Markariantz [1959] as given by Kondratyev [1965]: 7% for a 10/10 cloud cover and 20% for clear skies, representative of pure sea water at a latitude of 70°N in March.

After freeze-up, the albedo of natural leads and ponds increases rapidly because of internal reflections caused by air bubbles, brine pockets, interfaces between ice platelets, etc. Within an hour or so after freeze-up during cold weather, rime flowers start to grow on top of the new ice. Measurements of salt concentrations in the early growth stages of these crystals show values similar to those found for sea water, with the concentration decreasing gradually as the size and number of crystals increase on the young ice. The rapid growth of the rime flowers is likely to be related to evaporation from the relatively warm ice surface, and perhaps also to a relatively low saturation vapor pressure over the brine in the diffusion layer above the ice crystals. The growth of the frost flowers by condensation was also indicated by a higher rate of growth in the direction towards the wind. On floes a few weeks old close to the shore lead at Barrow, we found that the rime flowers under favorable conditions could grow to a continuous carpet a few centimeters thick. The visual observations indicated that the albedo then approached that of the windpacked snow.

As to the albedo measurements on 20 March (Table 1), the albedo under the radiation stand might have been slightly higher than the average albedo over the lead. Even so, the rime flowers on top of the young sea ice are clearly important in the energy budget of the leads during the late winter and early spring period, especially since the amounts of precipitation during this period are low. During AIDJEX in August 1972 albedo measurements of the pack ice by aircraft-borne sensors gave values only a few percent lower for frozen leads than for pack ice [Weller et al., 1972].

Long-wave Fluxes and the Net Radiation

Typical variations of the net radiation over the pack ice and over leads in cloudy and cloudfree conditions are shown in Figures 2, 3, and 4. The diurnal variation of the net radiation over open and freezing leads is obviously much higher than over pack ice because of the lower albedo of the leads. However, because of the inaccuracy of the net radiometers at

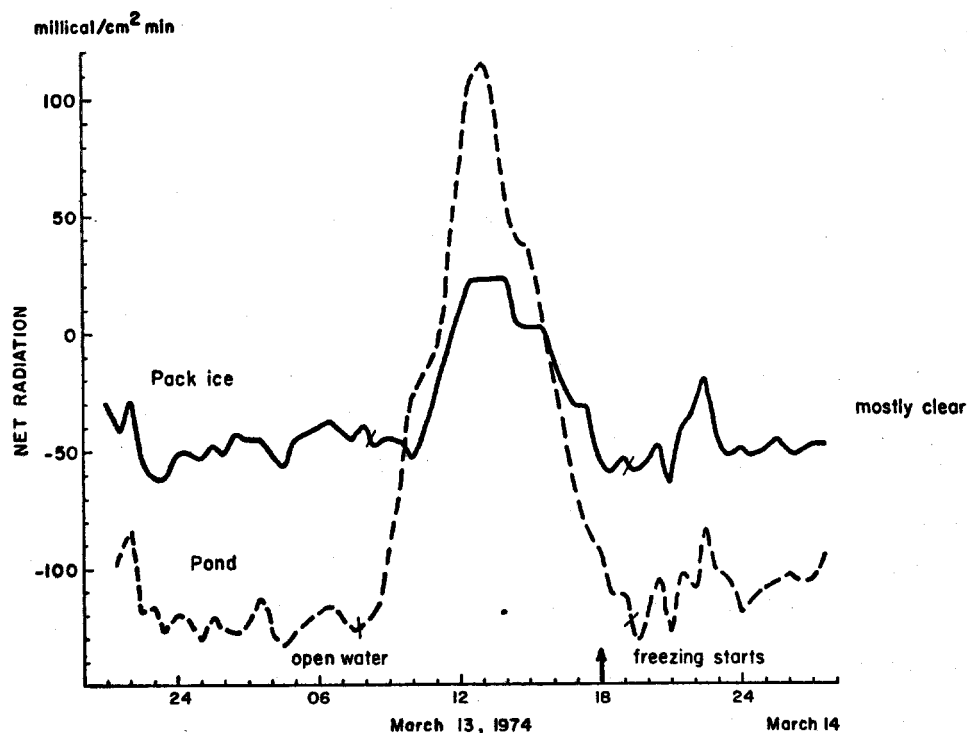


Fig. 2. Net radiation over open water and annual sea ice under cloud-free conditions, March 1974, Barrow, Alaska.

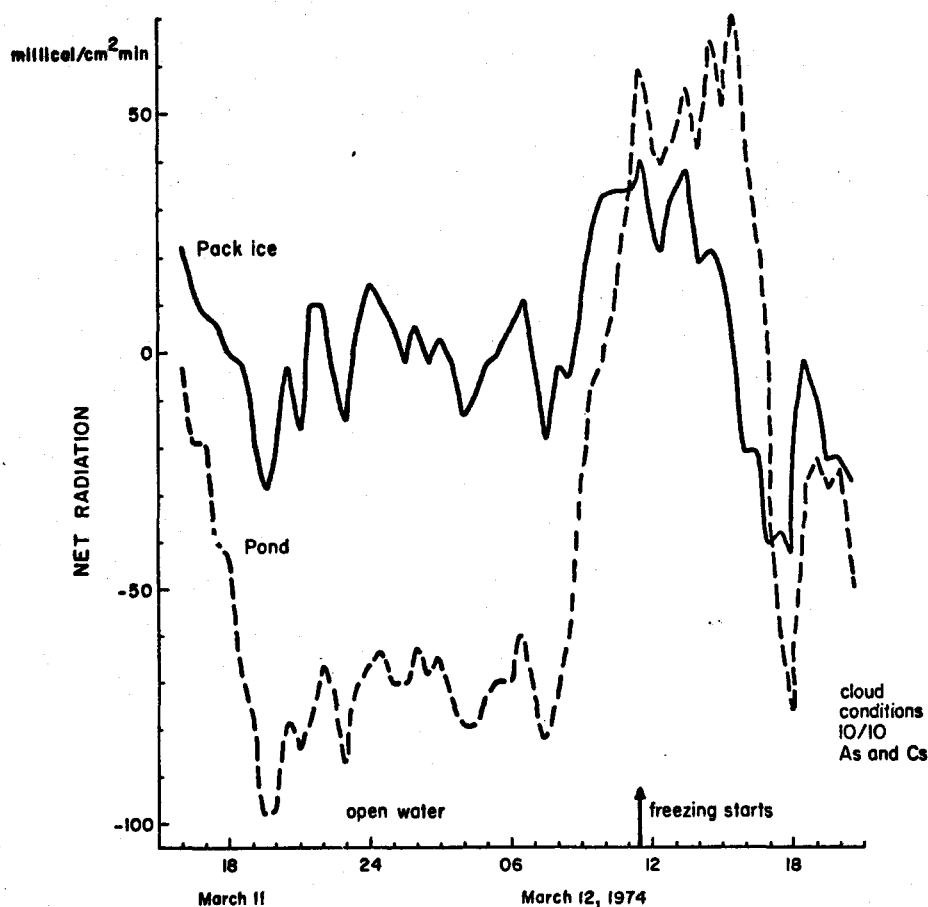


Fig. 3. Net radiation over open water and annual sea ice, under overcast conditions, March 1974, Barrow, Alaska.

low solar elevations, a detailed examination will not be made of these diurnal variations. We will instead examine the long-wave fluxes with the sun below the horizon. At night the curves of net radiation generally run parallel to each other except for minor deviations. When the cloud conditions are changing, these deviations may occasionally be due to the time difference between the recording of two channels, which amounted to about one minute. A few times, smoke from the generator might have drifted over and influenced one of the radiometers only.

When a lead freezes, the surface temperature of the new ice drops slowly (Fig. 4) and no sharp change occurs in the long-wave radiation balance. The most abrupt changes in outgoing long-wave radiation are associated with deformational changes in the lead. On 20 March the net

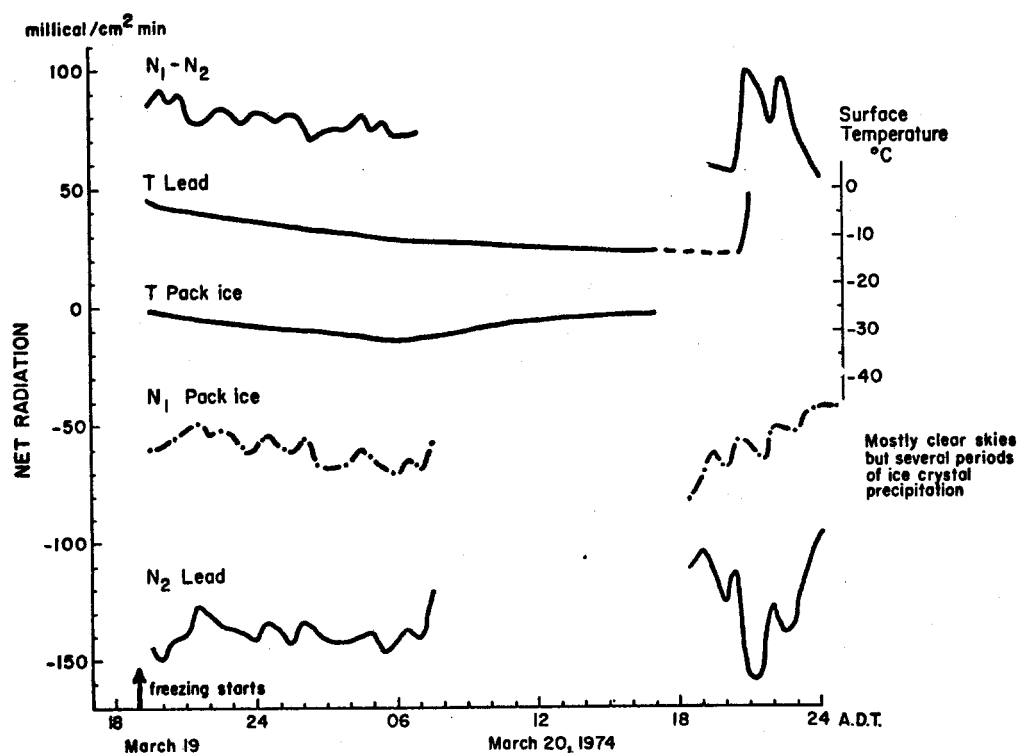


Fig. 4. Net radiation (N) and surface temperature (T) over a lead and pack ice off Barrow, Alaska.

radiation balance over the lead varied markedly because of rafting and the formation of open water stretches in the new ice. At midnight, when our record stops, the radiation equipment had to be dismantled quickly because floes had pushed over the pack ice edge close to the radiation stand.

Figures 2-4 summarize the net long-wave fluxes observed over the pack ice and over the leads or ponds. These values refer to the 1.5 m level and do not necessarily represent the surface fluxes discussed below. The values over the pack ice are in general agreement with previous measurements of long-wave fluxes during strong inversions in the polar regions. Typically, the net outgoing radiation for clear skies and moderate winds is of the order of 50 millical/cm² min. The corresponding values over the leads vary between about 100 and 150 millical/cm² min as measured at the 1.5 m level. Under cloudy conditions (Fig. 3) net losses are smaller. The effect of a thin, low cloud cover can be seen between 2100 and 2400 hours on 12 March (Fig. 3). These measurements were obtained when the wind had changed direction

and a low stratus deck had formed, probably drifting in over the lagoon from an extensive lead a few kilometers away. Most of the time the fog plumes over the small leads or ponds under investigation were of rather moderate density and vertical extent, especially when the air temperatures increased towards the end of March.

On several occasions, intensities of the surface emission were determined below both net radiometers by means of the Barnes thermal radiometer. These measurements make it possible to calculate possible divergences of the long-wave fluxes in the low layer over the leads, assuming that no flux divergence takes place over the snow-covered pack ice where the temperature gradients are relatively small.

In Table 2 the result of these comparisons is shown. Except for a few cases during daytime conditions, the calculated long-wave atmospheric radiation is higher over the leads than over the adjacent ice. The measurements of the net radiation fluxes over the leads from 9 March through 14 March represent conditions downwind of open water or freezing lead stretches of about 10-20 m. The measurements on 19 and 20 March represent conditions on the upwind side of the lead. A calculation of the possible influence of the close-by edge of the pack ice or of the snow surface next to the lead on the outgoing radiation indicates a negligible effect especially if one considers that the field of view of the lower receiving surface of the net radiometer is screened by a rim. In the experiments on 19-21 March, the positions of the net radiometers were changed from the previous experiments. Discrepancies in the instrument calibrations, therefore, probably did not cause the observed divergence.

It appears likely that the difference between the R_A values is mainly due to flux divergence below the radiometers, considering the short distance between them. A rough estimate of the divergence of the radiation fluxes due to water vapor and carbon dioxide may be made for the conditions on the upwind side of the lead, using the assumption that there is an isothermal saturated layer at air temperature under the radiometer. Using slab emissivities by Elsasser and Culbertson [1960] for various temperatures, it appears that less than 25% of the observed flux divergence may be explained by the

TABLE 2

RADIATION FLUXES OVER LEADS AND PACK ICE (millical/cm² min)

Day	Time	N_1	N_2	S_1 _{abs}	S_2 _{abs}	T_{B1} (°C)	T_{B2} (°C)	ΔT	T_B (zenith)	e_1 ^(†)	e_2 ^(†)	R_{A1}	R_{A2}	ΔR_A	Surface	Clouds
03/09	1230	-35	-27	187	48	-3.1	-30.9	27		421	281	199	206	-7	Water	Clear skies, light ice crystal precip.
	1600	-75	-26	63	37	-12.1	-29.5	17		378	287	240	224	16	Ice	Ci 10/10
03/11	2030	-79	-3	0	0	-1.6	-19.6	18	-36.2	431	336	352	333	19	Water	As 10/10
03/12	1030	14	34	84	31	-1.1	-14.6	13	-15.1	433	363	363	366	-3	Water	As 10/10
	1630	19	-21	129	37	-5.9	-15.4	10		415	359	305	301	4	Ice	light snowfall Ci 10/10
	2030	-51	-26	0	0	-7.6	-18.6	11	-22.7	40.5	342	354	316	38	Ice	St 10/10 light
03/13	1500	36	2	164	59	-2.1	-22.8	21		427	319	299	262	37	Water	St 1/10 smoke-- generator over radiometer N_2
03/14	1430	38	-8	151	65	-13.5	-20.3	7		370	333	257	260	-3	Ice	As Cs 10/10
	1930	-68	-38	0	0	-13.9	-22.6	9	-55.2	368	320	300	282	18	Ice	Cs 10/10
03/19	1940	-145	-60	0	0	-3.9	-25.9	22		427	304	282	244	38	Skim ice	Cs 5/10
03/19	2130	-126	-49	0	0	-46	-27.2	23		423	298	297	249	48	Ice	Cs 3/10 light
03/20	0030	-134	-54	0	0	-7.6	-29.5	22		405	287	271	233	38	Ice	Clear
	0630	-137	-68	0	0	-11.1	-31.5	20		384	277	247	209	38	Ice	Clear
Mean:								17						22		
Mean (night only, $S_{abs} = 0$):								18						34		

Subscript 1 = leads
Subscript 2 = pack ice

N = net all-wave flux
 S_{abs} = absorbed short-wave flux
 T_B = surface radiation temperature

e = emitted long-wave flux
 R_A = atmospheric long-wave flux

(†) $e = \delta T_B^4$ except for a water surface, when $e_1 = \frac{0.965}{0.980} \delta T_{B1}^4 \rightarrow 0.985 \delta T_{B1}^4$

absorption and emission by water vapor and carbon dioxide. It seems therefore likely that water droplets or ice crystals contribute to the main part of the observed flux divergence. It should be remarked that a haze, although mostly thin, could occasionally be observed over the leads, even after freeze-up.

We have not yet examined temperature or humidity data over the leads. We will, however, discuss other observations that have a bearing on the long-wave radiation field over a lead. Shortly after freeze-up at low air temperatures, frost flowers develop on the ice. Because of their exposure to the air, the temperature of the flowers will generally be lower than the underlying surface of new ice. For instance, on 20 March at 1650 A.D.T., measurements with the Barnes radiometer gave a radiative temperature of -12.6°C over the ice surface, -15.6°C over the frost flowers, and -26.4°C over the adjacent pack ice. On the same occasion there were also horizontal variations of the surface temperature, with a positive temperature gradient from the pack ice edge towards the middle of the lead. The temperature of the young ice 1.5 m from the lead edge was -13.3°C ; at 4 m it was -12.6°C ; and 7 m from the edge the temperature was -12.1°C . The values given in Table 2 are generally an average of several temperature readings of the surface under the radiometers. The temperature as measured by the emission normal to the ice surface thus generally increased towards the center of the lead, where the freeze-up occurred later than along the edges. However, the radiation intensity measured from a point at the side of the lead showed decreasing values as the sensor head was being pointed at increasingly oblique angles towards the ice surface. At least part of this anisotropy in the radiation field was probably due to an increase in total surface area of the frost flowers in the field of view of the sensor level as the zenith distance increased.

Measurements by the Barnes radiometer of the surface emission of open sea water varied somewhat from time to time depending on such experimental conditions as clouds. The measurements clearly showed that the emission intensity of the water surface decreased with increasing zenith distance; i.e., the water surface cannot be regarded as a perfect black body. A few times the intensity of the surface emission was measured normal to the surface

(e_0) and at a zenith distance of 45° (e_{45}) with the sensor head at a height of about 1 m above the surface. Under clear sky conditions, when the reflected sky radiation within the interval 8-14 μm can be expected to be small, the ratio e_0/e_{45} was found to be 0.985 on one occasion and 0.978 on another. Their average value of 0.982 is considerably lower than the theoretical value of 0.995 that may be calculated for water as a dielectric medium with high absorptivity by applying Kirchhoff's and Fresnel's laws and with a refractive index of 1.33 for the 8-14 μm interval [Kondratyev, 1965]. The low value of the ratio of the emissivities is again indicative of a flux divergence that might have been caused mainly by supercooled water droplets in the path between the water and the radiation sensor. Fog plumes could generally be recognized clearly over the open water surfaces (and often during the first stages of the freezing of the leads).

For a very accurate estimate of the radiation balance of water surfaces it is necessary to take into account the deviations from black body radiators. The emissivity for a plane water surface has been both theoretically and practically demonstrated to be close to 0.965 [Kondratyev, 1965]. For an open lead surface, generally with small waves and ripples, an effective emissivity of 0.97 may perhaps be an appropriate value. This value should also be representative for the effective absorptivity with a diffuse long-wave radiation field in connection with low overcast skies. For incoming long-wave radiation under clear skies, however, the effective absorptivity of the water surface should be lower, partly because the refractive index has a minimum in the atmospheric "window" region 8-14 μm , where the incoming radiation intensity is low, and partly because the intensity of the atmospheric radiation increases with increasing zenith distance at the same time as the reflectivity of the water surface increases. The total effect of these two factors may be calculated. A rough estimate indicates that the effective absorptivity of the water surface is a few percent lower than the effective emissivity under clear sky conditions. A difference of a few percent may, however, be a minor concern in calculations of the long-wave radiation energy budget of leads, considering the much larger effects of erroneous estimates of the albedo of freezing leads, the surface temperature changes, and the magnitude of the incoming long-wave fluxes.

DISCUSSION

Our observations of leads in the vicinity of Barrow indicate that, in conditions with light to moderate winds, the formation of skim ice and partial freeze-up start very soon after the open water is exposed to the cold air; the leads usually froze over within a day or less except for occasional holes kept open by seals. In winter and the early part of the light season, the long-wave losses of the leads dominate the short-wave gains. Because of the relatively high surface temperature of the young ice, the rate of long-wave heat losses is considerable in the few days after freeze-up, even if no breakup of the young ice takes place. On the other hand, because of a rapid increase in the albedo, the absorbed short-wave radiation also decreases rapidly. By March, the daily net losses of radiation may be highest following the freeze-up. For instance, if we calculate a radiation budget for the natural lead visited on 19-21 March using (a) the measured albedo values, (b) the incoming solar radiation and the surface temperatures of the undisturbed ice on the day after freeze-up, (c) an estimated albedo of the open water of 20%, (d) a sea water temperature of -1.8°C , and (3) the measured incoming long-wave radiation fluxes at night, we arrive at a net daily radiation of -146 cal/cm^2 for the open lead and -160 cal/cm^2 for the frozen lead one day later.

There are several physical parameters of the leads and their environment that must be known before reliable estimates of their radiation budget can be made. The most important seem to be:

1. The variations of the surface temperatures after freeze-up, including changes imposed by rafting and ridging of the young ice.
2. The variations of surface albedo after freeze-up, including the effect of frost flowers.
3. The formation of stratus and fog plumes over the leads.

All these characteristics may be assumed to vary in a complicated manner in relation to air temperature, wind speed, humidity, air stratification, size of the leads, etc. As regards the relatively small leads less than 100 m wide observed in the Barrow area, the fog plumes were generally quite readily visible, but only at low levels when air temperatures

were around -20°C to -30°C . The effect of these shallow plumes on the incoming short-wave and long-wave radiation was probably quite small and could not be detected within the accuracy of our instruments. On the other hand, shallow plumes or haze layers seemed to cause a noticeable divergence of the outgoing long-wave radiation above the open and freezing leads.

Over and adjacent to extensive leads, stratus layers were often observed. When these stratus layers drifted in over the measuring site, the effect on the incoming long-wave fluxes and the short-wave fluxes was more marked. Depending on the season, the net radiation of the leads may then increase or decrease. The natural seasonal variations of the physical characteristics of leads are also considerable. It is therefore suggested that systematic observations using aircraft and satellite data should be used to record typical cloud conditions over leads, and to deduce typical surface albedos and temperatures in order to provide the data needed for estimates of the total effects of leads on the Arctic radiation budget in all seasons.

ACKNOWLEDGMENTS

This study was supported by ONR Contract No. N00014-67-A-0317-0010. Logistics provided by the Naval Arctic Research Laboratory at Barrow, Alaska, are gratefully acknowledged. The project was coordinated by the AIDJEX Office, as part of the Lead Experiment.

REFERENCES

- Ambach, W. 1963. Untersuchungen zum Energieumsatz in der Ablationszone des Grönländischen Inlandeises. *Expedition Glaciologique Internationale au Groenland, 1957-60*, vol. 4, no. 4.
- Elsasser, W. M., and M. F. Culbertson. 1960. Atmospheric radiation tables. *American Meteorological Society Monograph*, vol. 4, no. 23.
- Kondratyev, K. Ya. 1965. *Radiative Heat Exchange in the Atmosphere*. New York, N.Y.: Pergamon Press.
- Lauscher, F. 1952. Sonnen- und Himmelstrahlung in Meer und Gewässern, Part I, Theorie der Strahlungsreflexion, *Arch. Meteorol. Geophys. Bioklimat.*, vol. 4, no. 2, p. 168-192.

- Liljequist, G. H. 1956. Energy exchange of an Antarctic snowfield.
Norwegian-British-Swedish Antarctic Expedition, 1949-1952, Scientific Results, vol. 2.
- Maykut, G. A., and P. E. Church. 1973. Radiation climate of Barrow, Alaska, 1962-66. *J. Appl. Meteorol.*, 12(4), 520-628.
- Ter-Markariantz, N. E. 1959. On calculation of albedo of water surfaces.
Trans. Main Geophysical Observatory, no. 80.
- Weller, G., S. A. Bowling, K. Jayaweera, T. Ohtake, S. Parker, G. Shaw, and G. Wendler. 1972. Studies of the solar and terrestrial radiation fluxes over arctic pack ice. Technical Rept. No. 2, Office of Naval Research Contract N00014-71-A-0364-0001.

SODAR INVESTIGATION OF THE EFFECT OF OPEN LEADS ON THE BOUNDARY LAYER STRUCTURE OVER THE ARCTIC BASIN

by

Bjorn Holmgren* and Linda Spears
*Geophysical Institute, University of Alaska
Fairbanks, Alaska 99701*

ABSTRACT

During the AIDJEX Lead Experiment in February-April 1974, a vertically pointing sodar (Sound Detecting and Ranging) was operated continuously at Barrow, Alaska, for one month. Stable conditions prevailed practically all the time. Two distinct flow types were recognized. One was characterized by a diffuse backscatter over a depth ranging from the lowest probing height of 25 m up to elevations of 400-500 m. This diffuse backscattering layer, which often but not always had a sharp upper boundary, apparently corresponds to the forced mixing boundary layer first investigated in detail by Sverdrup. The other turbulence regime, representing conditions of a higher overall stability, was characterized by quasi-horizontal multiple echo bands of varying thickness. The transition from a diffuse backscattering deep layer into band echoes was often gradual. A few times the acoustic record indicated transitions of the boundary structure that might have been related to open leads on the upwind side of the antenna. Two such cases are briefly discussed here.

INTRODUCTION

Open and freezing leads and polynyas within the polar pack ice release as yet unknown quantities of heat and moisture into the atmosphere in winter. Neither is it known what effect the leads have on the vertical temperature and humidity profiles in the lower troposphere away from the leads. The data from the British Trans-Arctic Expedition in 1968-1969 [Koerner, 1973] showed that 20% of the total production of new ice in the inner pack ice region is related to the freezing of leads. Much of the thin new ice is subsequently piled into ridges and hummocks.

*Now at Meteorologiska Institutionen, Observatorieparken, Uppsala, Sweden

The objective of the AIDJEX lead experiment at Barrow in February-April 1974 was to determine the effects of open and freezing leads on the atmosphere and the ocean. As an independent study, but related to this experiment, a vertically pointing sodar (acoustic radar) was operated at Barrow (Fig. 1). A continuous record was collected during the entire month of March 1974. Two cases of marked changes in the boundary layer structure are discussed briefly in relation to the possible influence of open leads. The results are somewhat ambiguous, partly because of the large distance to the leads from the observation site, but it may still be of interest to consider the acoustic soundings as a technique for observing the influence of open leads on the boundary layer structure.

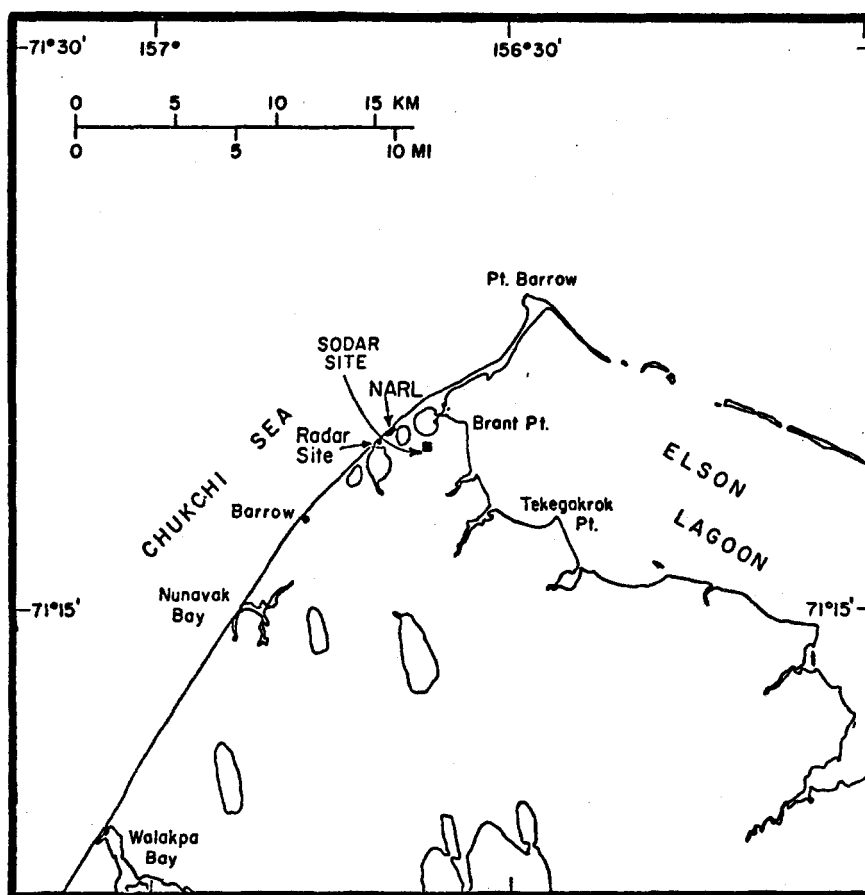


Fig. 1. Location map of the experiment sites, Pt. Barrow, Alaska.

SITE AND INSTRUMENTS

The area surrounding the sodar site is quite flat and, during the experiment, snow-covered for hundreds of kilometers in all directions. The tundra surface is generally smooth with a surface roughness parameter of about 0.03 cm [Weller and Holmgren, in press]. This value is of the same order as that found over extensive snow fields [Liljequist, 1956]. The roughness of pack ice may at times be much higher, because of the numerous pressure ridges and hummocks. During the spring of 1974, the shorefast ice along the coast west of Barrow was badly broken into densely packed ice blocks of the size of several meters. The corresponding z_0 values were probably of the order of several centimeters at least.

The sodar system (Fig. 2) was developed by the National Oceanic and Atmospheric Administration Wave Propagation Laboratory in Boulder, Colorado. A similar system has been described elsewhere [Simmons, Wescott, and Hall, 1971]. The echoes were recorded on a wet-paper facsimile machine. The vertical scanning range was about 650 m. Most of the time a 30 msec sound-pulse at a frequency of 3150 Hz was transmitted at a pulse rate of 4.16 seconds.

No special problems were encountered in regard to the cold weather or snow conditions. The antenna housing, lined by a sound-absorbing cuff to suppress the side lobes, was half buried in a snow drift. Drifting snow is common in this area, but the intensity was low for most of the experimental period. The actual snow precipitation is generally negligible during this time of the year. The small amounts of snow that did collect in the dish-shaped antenna could easily be swept out with a broom. Once or twice, in situations with heavy drifting, we put a lid on top of the antenna house and waited for better weather.

No noticeable wind noise was encountered. However, in situations with wind speeds higher than 6-7 m/sec as measured at the 3.5 m level, many echoes corresponding to the upper part of the record were probably missed because of decreasing antenna efficiency as the angle of arrival increases (see below).

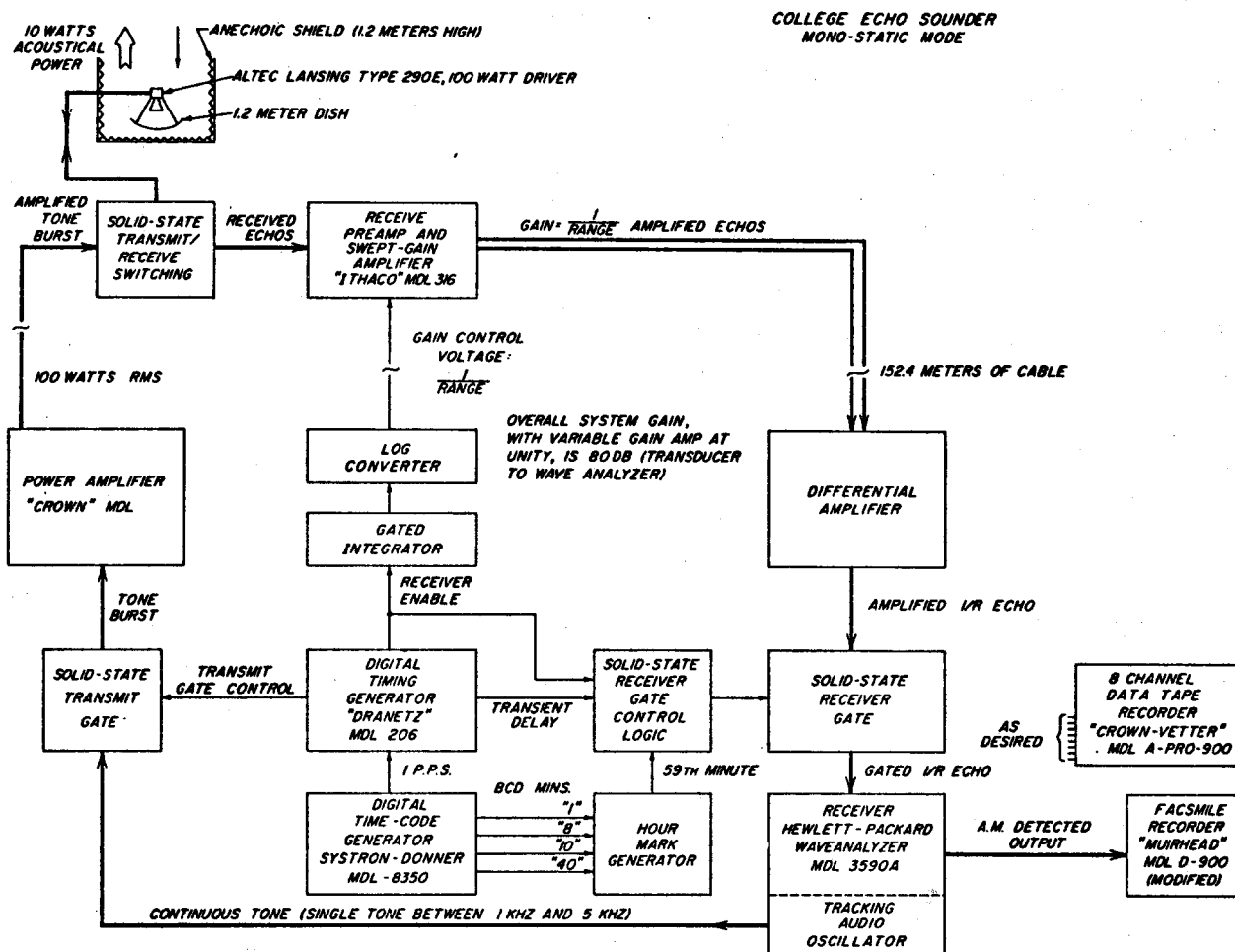


Fig. 2. Schematic diagram of acoustic sounder.

When an acoustic antenna is used both as transmitter and receiver, the backscattered acoustic power is supposedly related to the small-scale temperature fluctuations only. Assuming a Kolmogorov spectrum for the wind and temperature fluctuations, the backscattering is dominated by fluctuations on a spatial scale given by one-half the acoustic wave length. The backscatter at 180° is related only to temperature fluctuations. The atmospheric echoes in stable stratifications will generally indicate a region of enhanced turbulence. For an account of the backscattering theory, see, for example, Little [1969] and Ottersten, Hardy, and Little [1973].

GENERAL CHARACTERISTICS OF THE ACOUSTIC RECORDS

The acoustic record of Figure 3 shows diffuse backscatter from the lowest probing range of 25 m up to about 200 m with a marked upper boundary. In all likelihood this backscattering layer corresponds to the forced mixing boundary layer as first investigated in detail in the Arctic by Sverdrup [1933]. At Barrow, well-defined mixing layers appeared about 60% of the total period, mostly in situations with moderate to strong winds. There was a diurnal variation in the depth of the mixing layer and also in the strength of the backscattering echoes because of the diurnal changes of the stability. Except for a few periods associated with cold air advection or clouding over, the twice-daily routine radiosoundings at the Barrow Village as well as the acoustic records indicated a stable stratification throughout the recording period. The conditions in the lowest few meters above the surface might have been somewhat more variable.

Above the mixing layer, there were generally intermittent band echoes (Fig. 3). In conditions with light winds, the band echoes were generally stronger and more frequent than in conditions with strong winds, when the upper echoes tended to disappear in spite of the fact that strong inversions were more or less always present above the mixing layer. It is suggested that many echoes were then missed because the reception worsened as increasing winds caused the angle of arrival to widen [Mahoney, McAllister, and Pollard, 1973]. The band echoes are probably associated with windshearings in layers of high overall stability [Gossard, Jensen, and Richter, 1971; Bean, 1972; Metcalf and Atlas, 1973].

Figure 4 shows a flow regime which on the acoustic record is characterized by wavy, quasi-horizontal backscattering bands, indicating that the turbulence is mainly confined to thin sheets. The surface wind fluctuations are obviously related to the sinusoidal gravity waves propagating in the stable layers. A diffuse backscattering region in the surface layer does not appear continuously on this record, as it does on many other records in situations with light winds and a surface inversion. However, there are indications that a mixing layer may have existed most of the time, but with the upper boundary below the lower probing range of the sodar. Previous

measurements of wind and temperature profiles including temporal temperature fluctuations over a flat snow surface [Holmgren, 1971] indicated that the top of the mixing layer could descend below the 1 m level or lower when there were light winds and strong inversions.

The depth of the mixing layer, as deduced from the sodar records, generally increased with increasing winds. However, the wind speed alone was not a very good predictor of the depth of the mixing layer.

EFFECTS OF OPEN AND FREEZING LEADS

When leads open in the pack ice, the surface temperature at the lead adjusts quickly to -1.8°C . In cold weather, convection starts over the lead and the transfer of sensible heat and water vapor from the lead into the atmosphere induces changes in the boundary layer structure. West of Barrow, a lead generally opens between the shorefast ice and the moving pack ice when the winds have an offshore component. The shorefast ice extended about 1.5 km offshore in spring 1974. The ice on Elson Lagoon (Fig. 1), east of the spit, was very smooth. This ice does not open even with very strong winds; therefore, the effects of leads on the boundary layer structure can be expected to be recorded best by the sodar with onshore winds from the west or northwest.

Figures 5 and 6 are sodar records made during a change of wind direction. The 12 March data in Figure 5 were collected when the wind was changing from 270° to 320° (north = 360°). A stratus cover formed and a complete reorganization of the boundary layer took place during the observation period. Although the cloud amounts given in Figure 5 were actually measured at the village of Barrow, independent observations at a temporary location on Elson Lagoon showed similar cloud conditions there. At 2120 ADT a stratus cover was recorded, and at 2220 ADT there was a clear sky overhead at the lagoon. The lifted echo in Figure 5 is probably associated with an inversion at the top of the stratus layer. Below this lifted echo there is most likely a turbulent layer, but since only very faint echoes appear, the lapse rate is probably near-adiabatic. The depth of the mixing layer increases

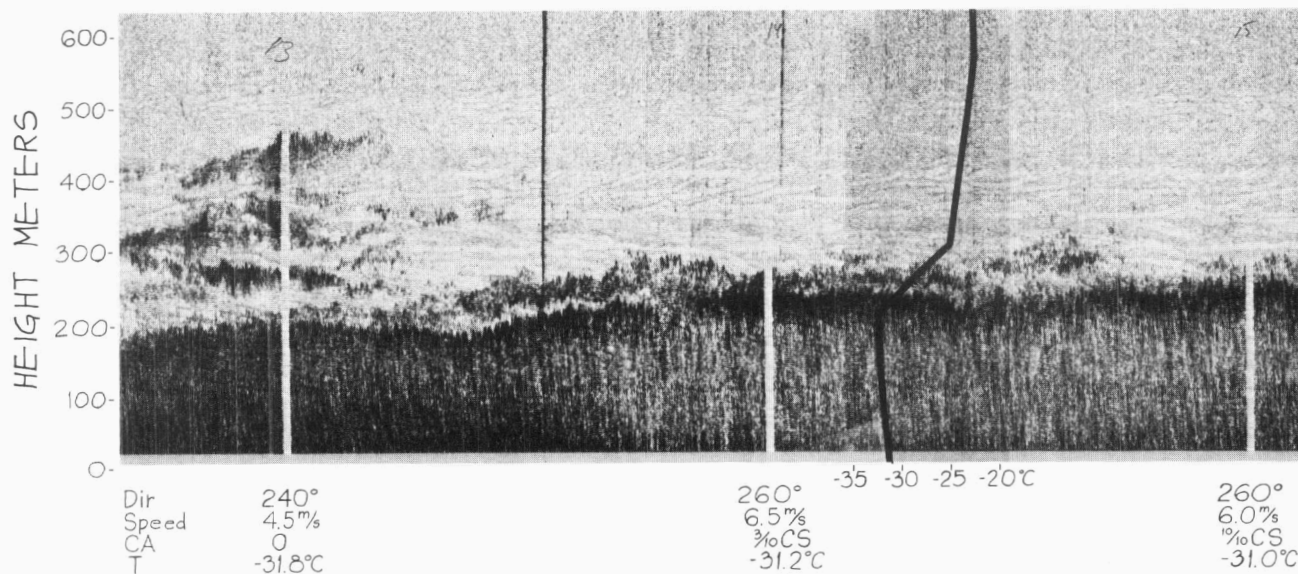


Fig. 3. Typical acoustic record, 7 March 1974, showing distinct upper boundary of mixing layer and intermittent band echoes above.

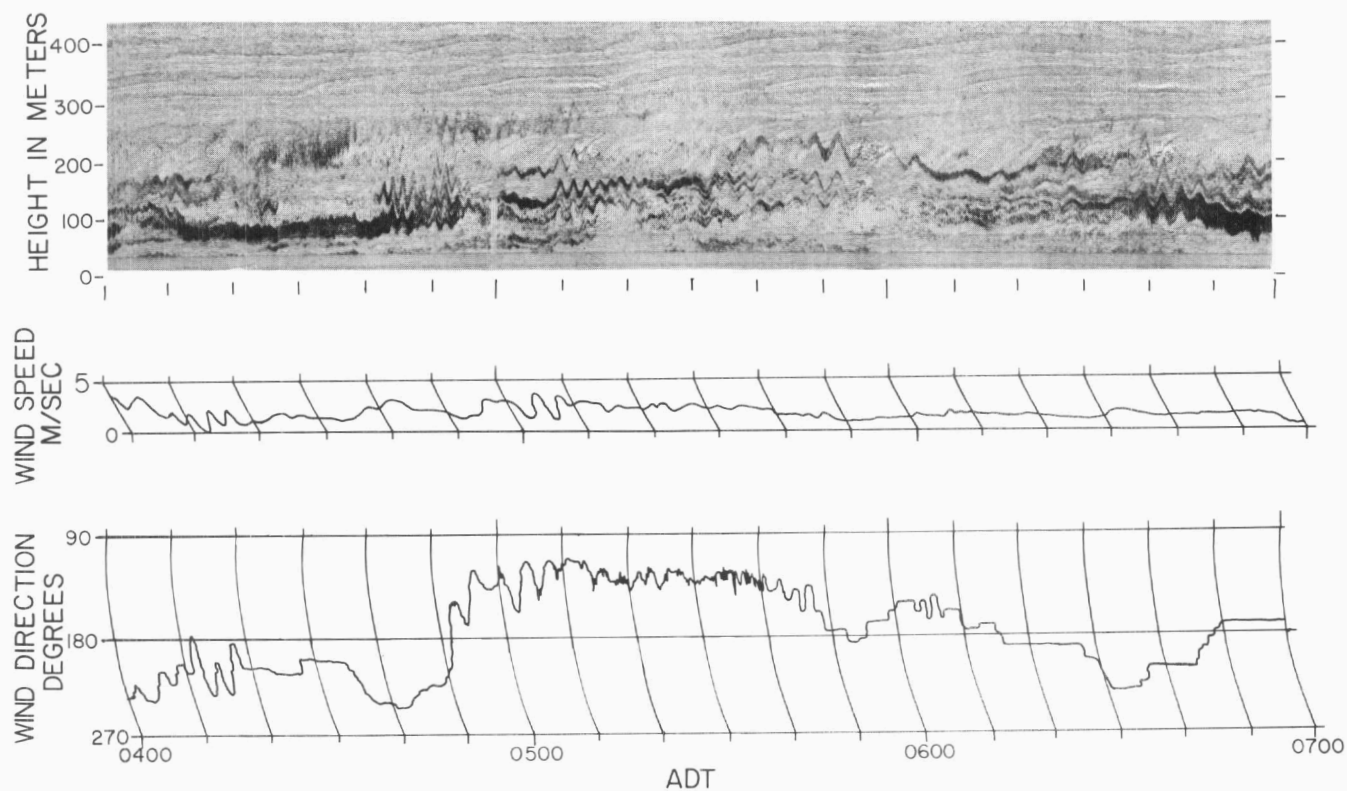


Fig. 4. Acoustic record, 12 March 1974, showing gravity waves.

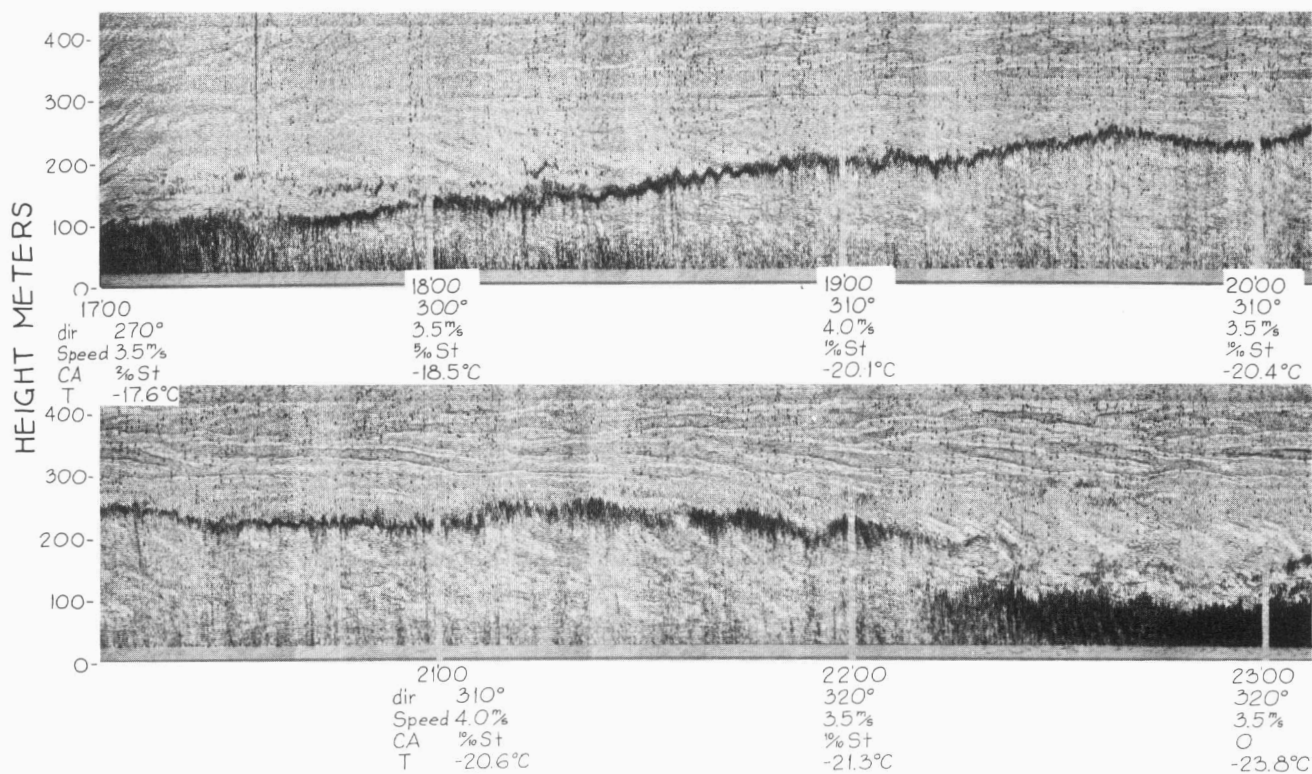


Fig. 5. Acoustic record, 12 March 1974, showing the effects of cloud formation and dissipation.

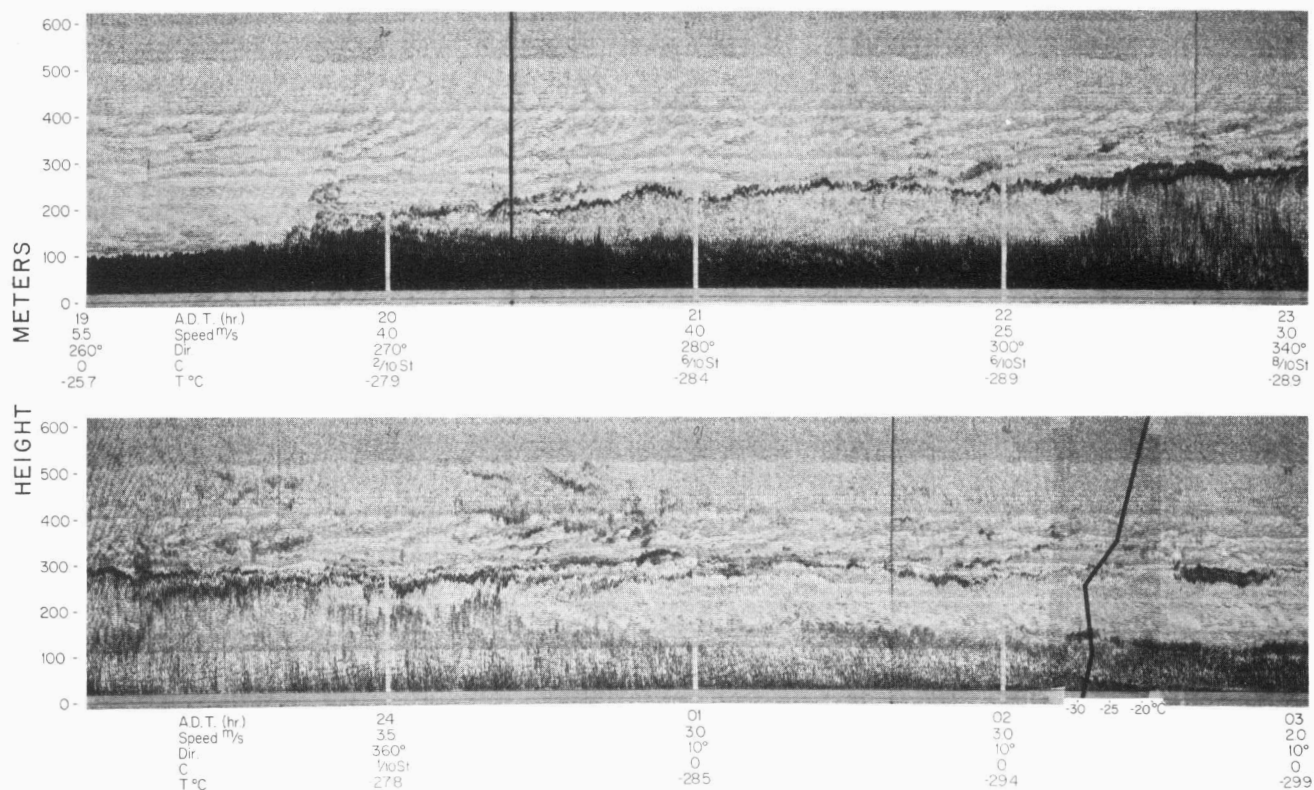


Fig. 6. Acoustic record, 19 March 1974, showing the effect of changes in wind direction.

from about 100 m at the start of the record to a maximum of 250 m and then back again to about 100 m. Both at the start and at the end of the period the mixing layers are of the forced type.

The sodar record for 19 March in Figure 6 shows first a mixing layer 100 m deep and a backscattering band that starts to rise shortly before 2000 ADT. A sudden expansion of the dark backscattering surface layer occurs after 2200 ADT to a maximum depth of about 300 m. As the upper echoes gradually weaken at the end of the record, a surface mixing layer 100 m deep again becomes the most prominent feature. During the windshift the air in the layer between 100 and 300 m becomes unstable, as found by comparing the sounding shown in Figure 6 with the Barrow radiosoundings made 12 hours before and 12 hours after that period.

Figure 7 shows a photo from a time-lapse sequence of the screen of a 3 cm radar situated on the shore close to NARL (Fig. 1). This radar is used by the Ice Research Group, University of Alaska, for detecting ice movements within a 3-mile radius. The radar data are shown here to suggest that a combination of radar and sodar might be suitable for future studies of the effect of leads. The radar echoes are caused by reflections from such projections as pressure ridges, hummocks, and ice blocks. An open water surface or new thin ice does not send back an echo. Because of the screening effect, wide areas behind high pressure ridges are free of echoes, so that one cannot generally distinguish between a lead and pack ice from a single radar frame. However, by time-lapse photography ice movements can be recognized, and sometimes the extent of leads can be inferred from the ice movements.

The lead outlined in Figure 7, which was observed by radar to open on 10 March, was surely at least partly ice covered by 12 March. The acoustic records indicate that this particular lead probably had little influence on the changes in the boundary layer at the sodar site, since the maximum elevation of the mixing layer occurred when the winds were from a section well north of the lead as seen from the sodar site. However, during the 10-12 March period, a wide continuous lead could be seen on NOAA satellite images to stretch west and north of Barrow for hundreds of kilometers along the coast, but farther out. The formation of stratus clouds and the changes in the boundary layer structure might therefore have been associated with this large lead rather than with the one noted in Figure 7.

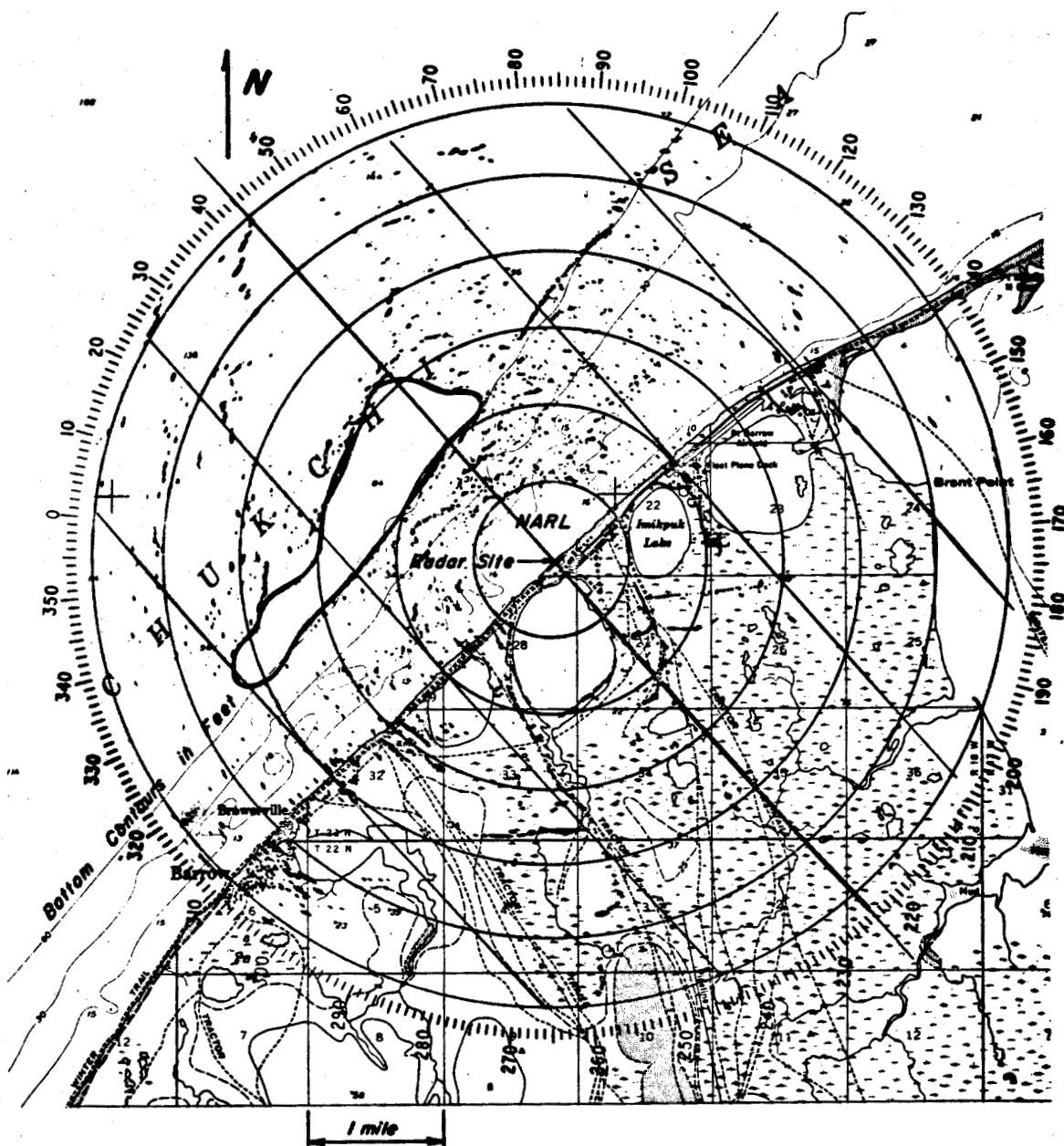


Fig. 7. Photograph from a time-lapse sequence of the 3 cm radar screen near NARL. A large lead can be seen to the west of the radar site.

An experiment involving measurements of turbulent fluxes and radiation at and over a small lead was being performed about 25 km north of Barrow on the same night that the sodar record in Figure 6 was made (19 March). Because of the distance, that particular lead would have had no noticeable effect on

the sodar record. In the pack ice north and northwest of Barrow there were several wide freezing leads and polynyas during this period; but since no open lead could be recognized within the range of the radar, we conclude that there were, at the most, only small areas of open water.

DISCUSSION

It may seem tempting, with reference to Figures 5 and 6, to interpret the deepening of the mixing layers as a result of convection over leads. This would then involve entrainment of the warm air from above the surface layer into the mixing layer. However, the weather data given in those figures show that the surface temperature is actually decreasing during the critical period. Apart from the warming to be expected by the entrainment of warm air into the mixing layer, the heat transfer from the lead should also tend to increase the temperature. The expansion of the mixing layer might therefore in this case be partly, or perhaps entirely, due to other effects, such as low-level convergence induced at the transition between the comparatively smooth, moving pack ice and the rough 1.5 km wide zone of shorefast ice. There may also have been changes of the air mass in the lowest few hundred meters involved. The weather changes on 19-20 March might have been due mainly to a low-level cold front. No such passage was seen on the surface weather maps, but they do not include enough weather data from the Arctic Ocean to be considered reliable on this point. Although our sodar data thus do not allow any safe conclusions about the effect of open and freezing leads on the boundary layer structure in these particular cases, it seems plausible that such influences can be monitored, given a suitable position of the acoustic sounder in relation to the lead.

In all seasons the heat and moisture transfers within the lower troposphere in the Arctic Basin are closely related to what happens over the leads. The leads also have an effect on the aerosols and the radiation climate. During numerous flights over the Barrow area we observed that the haziness and the horizontal visibilities in the lower troposphere could frequently be compared to conditions over big metropolitan areas in the south.

Our preliminary analysis of pyrliometric measurements indicates that the high turbidity values are critically dependent on the vertical humidity distribution. Within the mixing layer there is generally an effective transfer of moisture to the surface either by ice crystal precipitation or by condensation at the cold snow surface. In the stable layers above the mixing layer the residence time for water vapor can be expected to be many times higher if no precipitation occurs. One crucial question in this context is whether moisture from the leads can be transported up above the mixing layer. Accounts of the acoustic soundings and their relationships with the radiation measurements, humidity profiles, and temperature profiles will be given elsewhere in this Bulletin.

ACKNOWLEDGMENTS

This work was supported by ONR Contract No. N00014-67-A-0317-0010 and NSF Grant GV-27697. Logistic support was provided by the Naval Arctic Research Laboratory, Barrow, Alaska. The National Oceanic and Atmospheric Administration kindly allowed us to use their building at Barrow to house the sounder electronics. The program was coordinated by the AIDJEX Office as part of the Lead Experiment.

REFERENCES

- Bean, B. R. 1972. Application of FM-CW radar and acoustic echosounder techniques to boundary layer and CAT studies. In *Remote Sensing of the Troposphere*, ed. V. E. Derr. National Oceanic and Atmospheric Administration, Boulder, Colorado, pp. 20-1 - 20-20.
- Beran, D. W., W. H. Hocke, and S. F. Clifford. 1973. Acoustic echosounding techniques and their application to gravity-wave, turbulence and stability studies. *Boundary Layer Meteorology*, 4, 133-153.
- Gossard, E. E., P. R. Jensen, and J. H. Richter. 1971. Fine structure of thermally stable layers observed by high resolution radar. *EOS, Trans. Amer. Geophys. Union*, 51(11), 759.

- Holmgren, B. 1971. Climate and energy on a sub-polar ice cap in summer, Pt. Barrow, wind and temperature field in the low layer on the top plateau of the ice cap. Uppsala Universitet, Meteorologiska Institutionen, Meddelande, No. 108, 43 pp. (Arctic Institute of North America Devon Island Expedition, 1961-1963).
- Koerner, R. M. 1973. The mass balance of the sea ice of the Arctic Ocean. *J. Glaciology*, 12(65), 173-185.
- Liljequist, G. M. 1956. Energy exchange of an antarctic snow field: wind structure in the low layer. *Norwegian-British-Swedish Antarctic Expedition, 1949-1952, Scientific Results*, vol. 2, part 1. Oslo, Norway: Norsk Polarinstitut.
- Little, C. G. 1969. Acoustic methods for the remote probing of the lower atmosphere. *Proc. of the IEEE*, 57(4), 571-578.
- Mahoney, A. R., L. G. McAllister, and J. R. Pollard. 1973. The remote sensing of wind velocity in the lower troposphere using an acoustic sounder. *Boundary Layer Meteorology*, 4, 155-167.
- Metcalf, J. I., and D. Atlas. 1973. Microscale ordered motions and atmospheric structure associated with their echo layers in stably stratified zones. *Boundary Layer Meteorology*, 4, 7-35.
- Ottersten, H., K. R. Hardy, and C. G. Little. 1973. Radar and sodar probing of waves and turbulence in statically stable clear-air layers. *Boundary Layer Meteorology*, 4, 47-89.
- Simmons, W. R., J. W. Wescott, and F. F. Hall. 1971. Acoustic echosounding as related to air pollution in urban environments. NOAA Technical Rept. ERL 216-WPL-17, Boulder, Colorado.
- Sverdrup, H. U. 1933. Meteorology, Part 1: Discussion. *The Norwegian North Polar Expedition with the "Maud," 1918-1925, Scientific Results*, vol. 2. Bergen, Norway.
- Weller, G. E., and B. Holmgren. The microclimates of the arctic tundra. *J. of Applied Meteor.* (in press).

